

Copyright  
by  
<Ekachai Puttitwong>  
<2006>

**The Dissertation Committee for Ekachai Puttitwong Certifies that this is the approved version of the following dissertation:**

**Factors Affecting the Precision and Accuracy of Surface Temperature Measurement Using Light-pipe Radiation Thermometers (LPRTs)**

**Committee:**

---

John R. Howell, Supervisor

---

Ofodike A. Ezekoye, Co-Supervisor

---

Philip S. Schmidt

---

Matthew J. Hall

---

Kenneth S. Ball

**Factors Affecting the Precision and Accuracy of Surface Temperature  
Measurement Using Light-pipe Radiation Thermometers (LPRTs)**

**by**

**Ekachai Puttitwong, B.Eng., M.S.**

**Dissertation**

Presented to the Faculty of the Graduate School of

The University of Texas at Austin

in Partial Fulfillment

of the Requirements

for the Degree of

**Doctor of Philosophy**

**The University of Texas at Austin**

**December 2006**

## **Dedication**

To my beloved Puttitwong family:

my parents: Suthep and Pimpa;

my wife and son: Siribang-orn and Napat;

my brother and sister: Ekarat and Pattranut

## **Acknowledgements**

First of all, I would like to express my deepest gratitude and appreciation to Dr. John R. Howell and Dr. Ofodike A. Ezekoye, who are my Ph.D. advisor and co-advisor, respectively, for their invaluable guidance, support, and generosity. Without their comment and suggestion, this research study would be impossible to succeed. It was a great experience and honor for me working under their supervision. They were always available when I needed a suggestion on solving the technical problem. They provided me not only the knowledge in semiconductor and LPRT system but also a role model for being an excellent researcher. I had learnt a lot from both their class and our group meeting. Words are not enough to present how greatly appreciatory I feel to both of them.

The third person, who I wish to thank, is Dr. Kenneth S. Ball. Because of his e-mail and our first conversation, I decided to choose this research area, which is very interesting. He was not only my first supervisor and one of my dissertation committee, but also a person who introduced me to Prof. Howell and Prof. Ezekoye. I am really glad to be his advisee even though it was just my first year and a half at the University of Texas at Austin.

I also want to acknowledge my other two members of the dissertation committee, Dr. Philip S. Schmidt and Dr. Matthew J. Hall, for their careful reviews, comments, and suggestions on this dissertation.

Special thanks go to ME staffs in the machine shop: Don Artieschoufsky, Curtis Johnson, and Danny Jares, who guided me constructing the experiment; and Rosalie Foster who helped me for all purchasing process. I would also like to remember and thank all my friends and colleagues: Yan Qu whom I spent most of my time working with and talking to; Colin Beal who helped me in finding the acceptance angles of light-pipe probes; Dong Mei Zhou, Joshua D. Maxwell, Arvind Battula, Jason Lee, and Sanjiv Shah; and Wichaya Changwatchai who helped me solve the computer problem.

Finally, I wish to thank my beloved parents: Suthep and Pimpa Puttitwong. They always support me on whichever direction I choose. I cannot imagine how I could accomplish my Ph.D. without their unconditional love and greatest support. Also, my younger brother, Ekarat, and younger sister, Pattranut, are the people who do not hesitate to help me whenever I ask for. Last but not least, my deepest appreciation goes to my wonderful wife, Siribang-orn Puttitwong. She is everything in my life. I would like to say “Thank you very much” to her for staying on my side, cheering me up when I feel down, cooking my food, making me laugh, etc.

# **Factors Affecting the Precision and Accuracy of Surface Temperature Measurement Using Light-pipe Radiation Thermometers (LPRTs)**

Publication No. \_\_\_\_\_

Ekachai Puttitwong, Ph.D.

The University of Texas at Austin, 2006

Supervisor: John R. Howell

Co-supervisor: Ofodike A. Ezekoye

The accurate measurement of temperature in Rapid Thermal Processing (RTP), a key technique that processes single silicon wafers at a lower cost and in a shorter period of time, is of vital importance for improving the productivity of high quality devices. In order to meet the requirement of the International Technology Roadmap for Semiconductor 2004 (ITRS-2004), which is an uncertainty of  $\pm 1.5$  °C at 1,000 °C, light-pipe radiation thermometers (LPRTs) are the sensor of choice to monitor the wafer temperature during the processing.

To achieve this goal of uncertainty, a unique test bed, which is an axisymmetric design chamber with a three-zone ceramic heater, was developed by the University of Texas and used to calibrate the LPRT system by comparing its reading with the temperature reading obtained from an instrumented wafer. However, a difference of 10 °C to 30 °C between these two readings was found. This dissertation focuses on finding

the error sources with three different types of light-pipes: fused silica, fused quartz, and sapphire.

The thermal environment effect is the first factor to be determined. The diffuse reflectivity caused by the surface imperfections of the LPRT is determined in this research. Three different surface roughness values of fused silica light-pipe created by different type of sandpapers were performed, and their results were compared with previous Monte Carlo simulation results. Furthermore, different types of light-pipe can be affected differently. To explain which light-pipe material can be most influenced by the thermal environment effect based on its spectral properties, the sensitive wavelength range of our photo-detector was measured.

Another study is the effect of the separation distance between the light-pipe tip and the measured object on the object surface made by the light-pipe probe. To determine which type of object and light-pipe materials are causing the separation distance effect, ceramic and molybdenum, which were painted with flat black ultra-high-temperature paint, were used as the measured targets. Moreover, the experimental results were compared to a computer model using the finite-difference method in order to predict the temperature depression as the space between the tip of the light-pipe and the target increases. To obtain higher accuracy in the computer simulation, the spectral properties of each material were measured by using an infrared spectroradiometer. To understand the directional range over which the LPRT can detect the radiation signal, the acceptance angles of each light-pipe materials were also measured.

## Table of Contents

List of Tables .....	xi
List of Figures .....	xii
List of Figures .....	xii
Chapter 1: <i>Introduction</i> .....	1
1.1 Rapid thermal processing .....	1
1.2 Temperature measurement in rapid thermal processing .....	5
1.2.1 Thermocouple .....	6
1.2.2 Radiation thermometer .....	9
1.3 Scope of research .....	13
Chapter 2: <i>Uncertainty Analysis</i> .....	17
2.1 Background .....	17
2.2 Sources of uncertainty .....	18
2.3 Uncertainty characterisation .....	21
2.3.1 Type A component .....	22
2.3.2 Type B component .....	24
2.3.3 Combining uncertainty component .....	26
2.3.4 Expanded uncertainty component .....	28
Chapter 3: <i>Discussion on Thermal Environment Effect</i> .....	30
3.1 Introduction .....	30
3.2 Determination of effective wavelength of LPRT sensor .....	31
3.3 Experimental set-up and results .....	38
3.4 Comparison between measured and computer-model results .....	54
Chapter 4: <i>Discussion on Separation Distance Effect</i> .....	62
4.1 Introduction .....	62
4.2 Experimental set-up and results .....	64
4.3 Computer simulation results .....	75
4.4 Determination of acceptance angle of LPRT sensor .....	86

Chapter 5: Conclusions and Recommendations .....	96
5.1. Conclusions.....	96
5.1.1 Effective wavelength .....	96
5.1.2 Thermal environment effect .....	97
5.1.3 Separation distance effect.....	98
5.1.4 Effect of acceptance angle .....	100
5.2 Recommendations.....	102
References.....	104
Vita .....	109

## List of Tables

Table 1.1:	Compositions and upper temperature limits for various TCs. ....	6
Table 2.1:	Temperature fixed points defined by ITS-90 at 1 atm [Figliola and Beasley, 2006]. ....	19
Table 2.2:	Student t-distribution [Taylor and Kuyatt, 1994]. ....	29
Table 3.1:	Overview of wavelength range for each component. ....	33
Table 3.2:	The values of m and b for linear correction factor equation. ....	40
Table 3.3:	Example of uncertainty budget of fused silica light-pipe. A, B, and C are divisor, uncertainty value, and standard uncertainty, respectively. .	42
Table 3.4:	Surface roughness measurements in microinches for cylindrical surfaces at each end of LPRTs. ....	52
Table 3.5:	Surface roughness measurements in micron and diffuse reflectance gained from matching Yan Qu’s computer code with experimental results. ....	57
Table 4.1:	Overview of thermal conductivity for each material. ....	66
Table 4.2:	Example of uncertainty budget of sapphire light-pipe with ceramic plate at 475 °C and 2-mm spacing. A, B, and C are divisor, uncertainty value, and standard uncertainty. ....	67
Table 4.3:	Temperatures of surrounding and cold radiation shield at different chamber temperatures. ....	81
Table 4.4:	Summary of shield temperature (°C) in UT-Austin RTP chamber. ....	95

## List of Figures

Figure 1.1: Relationship between wafer thickness and diameter [ <a href="http://www.itrs.net">http://www.itrs.net</a> ].	2
Figure 1.2: Schematic diagram of typical RTP test bed wafer chamber [Ranish, 2003].	4
Figure 1.3: Basic thermocouple circuit.	9
Figure 1.4: Infrared transmission spectrum of atmosphere [Maxwell, 2005].	11
Figure 1.5: NTM 500-R LPRT system.	12
Figure 2.1: Example of PRT hysteresis error evaluation [Nicholas and White, 1994].	20
Figure 2.2: The approached geometry of regression uncertainty.	23
Figure 2.3: Normal or Gaussian probability distribution [Figliola and Beasley, 2006].	25
Figure 3.1: Illustration of a beam reaching the smooth sidewall of the light-pipe probe [Puttitwong, Qu, Howell, and Ezekoye, 2006].	31
Figure 3.2: Schematic of the top view of optical layout for the spectroradiometric measurement system.	32
Figure 3.3: Comparison of response curves at the current of 5.5 A and at different wavelength for the detector with and without light-pipes attached.	34
Figure 3.4: Comparison of response curves at different wavelength and different applied current for the detector with fused silica light-pipe.	35
Figure 3.5: Temperature readings versus wavelength for the detector with fused silica light-pipe.	36

Figure 3.6: Illustration of effective wavelength range of detector with fused silica light-pipe.....	37
Figure 3.7: Schematic of experimental set-up.....	39
Figure 3.8: Comparison of measured temperature of three light-pipes before and after applying linear correction factors at the blackbody temperature of 500 °C.....	41
Figure 3.9: Actual temperature results displayed by fused silica light-pipe at four different blackbody temperature settings.....	44
Figure 3.10: Actual temperature results displayed by fused quartz light-pipe at four different blackbody temperature settings.....	44
Figure 3.11: Actual temperature results displayed by sapphire light-pipe at four different blackbody temperature settings.....	45
Figure 3.12: Spectral transmittances of three different LPRT materials at the normal incident angle $\theta = 0^\circ$ .....	46
Figure 3.13: Reflectances of three different LPRT materials at the $\lambda = 1,013.98$ nm.....	47
Figure 3.14: Spectral reflectances of three different LPRT materials at the normal incident angle $\theta = 0^\circ$ .....	48
Figure 3.15: Comparison of temperature readings between different end and different furnace location of fused silica light-pipe at $T_{BB} = 500$ °C. ....	49
Figure 3.16: Comparison of temperature readings between different end and different furnace location of fused quartz light-pipe at $T_{BB} = 500$ °C.....	50
Figure 3.17: Comparison of temperature readings between different end and different furnace location of sapphire light-pipe at $T_{BB} = 500$ °C.....	50

Figure 3.18: a) Magnified images at 500X of fused silica light-pipe with different surface roughness and b) Comparison of measured temperature readings among three different surface roughness values. ....	53
Figure 3.19: Flow chart diagram of Yan Qu’s Monte Carlo model for determining the thermal environment effect [Qu, 2006]. ....	56
Figure 3.20: Comparison of experiment and computer simulation light-pipe temperature results. ....	57
Figure 3.21: a) Reflectivity and transmittivity for radiation incident on a thick semitransparent material [Modest, 2003], and b) Experimental set-up for determining the actual reflectivity. ....	59
Figure 3.22: Spectral directional-hemispherical reflectivity (%) of fused silica light-pipe at different surface roughness. ....	60
Figure 3.23: Spectral transmittivity (%) of fused silica light-pipe at different surface roughness. ....	60
Figure 4.1: Illustration of NIST RTP test bed [Kreider, Chen, Dewitt, Kimes, and Tsai, 2003]. ....	63
Figure 4.2: Schematic of UT-Austin RTP test bed [Qu, Puttitwong, Howell, Ezekoye, and Ball, 2005]. ....	64
Figure 4.3: Schematic of chamber and several internal components. ....	65
Figure 4.4: The changes in temperature of TCs embedded on molybdenum sheet due to the different positions of the fused silica light-pipe for the chamber temperature of 400 °C. The uncertainty of TC#1 is + 5.3 °C. ....	69
Figure 4.5: The changes in temperature of TCs embedded on molybdenum sheet due to the different positions of the fused silica light-pipe for the chamber temperature of 475 °C. The uncertainty of TC#1 is + 5.7 °C. ....	69

- Figure 4.6: The changes in temperature of TCs embedded on molybdenum sheet due to the different positions of the fused silica light-pipe for the chamber temperature of 550 °C. The uncertainty of TC#1 is + 6.2 °C. .... 70
- Figure 4.7: The changes in temperature of TCs embedded on molybdenum sheet due to the different positions of the fused quartz light-pipe for the chamber temperature of 400 °C. The uncertainty of TC#1 is + 5.3 °C. .... 70
- Figure 4.8: The changes in temperature of TCs embedded on molybdenum sheet due to the different positions of the fused quartz light-pipe for the chamber temperature of 475 °C. The uncertainty of TC#1 is + 5.7 °C. .... 71
- Figure 4.9: The changes in temperature of TCs embedded on molybdenum sheet due to the different positions of the fused quartz light-pipe for the chamber temperature of 550 °C. The uncertainty of TC#1 is + 6.2 °C. .... 71
- Figure 4.10: The changes in temperature of TCs embedded on molybdenum sheet due to the different positions of the sapphire light-pipe for the chamber temperature of 400 °C. The uncertainty of TC#1 is + 5.3 °C. .... 72
- Figure 4.11: The changes in temperature of TCs embedded on molybdenum sheet due to the different positions of the sapphire light-pipe for the chamber temperature of 475 °C. The uncertainty of TC#1 is + 5.7 °C. .... 72
- Figure 4.12: The changes in temperature of TCs embedded on molybdenum sheet due to the different positions of the sapphire light-pipe for the chamber temperature of 550 °C. The uncertainty of TC#1 is + 6.2 °C. .... 73
- Figure 4.13: The changes in temperature of TCs embedded on ceramic plate due to the different positions of the fused silica light-pipe for the chamber temperature of 475 °C. The uncertainty of TC#1 is + 5.7 °C. .... 74

Figure 4.14: The changes in temperature of TCs embedded on ceramic plate due to the different positions of the fused quartz light-pipe for the chamber temperature of 475 °C. The uncertainty of TC#1 is + 5.7 °C. ....	74
Figure 4.15: The changes in temperature of TCs embedded on ceramic plate due to the different positions of the sapphire light-pipe for the chamber temperature of 475 °C. The uncertainty of TC#1 is + 5.7 °C. ....	75
Figure 4.16: Schematic details of computer model. ....	77
Figure 4.17: Spectral directional-hemispherical reflectivity (%) of fused silica, fused quartz, and sapphire light-pipes. ....	78
Figure 4.18: Spectral directional-hemispherical reflectivity (%) of materials with and without coatings. ....	78
Figure 4.19: Fractional blackbody emissive power in the range 0 to $\lambda T$ [Siegel and Howell, 2002]. ....	79
Figure 4.20: Illustration of disk to parallel coaxial disk of unequal radius [Siegel and Howell, 2002]. ....	80
Figure 4.21: Illustration of outer surface of cylinder to annular disk at end of cylinder [Siegel and Howell, 2002]. ....	80
Figure 4.22: Grid study for object temperature. ....	84
Figure 4.23: Temperature profile across the ceramic plate for different tip-to-target spacing of sapphire light-pipe. ....	84
Figure 4.24: Comparison of the magnitude of the separation distance effect among different combination of object and light-pipe's materials. ....	85
Figure 4.25: Tip temperature at each separation distance when using different kinds of objects and light-pipes. ....	86

Figure 4.26: Schematic of light beam traveling inside the light-pipe probe relative to the incident angle [Qu, 2006].....	88
Figure 4.27: Schematic of experimental set-up for determining the acceptance angle. ....	89
Figure 4.28: Illustration of averaged temperature readings obtained from different kinds of light-pipe versus the incident angle. ....	90
Figure 4.29: Comparison of the results obtained from the experiment and the MCM simulation for each incident angle. ....	91
Figure 4.30: Illustration of the shape of light beam coming out from fused silica light-pipe when the distance between light-pipe tip and white paper is 168.3 mm and the incident angle is 10 degrees. ....	92
Figure 4.31: Exit angle versus incident angle (degrees) for fused silica and fused quartz light-pipes. ....	93
Figure 4.32: a) Light-pipe temperature readings at different LPRT's tip locations, and b) Light-pipe temperature differences at different separation distances and at 0.5 mm away from the surface of silicon wafer (in UT-Austin RTP test bed).....	94

## **Chapter 1: *Introduction***

### **1.1 RAPID THERMAL PROCESSING**

In the world of high technology, semiconductor device manufacturing plays an important role for almost every human being. The overall market of this industry consists of silicon integrated circuits (IC), micro-electro-mechanical systems (MEMS), automation, solar cell, communication, etc. Its progress and success has been achieved through lowering production costs, reducing the device dimensions, increasing the doping density, and decreasing the defect density.

As mentioned by Gordon Moore, the demand for semiconductor chips is growing rapidly. Therefore, the most efficiently economical way for chip manufacturers to meet this demand is to increase the silicon wafer diameter. Over a decade, the wafer dimension has been changed many times. It was initially 200 mm in 1995, and then moved to 300 mm in the year of 2001. The wafer sizes are expected to be 450 mm and 675 mm in the years 2010 and 2020, respectively. The wafer thickness also depends on the wafer diameter because of possible damage during handling and the sagging issue during processing. For example, 825  $\mu\text{m}$  is the recommended thickness for a 450 mm diameter wafer. Figure 1.1 shows the relationship between the wafer diameter in millimeters and the wafer thickness in micron.

At present, many of the thermal processes involved in semiconductor manufacturing are performed in conventional batch furnaces. This type of furnace operates at atmospheric condition and uses convective heating tubes in order to obtain the target temperature profile over a large batch of wafers, which usually contain 150-200 wafers per batch. The typical ramp-up rate of 10 °C/min and ramp-down rate of 3 °C/min

are required for this operation which leads to the total cycle time of 4-10 hours per batch [Yoo, Yamazaki, and Enjoji, 2000].

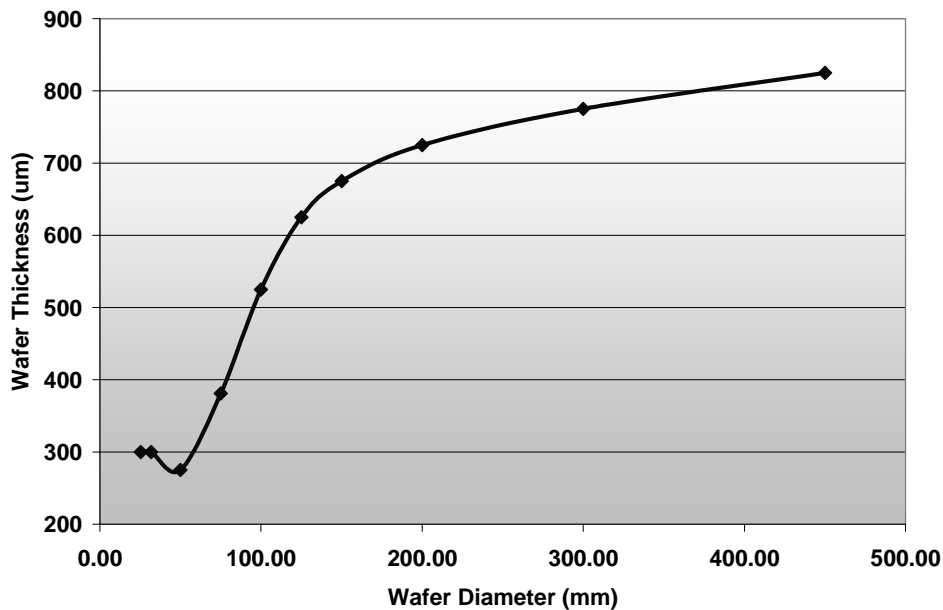


Figure 1.1: Relationship between wafer thickness and diameter [<http://www.itrs.net>].

Because of the conventional furnace geometry, it is impossible to uniformly heat the wafers. The temperature at their edges will always be higher than at their center since they are exposed to the high temperature of the furnace wall. On the other hand, the edges will lose heat faster than the center during the cooling process. The temperature gradients across the silicon wafer surface have to be limited to eliminate the cause of film thickness non-uniformity occurring during the chemical vapor decomposition process, and stress accumulations. Studies have demonstrated that gradients in excess of 10 °C/cm can introduce plastic deformation or crystalline lattice slip within the wafer resulting in dangling bonds, altered solid solubility, shorter recombination times, and trapped charges [Perkins, Riley, and Gyurcsik, 1995]. To achieve more uniformity, the space between

each wafer has to be increased, causing larger batch furnace size. Furthermore, the temperature inside a batch furnace is controlled by using several thermocouples placed at various positions in the furnace, which do not reflect the real wafer temperature.

To reduce the production cost due to the long process cycle time of conventional batch processing and to improve the product quality and reliability due to the poor across-wafer temperature uniformity of batch furnaces, rapid thermal processing (RTP), a key technique that processes single silicon wafer at high temperature (1000 °C to 1,200 °C), has been introduced into the semiconductor business. Treating individual wafers can reduce the loss risk of system failure per run. As implied by the word “rapid” in RTP, the total cycle time for RTP method is short (1-5 min/wafer) since the ramp-up (20-250 °C/sec) and ramp-down (up to 90 °C/sec) rate are high [Yoo, Yamazaki, and Emjoji, 2000]. This faster processing time can help to reduce the energy consumption, resulting in lower thermal costs. Popular uses of rapid thermal processing are rapid thermal annealing (RTA), rapid thermal oxidation (RTO), and rapid thermal chemical vapor deposition (RTCVD).

The essential components of an RTP system mainly consist of a process chamber, heat source, process gas delivery system, temperature measuring device, and temperature controller. A typical RTP chamber is illustrated in Figure 1.2. The types of the process chambers can be either hot wall with resistively heated silicon carbide, warm wall with air-cooled quartz, or cold wall with water-cooled stainless steel. Generally, a wafer in an RTP system is heated by using a bank of tungsten-halogen lamps, which range from 25 to over 150 lamps configured from 4 to 14 zones [Reid and Sitaram, 1996], and can be as high temperature as  $\approx 2,700$  °C. This heat source is defined by the term “lamp annealing” [Hart and Evans, 1988]. Unlike the convective-based heating system of the conventional furnace, this radiant heating mechanism, which directly heats the silicon

wafer to high temperature without sacrificing deposition quality [Perkins, Riley, and Gyurcsik, 1995], allows more flexibility in rapid heating and cooling. So, the chamber wall temperature is much lower than the wafer temperature. The temperature control in RTP technology is based on a real-time wafer temperature measurement. This in-situ measurement and control can help the system produce more uniform temperature across the wafer. Another advantage of RTP relative to batch processing is the ability to minimize the particle contamination because of the high purity of the ambient gas surrounding each wafer.

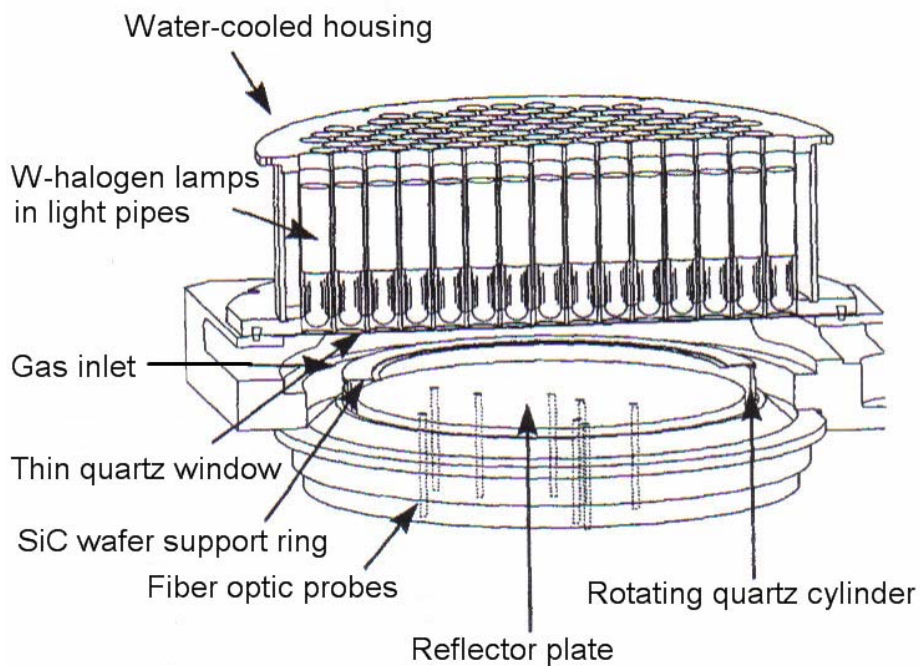


Figure 1.2: Schematic diagram of typical RTP test bed wafer chamber [Ranish, 2003].

In spite of all these advantages of the RTP furnace which seems attractive to semiconductor industry, wafer temperature control is the major drawback that arises with the use of this new technology. This hurdle can be split into two main separate

components. The difficulty in reproducing the identical RTP chamber conditions (time-temperature cycle) on different wafers is the first disadvantage. As mentioned, the heating mechanism in RTP system is largely radiative, so it is hard to make every point on the wafer surface experience the same temperature. The main factors are that the thermal energy radiated by the heated wafer is non-uniform and the total emissive flux that is emitted from the wafer is not a linear function of its surface temperature [Perkins, Riley, and Gyurcsik, 1995]. The last hurdle is the inability to achieve consistent across-wafer temperature. As opposed to batch processing, the wafer edges in an RTP chamber tend to lose more heat than the rest of the wafer surface because of the non-reflective features on the chamber wall and the convective heat loss caused by the process gas flowing over the wafer. Even though silicon is a good thermal conductor, it is difficult to smooth out the temperature profile over a 10 cm length scale [Timans, 1998]. Furthermore, this temperature uniformity is critical for improving RTP technology since smaller electronic devices require tighter temperature uniformity. The solution to these hindrances is to measure and to control the temperature in-situ by using both accurate and fast temperature sensors.

## **1.2 TEMPERATURE MEASUREMENT IN RAPID THERMAL PROCESSING**

Because of the temperature measurement issues including accuracy, repeatability, and compatibility with the RTP process, rapid thermal processing has not been widely used in the semiconductor industry. There are many measuring methods that can be applied in this manufacturing technology and are traceable to the international temperature standard (ITS) such as thermocouples, radiation thermometers or pyrometers, power control, in-situ ellipsometry, speckle interferometry, ripple technique pyrometry, slip rings, radial lamp housings, and acoustic waves [Yan, 1999]. However, only thermocouples and pyrometers are currently used by most of the RTP

manufacturers, and these can also do in-situ measurements. These two measuring instruments will be discussed in the following two sections.

### 1.2.1 THERMOCOUPLE

Thermocouples are one of the most widely used of all temperature measurement sensors today. They have the advantages of being inexpensive, simple to use, reliable, available in various sizes, and able to withstand harsh environments. There are 25 different types of thermocouples in service over a wide range of temperatures, and they are classified by the material compositions at the bead, between two wires joined together. However, only seven of them are commonly used in RTP which are types E, J, K, N, B, S, and R. They are summarized in Table 1.1.

Types	Materials	Max. Temp (°C)	Best Accuracy
E	nickel-chromium alloy/copper-nickel alloy	870	1.5 °C or 0.4% of readings
J	iron/another slightly different copper-nickel alloy	760	
K	nickel-chromium alloy/nickel-aluminium alloy	1,260	
N	nickel-chromium alloy/nickel-silicon alloy	1,300	
B	platinum-30% rhodium/platinum-6% rhodium	1,700	1 °C plus
S	platinum-10% rhodium/platinum	1,400	0.3% of
R	platinum-13% rhodium/platinum	1,400	(t-1100)°C

Table 1.1: Compositions and upper temperature limits for various TCs.

The basic theory of thermocouple thermometers is based on the thermoelectric effects consisting of the Seebeck effect, the Peltier effect, and the Thomson effect. The

Seebeck effect is the voltage difference caused by a temperature gradient between the junction of two dissimilar metals, A and B. The magnitude of this potential,  $E_S$ , which is on the order of several microvolts per unit temperature change is related to the Seebeck coefficients,  $S_{A,B}$ , also called the thermoelectric power or the thermopower, and is expressed as  $dE_S = S_{A,B}dT$ . The non-linear Seebeck coefficients depend on material, molecular structure, and temperature. Unlike Peltier and Thomson effects, the Seebeck effect is the heat-to-electricity effect that is relevant for thermocouple thermometers and the only effect occurring without any electric current.

The Peltier effect represents the reversible heat absorption or evolution when an electric current created by an external source or by the thermocouple itself is passed through an abrupt interface between two metals. The amount of heat per unit time is equal to  $Q = \pi_{A,B}I$  where  $\pi_{A,B}$  is the Peltier coefficient. This coefficient shows the amount of heat that has been accumulated or depleted per unit charge current. The direction of this heat transfer is related to the current polarity causing the sign of the heat absorbed/evolved. The Peltier heating or cooling can perturb the measured temperature readings. In order to eliminate the flowing current in the thermocouple circuit, high-impedance voltage-measurement devices are used [Schooley, 1986].

The Thomson effect deals with the reversible evolution or absorption of heat when a current traverses a single homogeneous conductor with a temperature gradient. This is almost similar to the Peltier effect considering the number difference of free electrons on both sides of the junction except that the Thomson effect accounts for the difference of free electron density existing along the conductor [Michalski, Eckersdorf, and McGhee, 1991]. So, not only the Peltier voltage but also the single conductor itself can be carriers of emf. The heat production per unit volume can be calculated by the difference between the Joule heating,  $\rho J^2$ , and the Thomson heat,  $\mu JdT/dx$ . The  $\rho$  is

the material resistivity, the  $J$  is the current density, the  $dT/dx$  is the temperature gradient along the distance, and the  $\mu$  is the Thomson coefficient. Essentially, the Seebeck effect is the summation of the Peltier and Thomson effects.

Beside the above basic theory, thermocouples are also governed by three other fundamental laws which are the law of homogeneous circuits states, the law of intermediate metals states, and the law of successive temperatures states. With these three laws, extension metal wire can be added to a circuit with no effect to the temperature measurement as long as its junctions are at the same temperature. Figure 1.3a shows the principal law of emf. If the ends of metal A are at the temperatures of  $T_1$  and  $T_2$  which generates an emf of  $E_1$  and the other two junctions of metal B are at  $T_2$  and  $T_3$  which produce an emf of  $E_2$ , then the net potential generated by these two metals is the combination of  $E_1$  and  $E_2$ . Therefore, the target temperature measurement can be obtained by thermocouples if one junction is maintained at a known temperature called the reference junction or the cold junction, as illustrated in Figure 1.3b. This reference temperature is usually kept at  $0^\circ\text{C}$ . The voltage-temperature relationship of a thermocouple is a polynomial function given as  $T = \sum_{n=0}^N a_n E^n$  where  $a_n$  is a coefficient and  $N$  is between 5 and 9. Both values depend on the thermocouple types.

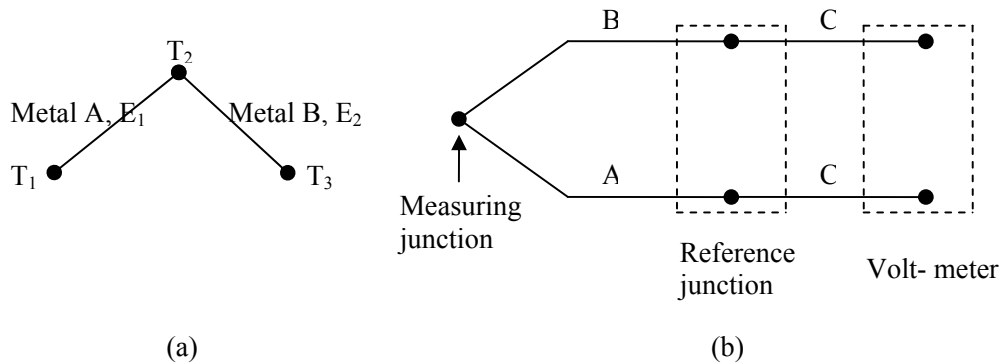


Figure 1.3: Basic thermocouple circuit.

Although thermocouples provide reasonable accuracy in RTP, there are several disadvantages associated with the measurement such as slow response time, low resolution, metal contamination, and limited lifetime. In addition, thermocouples are intrusive temperature measuring devices which can cause thermal perturbations on the wafer surface affecting the temperature readings, and can damage the surface of the wafer. Optical pyrometers, considered to be nonintrusive instruments, have been the sensor of choice for monitoring production wafers and controlling process temperature.

### 1.2.2 RADIATION THERMOMETER

The optical pyrometer has been used in many high temperature industries because of its high resolution and fast response time, as short as 1-10 ms. [Yan, 1999]. It is also a class of non-contact thermometer that is fundamentally based on the thermal radiation theories created by Max Karl Ernst Ludwig Planck, Joseph Stefan, Ludwig Eduard Boltzmann, and Wilhelm Wien. It measures the temperature by collecting the radiation from a hot object surface and relating that energy to the object's temperature. The spectral emitted energy,  $E$ , is described by the Planck equation:

$$E(\lambda, T) = \frac{\varepsilon_{\lambda} C_1}{\lambda^5 \left( e^{C_2/\lambda T} - 1 \right)} \quad , W / m^3 \quad (1.1)$$

where  $\varepsilon_{\lambda}$  is the spectral emissivity, and  $C_1$  and  $C_2$ , which are first and second radiation constants, are equal to  $3.742 \times 10^{-16} W \cdot m^2$  and  $1.4388 \times 10^{-2} m \cdot K$ , respectively. The emissivity is defined by the ratio of energy radiated by a real body and by a blackbody. An emissivity of 1 is for a true blackbody surface. Any real object would have an emissivity less than 1. The total radiant energy of this real object can be calculated by using the Stefan-Boltzmann equation:

$$E(T) = \varepsilon \sigma T^4 \quad , W / m^2 \quad (1.2)$$

where  $\sigma$  known as the Stefan-Boltzmann constant is equal to  $5.6704 W \cdot m^2 K$ . An inverse relationship between the wavelength of the peak intensity of a blackbody and the temperature is stated by Wien's displacement equation:

$$\lambda_{\max} T = 2.8977685 \times 10^{-3} \quad , m \cdot K \quad (1.3)$$

Considering the spectral transmission of air as shown in Figure 1.4, the suitable operating wavelength for most pyrometers can be less than  $1 \mu m$ , 3 to  $4 \mu m$ , or 8 to  $14 \mu m$  because less absorption appears among these wavelength ranges. Moreover, the ratio between changes in radiance and in temperature depends on the inverse of wavelength [Maxwell, 2005]. Thus, radiation thermometers with shorter wavelength are required for sensitive measurement.

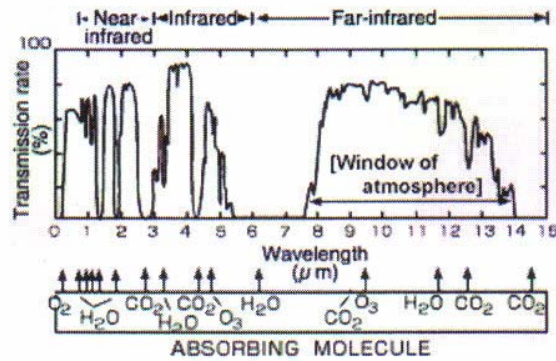


Figure 1.4: Infrared transmission spectrum of atmosphere [Maxwell, 2005].

Optical pyrometers, which are also called light-pipe radiation thermometers (LPRTs), used in this research can operate in the wavelength range of  $0.954 - 0.957 \mu\text{m}$ . This operating wavelength will be discussed later in chapter 3. LPRTs are currently becoming important tools for high temperature measurement in many industries, especially in semi-conductor manufacturing. Traditionally, they are attractive in radiometric temperature measurement because of their small size, easy installation, and their non-contact nature. The non-contact nature is particularly important since the LPRTs do not alter or damage the original wafer surface and minimally disturb the wafer temperature compared to contact thermometers or lens-type radiometers, which generally require larger viewing apertures. Furthermore, they are not affected by shock, vibration, and other adverse environments, and the high numerical apertures of LPRT sensors greatly minimize any effects of the variability in optical properties across the wafer [Tsai, 2003].

The main component of a typical LPRT system, CI-Systems NTM 500-R, is a quartz or sapphire crystal rod that collects the spectral radiance of an object surface at the LPRT tip and transmits it through a flexible optical fiber cable to a photo-detector.

Besides the detector, the control box or the base unit contains the electronics necessary to digitize the measured electrical signal and to convert it into the spectral radiance temperature ( $T_\lambda$ ). Figure 1.5 is a photograph of NTM 500-R LPRT system. This system operates in the temperature range of 400 °C to 1,250 °C with a sampling rate of 0.5 Hz to 30 Hz.



Figure 1.5: NTM 500-R LPRT system.

With Planck's law, which only applies for a blackbody, and Wein's distribution, the true temperature ( $T_{rad}$ ) of the emitting surface which varies from the spectral radiance temperature can be obtained through the following equation [Dewitt and Nutter, 1988]:

$$\frac{1}{T_{rad}} = \frac{1}{T_\lambda} + \frac{\lambda_{eff}}{c_2} \ln \varepsilon_{eff} \quad (1.4)$$

where  $\lambda_{eff}$  is the operating effective wavelength of the LPRT and  $\varepsilon_{eff}$  is the effective spectral emissivity of the observed surface.

To calibrate the LPRT system, a calibration wafer embedded with thin-film thermocouples is used to compare their temperature readings with the readings recorded

by the LPRT. These thermocouples given acceptable accuracy and repeatability are traceable to the International Temperature Standard of 1990 (ITS-90), which will be discussed in section 2.1. This calibration process is done in an RTP test bed that establishes a uniform heating environment.

### **1.3 SCOPE OF RESEARCH**

The University of Texas developed a thermometry test bed providing an environment for testing and evaluating various wafers and LPRT systems. This test bed, an instrumented vacuum furnace, utilizes an axisymmetric design and uses a multiple zone ceramic heater that allows silicon test wafers to be uniformly heated to temperature up to  $1,250^{\circ}C$ . Using this furnace and positioning the LPRT at the geometric center location under the instrumented wafer, it has been found that there is an offset of  $10^{\circ}C$  to  $30^{\circ}C$  between the temperature readings obtained from the LPRT and from the wafer thermocouples in a temperature range of  $500^{\circ}C$  to  $800^{\circ}C$  [Tan, 2002].

To find the sources of this error and achieve the uncertainty of  $\pm 1.5^{\circ}C$  at the temperature of  $1,000^{\circ}C$  as required by the International Technology Roadmap for Semi-conductor 2004 (ITRS-2004), there are several factors that have to be considered. The objective of this research is to understand the behavior of fused silica, fused quartz, and sapphire LPRT sensors, and to provide the fundamental knowledge required to advance this critical sensor technology.

Using the temperature measurement equation (equation 1.4), the effective wavelength has to be determined in order to achieve an accurate surface temperature result from the LPRT spectral radiance temperature. In addition, the bandwidth of this effective wavelength can be applied in calculating temperature uncertainty. The spectral characterization of LPRTs will be performed by using an infrared spectroradiometer which consists of an integrating sphere spectral reflectance attachment, a

monochromator, and a source attachment. The incident light beam from the tungsten lamp source is spectrally filtered through the monochromator and collected by the LPRT sensor. A linear translation stage is used for aligning the center between the LPRT tip and the monochromator's exit.

The thermal environment surrounding the LPRT can be another factor influencing the accurate temperature indicated by the LPRT sensor. Characterizing this environmental effect helps to minimize the measurement uncertainties and provides the range of necessary thermal environment temperatures for LPRT calibration. The experimental study is done by using a tube furnace to create the hot radiative environment while the LPRT tip is collecting radiation from a constant radiance blackbody source. The quality of LPRT measurement is also affected by any radiation scattering from the lateral surface along the length of the light-pipe. Ideally, only the tip of the LPRT collects radiation. If there are surface imperfections on the light-pipe probe, external radiation can leak into the side of LPRT and the thermal environment causes an error in LPRT readings. To determine whether such defects are contributing to differences in calibration, three different surface roughness LPRTs are examined in this research. The experimental results from both effects, thermal environment and rough surface, will be compared with the computer-model results calculated by Yan Qu. The details of determining the effective wavelength and the thermal environment effect will be described in Chapter 3.

Another source of error in the LPRT measurement is the stray radiation reaching the light-pipe due to the separation distance of the light-pipe tip from the object being measured which is discussed in Chapter 4. With increased distance, the light-pipe itself has more chance to receive extraneous radiation causing an increased temperature difference between the object temperature and the light-pipe indicated temperature. On

the other hand, if the separation distance decreases, the LPRT will conduct heat away from the object surface since it acts as a heat sink. This will cause a localized depression in the object temperature. Its magnitude is inversely proportional to the gap between them, such that the smaller the distance is, the more the heat loss will be. To determine this effect, a second experimental system has been designed. Using the linear translation stage, the LPRT can be manipulated to move vertically. According to equation 1.4, any variations in the effective spectral emissivity can lead to errors in the predicted temperature values. Silicon wafer emissivity can vary greatly with temperature, wavelength, wafer location, surface topography, and surface composition [Tsai, 1999]. This emissivity value is unknown. Furthermore, the silicon wafer is semitransparent, so radiation from the heat source can pass through the wafer and be transmitted to the light-pipe. Therefore, instead of measuring the temperature of the silicon wafer, an instrumented ceramic plate and a molybdenum plate painted with flat black ultra-high-temperature paint are used as the objects in this experiment.

Comparison of measured and predicted values is done. The predicted values are obtained by using a numerical method. The radiative environment of the chamber and the effect of the ceramic and molybdenum disk radiatively interacting with the light-pipe are modeled using a complete set of properties as can be found to provide input conditions for the light-pipe model. This coupled analysis of the chamber and light-pipe system can be used to find the relative error in light-pipe radiometric temperature measurement caused by the separation distance.

The last factor that is investigated in this research is the acceptance angle for the typical light-pipe. The acceptance angle will also be discussed in Chapter 4. As discussed earlier, an LPRT may collect more radiation from the surroundings when the light-pipe moves further away from the object. This can happen if its acceptance angle is large. In

order to determine this angle, the light-pipe tip collects the light beam from a laser pointer having a wavelength close to the wavelength of the detector. This experiment is done by adjusting the laser pointer in small angular increments. A portion of this laser beam is transmitted through the length of the light-pipe and emerges at the other end. Therefore, we can measure the range of acceptance angles of the light-pipe. This experimental result is then compared with the predicted values.

## **Chapter 2: *Uncertainty Analysis***

### **2.1 BACKGROUND**

For all temperature experimentation, it is hard to obtain the same result for each repetition of the measurement. The best conclusion on how well these different measured values represent reality is to compare with the actual ‘true’ value, which is unknown. The difference between these two types of values is called the measurement error which is categorized into two groups: systematic error and random error.

Systematic error, also called bias error or absolutely constant error, tends to shift the sample mean, which results from a large number of measurements under repeatable operating conditions, away from the true value of a measurand. Examples of systematic error sources are uncalibrated equipment, resolution error, experimental oversights, errors in theory, and imperfect observations [Nicholas and White, 1994]. Random error is defined as a scatter between the measured data and the mean result of a large number of repeated measurements. The random error is usually associated with system sensitivity, round-off error, errors caused by small changes in environmental condition such as temperature changes, vibrations, etc., and operator errors [Gertsbakh, 2003].

As mentioned earlier, the true value is forever unknown, so the actual error cannot be estimated. The only estimation that can be done based on the results from the measurement is to calculate a range of probable error where the true value must fall. This estimation is called the uncertainty analysis. The quality of an uncertainty analysis will depend equally on the measured variable, the quality of the equipment, the knowledge of the operator, and the measurement intent [Bentley, 1998]. According to the international metrology standard, there are two components in the uncertainty analysis which are type

A and type B errors. These are similar to the random and systematic errors, respectively, and will be discussed in the following section.

A complete temperature measurement result must include the measured value after application of all necessary corrections and an uncertainty, and be traceable to the International Temperature Scale of 1990 (ITS-90). This standard is realized by a set of the thermometric fixed points as listed in Table 2.1, and provides the method and the specified interpolation formulae between each of the fixed points. The temperature fixed points, defined as the melting point, the freezing point, and the triple point of various pure substances, are highly accurate and reproducible. In order to transfer the fixed temperature values with small uncertainty to any practical temperature measuring instruments, the standard platinum resistance thermometer (SPRT) must be used along with the accurate ITS-90 interpolation equations showing the relationship between temperature and resistance.

## **2.2 SOURCES OF UNCERTAINTY**

Every measuring sensor defined as an output value must be calibrated against the reference standard which is a known input value in order to characterize its precision. This calibration process will not be completed without uncertainty. Normally, most measurement has more than one source of calibration uncertainty. The main factors that contribute to the uncertainty calculation, especially in temperature measurement, are repeatability, reproducibility, resolution, hysteresis, reference-instrument precision, stability and uniformity of the calibration medium, and drift. These uncertainty sources will be discussed in more detail below:

Equilibrium state	Temperature	
	$T_{90}$ (K)	$t_{90}$ (°C)
Triple point of hydrogen	13.8033	-259.3467
Triple point of neon	24.5561	-248.5939
Triple point of oxygen	54.3584	-218.7916
Triple point of argon	83.8058	-189.3442
Triple point of water	273.16	0.01
Melting point of gallium	302.9146	29.7646
Freezing point of Tin	505.078	231.928
Freezing point of zinc	692.677	419.527
Freezing point of silver	1234.93	961.78
Freezing point of gold	1337.33	1064.18
Freezing point of copper	1357.77	1084.62

Table 2.1: Temperature fixed points defined by ITS-90 at 1 atm [Figliola and Beasley, 2006].

The term “repeatability” means the variation characteristic in the measurement results taken under the same conditions. These duplicate conditions consist of the same measurement method, the same person, the same measuring instrument, the same location, and repetition over a short period of time [Taylor and Kuyatt, 1994]. The reproducibility of measurement results is similar to the repeatability except that it is obtained under changed conditions of measurement. The changed specification of the conditions include principle of measurement, measurement process, observer, measuring instrument, reference standard, location, conditions of use, and time [Taylor and Kuyatt,

1994]. The repeatability and reproducibility are evaluated by using the statistically estimated standard deviation.

The resolution represents the smallest scale increment that any data provided by the measuring instrument can scatter. For example, if the measured resistance obtained from the digital multimeter (DMM) is  $146.3178 \Omega$ , then the resolution of this meter is equal to  $0.0001 \Omega$ . The random uncertainty accounting for the instrument resolution, also called zero-order uncertainty, is an estimate of one-half of its digital least count.

Hysteresis is a property of an instrument whose readings do not return completely to their original state. The sequence of measurement is a useful technique for checking the hysteresis error. Figure 2.1 shows an ascending-descending sequential test curve for a platinum resistance thermometer (PRT) calibration. The amount of hysteresis error is determined by the maximum difference between upscale and downscale sequential readings. The half-width of this error value is used as an estimator of the uncertainty.

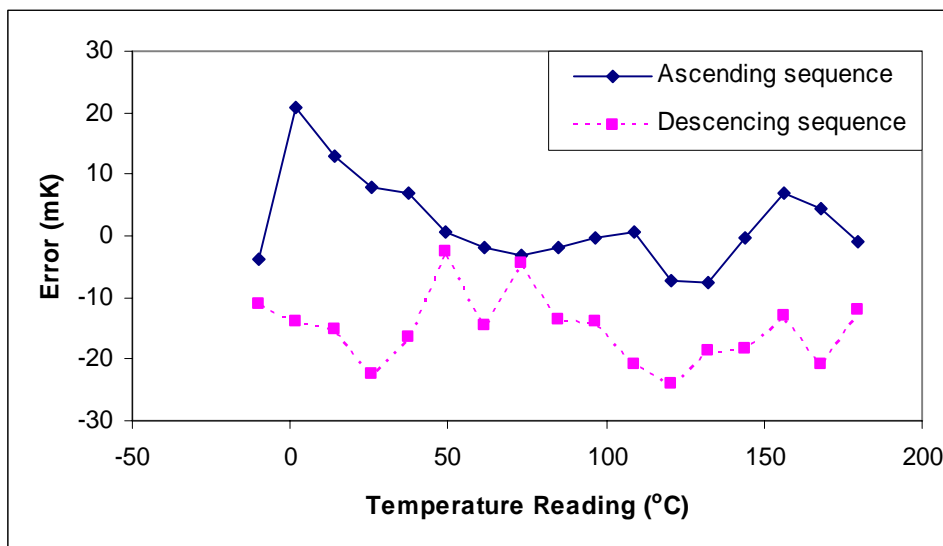


Figure 2.1: Example of PRT hysteresis error evaluation [Nicholas and White,1994].

Uncertainty sources associated with the instrument precision can be found either on the instrument specification called accuracy or on the instrument's calibration certificate called total uncertainty. The accuracy claimed by manufacturer and based on multiple lab tests is a type of the random error of an instrument. The value reported on the certificate is usually smaller than on the specification, and it is very important that the instrument certificate must use the same level of confidence as the total measurement uncertainty.

Inserting the temperature sensor into a well-controlled calibration bath, furnace, or cryostat at different positions will always give different readings. Ideally, the measured results should be the same. The magnitude of these temperature differences is caused by a fluctuating component and a steady component which leads to random and systematic variations in the thermometers' readings, respectively. Random fluctuation also known as stability is not a significant number and normally is counted as a part of repeatability uncertainty. A systematic component is contributed by temperature gradients or non-uniformity of the bath. These two values, stability and uniformity, can be found from either the manufacturer's specification or calibration certificate.

Drift in any measuring instrument usually depends on how long a time and what method they have been used. In thermometry, this uncertainty source is caused by dimensional or compositional changes [Nicholas and White, 1994]. In order to predict the drift rate, the history of each instrument must be known. Annual calibration is the best way for obtaining this specific information. For brand-new instruments, the half-width of the hysteresis curve is a good indicator of the expected drift.

### **2.3 UNCERTAINTY CHARACTERISATION**

According to the ISO Guide to the Expression of Uncertainty in Measurement recommended by the International Committee for Weights and Measures (CIPM), the

expression of uncertainty in measurement can be divided into two groups which are type A and type B standard uncertainties. These two types of uncertainty are categorized by the method of approach used to evaluate the uncertainty values. In typical measurement having more than one source of uncertainty, there are two ways in which the overall uncertainty can be reported in a calibration certificate: combined standard uncertainty and expanded uncertainty. All types of uncertainty are discussed in the following sections.

### 2.3.1 TYPE A COMPONENT

The evaluation method for type A standard uncertainty is typically based on two values: 1) the square root of the estimated variance, namely the standard deviation,  $\sigma$ , which is obtained from the statistical analysis of a set of  $n$  independent observations, each measurement represented by  $x_i$  where  $i = 1, 2, \dots, n$ , under identical operating conditions, and 2) the sample size,  $n$ . Thus, type A uncertainty or standard deviation of the means can be expressed as

$$u(x) = \frac{1}{n} \left[ \frac{1}{(n-1)} \sum_{i=1}^n (x_i - \bar{x})^2 \right]^{1/2} \quad (2.1)$$

where  $\bar{x}$ ,  $(x_i - \bar{x})$ , and  $(n-1)$  are called the mean value, the deviation of  $x_i$  and the degrees of freedom given as  $\nu$ , respectively. The degrees of freedom are defined as the difference between the number of taken data and the number of parameters used in estimating that data.

However, if a set of experimental results is represented by a function of some independent variables, equation (2.1) has to be modified using what is called regressive uncertainty. Assume that a mathematical expression that shows the relationship between the dependent measured variable and the independent variable is in the form of a polynomial function as:

$$x_{c,i} = a_0 + a_1 y_i + a_2 y_i^2 + \dots + a_m y_i^m \quad (2.2)$$

where  $x_{c,i}$  is the predicted value given by a value of  $y_i$ . The constant coefficients,  $a_0, a_1, \dots, a_m$ , are determined by the least-square method of curve fitting based on  $n$  measurements. The highest order,  $m$ , is also restricted by the number of measurements which  $m$  is less than or equal to  $(n-1)$  [Figliola and Beasky, 2006]. The type A scattering uncertainty can be now calculated by using the difference between the measured and predicted values as shown in Figure 2.2 and expressed by:

$$u(x) = \frac{1}{\sqrt{n}} \left[ \frac{\sum_{i=1}^n (x_i - (a_0 + a_1 y_i + a_2 y_i^2 + \dots + a_m y_i^m))^2}{(n - \rho)} \right]^{1/2} \quad (2.3)$$

where  $x_i$  and  $\rho$  are the measured data and the number of coefficients, equating to  $(m+1)$  for this function, respectively. The term in brackets is referred to as the standard error of the fit or the standard error of estimate (SEE).

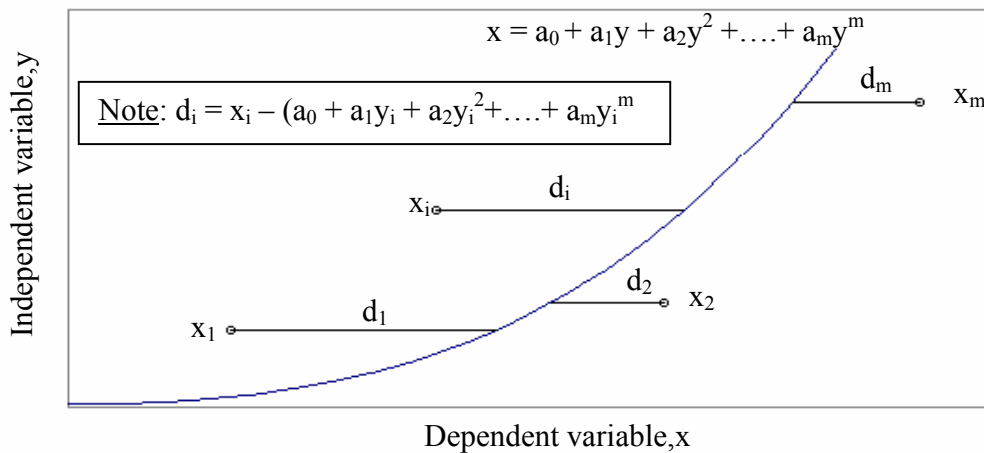


Figure 2.2: The approached geometry of regression uncertainty.

### 2.3.2 TYPE B COMPONENT

The evaluation of type B uncertainty is usually based on scientific judgment other than statistical means as with type A standard uncertainty. This scientific mean is determined by using all available information such as manufacturer's specification, calibration certificates or reports provided by other experimenters, handbooks, experience, intuition, and previous measurement data. The key in estimating this type of uncertainty is to determine the error distribution in measurements. In this section, two useful theoretical distributions that appear frequently in most metrological applications are discussed below.

The normal or Gaussian distribution commonly found in many fields represents that most of the measured data scatters close to their mean value with continuously fewer events/counts further from the mean. This normal probability distribution is also called a "bell curve" as shown in Figure 2.3 because its shape resembles a bell. In order to characterize the normal distribution, the probability density function for random variable  $x$  with mean true value  $\bar{x}$  and true variance  $\sigma^2$  is defined as

$$p(x) = \frac{1}{\sigma\sqrt{2\pi}} \exp\left(-\frac{(x-\bar{x})^2}{2\sigma^2}\right) \quad (2.3)$$

Integration of equation (2.3) over the interval  $\bar{x} \pm \delta x$  where  $\delta x \rightarrow 0$ , giving the area under  $p(x)$ , will provide the probability that any future measurement will lie in this interval. Therefore,

$$P(-z_1 \leq \beta \leq z_1) = 2 \left[ \frac{1}{\sqrt{2\pi}} \int_0^{z_1} e^{-\beta^2/2} d\beta \right] \quad (2.4)$$

where  $\beta = (x - \bar{x})/\sigma$  and  $z_1 = (x_1 - \bar{x})/\sigma$ . The equation (2.4) is also known as the normal error function. The results of this integration estimated by lower and upper limits  $\bar{x} - z_1\delta$  and  $\bar{x} + z_1\delta$  yield that

$z_1 = 1.0$ : 68.27% of measurement  $x$  lies within  $\pm 1\sigma$  of  $\bar{x}$ ;

$z_1 = 2.0$ : 95.45% of measurement  $x$  lies within  $\pm 2\sigma$  of  $\bar{x}$ ;

$z_1 = 3.0$ : 99.73% of measurement  $x$  lies within  $\pm 3\sigma$  of  $\bar{x}$ .

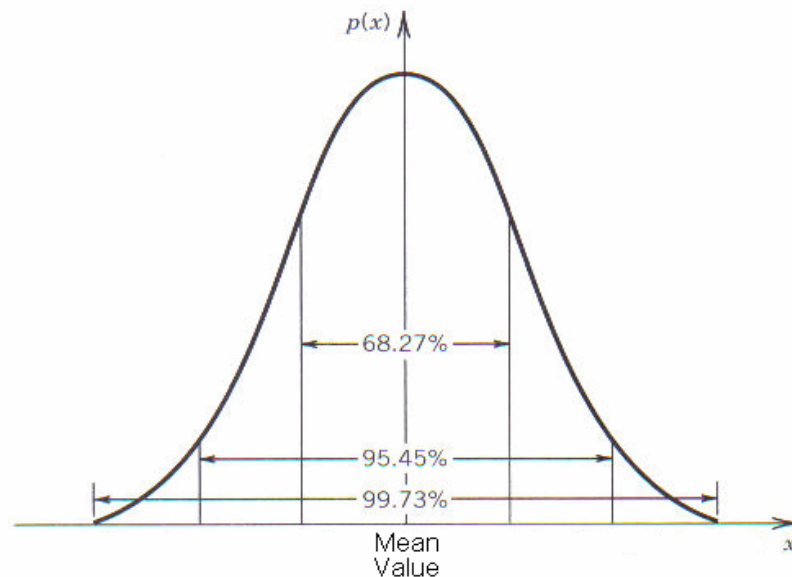


Figure 2.3: Normal or Gaussian probability distribution [Figliola and Beasley, 2006].

The second widely used distribution is called the rectangular or continuous uniform distribution, which has equal probability for any measured value to fall within a certain symmetric interval given by  $a$  and  $b$ . The probability density function of the rectangular distribution is thus:

$$f(x) = \frac{1}{(b-a)}, \quad \text{for } a < x < b \quad (2.5)$$

where  $f(x)=0$  for outside this range. The mean value,  $\bar{x}$ , and the variance,  $\sigma^2$ , are known exactly as  $(b+a)/2$  and  $(b-a)^2/12$ , respectively. Therefore, 100% of all measurements will lie within  $\pm\sqrt{3}\sigma$  of  $\bar{x}$ .

For characterizing type B uncertainty based on the above two distributions, all quoted uncertainty in the calibration certificate is usually assumed to be the normal distribution. Then, this standard uncertainty is calculated by dividing the quote value by the factor depending on a level of confidence. This factor is also known as the coverage factor (CL). A 95.45% confidence level is reported, for example, the dividing factor will be equal to 2.0. The rectangular distribution is applied when upper and lower limits are assigned such as specification of instrument (accuracy, resolution, etc.). This type B standard uncertainty is equal to the width of the interval divided by  $\sqrt{3}$ . Furthermore, this uniform distribution is also used in the absence of any other information [Husain and An-Anhdi, 2000].

### 2.3.3 COMBINING UNCERTAINTY COMPONENT

The reporting measurement result should be the combination between the measurand and its uncertainty which is either the combined or expanded uncertainty. In term of the combined standard uncertainty,  $u_c$ , discussed in this section, it is defined as the positive square root of the summation of the squares of all type A and type B uncertainties. However, the problem in determining the combined uncertainty of measured values arises when the value measured in an experiment is affected by other variables whose uncertainties are known in terms of some other quantity. In statistics, this is called propagation of uncertainty or propagation of error. To explain how these uncertainties propagate to the measured result, a general relationship between independent random mean variables  $\bar{Y}$  and  $\bar{Z}$  with the uncertainties of  $u_Y$  and  $u_Z$ , respectively, and a mean value of measured variable  $\bar{X} \pm u_X$  is assumed by

$$\bar{X} \pm u_X = f(\bar{Y} \pm u_Y, \bar{Z} \pm u_Z) \quad (2.6)$$

An approximate expression for  $\bar{X}$  is obtained by using a Taylor series expansion around the mean values of  $\bar{Y}$  and  $\bar{Z}$  given by

$$\bar{X} \pm u_X \approx f(\bar{Y}, \bar{Z}) \pm \left[ \left( \frac{dX}{dY} \right)_{Y=\bar{Y}} u_Y + \left( \frac{dX}{dZ} \right)_{Z=\bar{Z}} u_Z + \frac{1}{2} \left( \left( \frac{d^2 X}{dY^2} \right)_{Y=\bar{Y}} u_Y^2 + \left( \frac{d^2 X}{dZ^2} \right)_{Z=\bar{Z}} u_Z^2 \right) + \dots \right] \quad (2.7)$$

In a linearized approach for  $u_X$ , all higher-order terms in the right-hand side of equation (2.7) can be neglected so that only the first-order terms in bracket are retained. This assumption is valid only if  $u_Y$  and  $u_Z$  are sufficiently small and/or the partial derivative terms, which are called sensitivity coefficients showing how changes in Y and Z affect X, are small. Then, the relationship between the random error in the resultant X and the random errors in Y and Z can be expressed as

$$u_X = \left( \frac{dX}{dY} \right)_{Y=\bar{Y}} u_Y + \left( \frac{dX}{dZ} \right)_{Z=\bar{Z}} u_Z \quad (2.8)$$

Applying the second-power relation [Kline and McClintock, 1953], which is the square root of the sum of the squares (RSS), into the equation (2.8), the combining uncertainty of X can be written as

$$u_c(X) = \left[ \left( \frac{dX}{dY} \right)_{Y=\bar{Y}}^2 u^2(Y) + \left( \frac{dX}{dZ} \right)_{Z=\bar{Z}}^2 u^2(Z) + 2 \left( \frac{dX}{dY} \right)_{Y=\bar{Y}} \left( \frac{dX}{dZ} \right)_{Z=\bar{Z}} u(Y)u(Z) \right]^{1/2} \quad (2.9)$$

In case that the uncertainties  $u_Y$  and  $u_Z$  are uncorrelated of each other, the covariance  $u(Y)u(Z)$  vanishes. Therefore, the simple form for evaluating the combining

uncertainty of the multivariable relationship,  $x = f(y_1, y_2, \dots, y_N)$ , is usually presented as

$$u_c^2(x) = \sum_{i=1}^N \left( \frac{\partial f}{\partial y_i} \right)^2 u^2(y_i) \quad (2.10)$$

This above equation is also known as the law of propagation of uncertainty [Taylor and Kuyatt, 1994]. The measured value together with its combined standard uncertainty is approximately characterized as the normal or Gaussian distribution with 68 percent level of confidence.

#### 2.3.4 EXPANDED UNCERTAINTY COMPONENT

Another widely employed uncertainty is the expanded uncertainty,  $U$ , which is the combined standard uncertainty multiplied by a coverage factor,  $k$ . The value of  $k$  is a function of the t-estimator calculated from Student's t-distribution, percentage probability or level of confidence ( $P\%$ ), and effective degrees of freedom. Based on the Welch-Satterthwaite (WS) formula, the effective degrees of freedom can be computed as:

$$v_{eff} = \frac{u_c^4(x)}{\sum_{i=1}^n \frac{\left( \frac{\partial f}{\partial y_i} \right)^4 u^4(y_i)}{v_i}} \quad (2.11)$$

where  $v_{eff}$  is less than or equal to the summation of degrees of freedom of the standard uncertainty ( $u(x_i)$ ). For type A evaluation, the degrees of freedom will be either  $(n-1)$  or  $(n-\rho)$  depending on how the standard deviation is computed which is discussed in section 2.3.1. The degrees of freedom of type B standard uncertainty whose error is usually given as upper and lower limits can be assumed to be infinity because of less

probability lying outside these limits [Taylor and Kuyatt, 1994]. Therefore, the final reporting measured value is commonly written as

$$X = x \pm U, \quad \text{where } U = ku_c \quad (2.12)$$

associated with the confidence level P%.

As mentioned at the beginning of this chapter, every experimental result is subject to error. In order to report the measured value with higher confidence level on its accuracy, the uncertainty of measurement must be provided. Therefore, the method of calculating the expanded uncertainty, U, described in this chapter will be applied to determine the uncertainties in the experimental work to be described in later chapters.

$\nu$	Fraction P in percent				$\nu$	Fraction P in percent			
	68.27	90.00	95.45	99.73		68.27	90.00	95.45	99.73
1	1.84	6.31	13.97	235.8	15	1.03	1.75	2.18	3.59
2	1.32	2.92	4.53	19.21	20	1.03	1.72	2.13	3.42
3	1.20	2.35	3.31	9.22	25	1.02	1.71	2.11	3.33
4	1.14	2.13	2.87	6.62	30	1.02	1.70	2.09	3.27
5	1.11	2.02	2.65	5.51	35	1.01	1.70	2.07	3.23
6	1.09	1.94	2.52	4.90	40	1.01	1.68	2.06	3.20
7	1.08	1.89	2.43	4.53	45	1.01	1.68	2.06	3.18
8	1.07	1.86	2.37	4.28	50	1.01	1.68	2.05	3.16
9	1.06	1.83	2.32	4.09	100	1.005	1.660	2.025	3.077
10	1.05	1.81	2.28	3.96	$\infty$	1.000	1.645	2.000	3.000

Table 2.2: Student t-distribution [Taylor and Kuyatt, 1994].

## **Chapter 3: *Discussion on Thermal Environment Effect***

### **3.1 INTRODUCTION**

As mentioned in Chapter 1, light-pipe radiation thermometers used in rapid thermal processing measure the temperature of the silicon wafer which is placed inside the high-temperature chamber. Consequently, a partial sidewall area of LPRTs depending on the design of the RTP furnace is surrounded by hot radiative environment. The environmental radiation can cause a significant change in the temperature reading indicated by an LPRT when the surrounding temperature is higher than the measuring surface temperature. This is addressed as the “thermal environment effect”.

Meyer (2001) examined the influence of the effect of thermal environment on eight sheathed sapphire light-pipes and found that the measured temperature displayed by LPRTs continuously increased with an increase in their surrounding temperature. He concluded that careful selection of light-pipes can minimize an error caused by the thermal environment. A similar experiment to Meyer’s was done by using three different kinds of commercial light-pipes (fused silica, fused quartz, and sapphire) of 4-mm diameter and 18-inch (approximately 457 mm) length. The details of these experimental results including their corresponding uncertainty analysis will be described in the following section.

Based on Snell’s law which will be described in details in Chapter 4, the relation between the refractive angle and the angle of incidence depends on the ratio of refractive indices. If the refractive index ratio is  $(n_2/n_1) \geq 1.41421$ , the acceptance angle will be  $90^\circ$ . Therefore, since the refractive indices for fused silica/quartz and sapphire over the wavelength range between 265.2 nm and 3507.0 nm are 1.50003-1.40568 and 1.83360-

1.69504, and over the narrower spectral range of detector sensitivity are always greater than 1.41421, radiation from all incident angles can enter the light-pipe surface.

For an optically smooth sidewall of a light-pipe which has perfectly specular reflection, the radiation collected by the photo-detector will be only from the tip of the light-pipe probe. All extraneous radiation reaching the sidewall of the probe will either be reflected from or be transmitted through the probe with the same incident angle as shown in Figure 3.1. The light-pipe surface can be considered to be “optically smooth” only if the average length scale of surface roughness is much smaller than the effective wavelength of the light-pipe detector. This effective wavelength will be discussed in the following section.

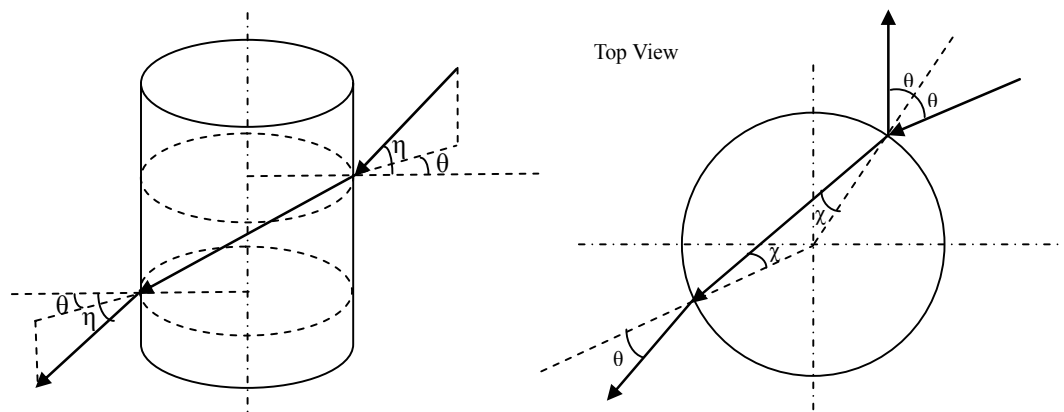


Figure 3.1: Illustration of a beam reaching the smooth sidewall of the light-pipe probe [Puttitwong, Qu, Howell, and Ezekoye, 2006].

### 3.2 DETERMINATION OF EFFECTIVE WAVELENGTH OF LPRT SENSOR

The actual temperature of the radiating target obtained by LPRTs can be calculated through the temperature measurement equation (equation 1.4). According to this equation, the operating effective wavelength of the LPRTs must be known. To characterize the spectral response of our photo-detector NTM 500-R LPRT system with

and without the light-pipes attached, an infrared spectroradiometer was used. This equipment operates at standard atmospheric pressure and at standard room temperature. The main components of the infrared spectroradiometer are an integrating sphere spectral reflectance attachment, a monochromator, and a source attachment as shown in Figure 3.2.

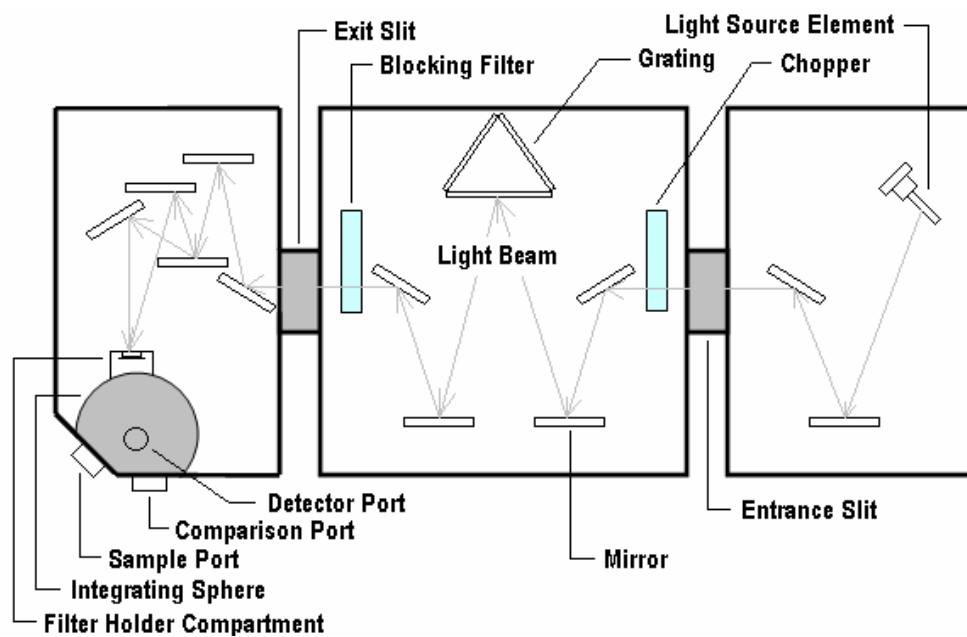


Figure 3.2: Schematic of the top view of optical layout for the spectroradiometric measurement system.

In the above figure, the light beam signal is generated by a light source which is either a 150-watt quartz-halogen lamp or an infrared-ceramic-nernst glower depending on the wavelength range that is required to enter the entrance slit of the monochromator. The incident light beam passes through a chopper with a frequency of 167.0 Hz. After being dispersed by the diffraction gratings consisting of 600 grooves/mm, 200 grooves/mm, 150 grooves/mm, and 75 grooves/mm (all of which operate at a particular wavelength

range) and filtered by a set of blocking filters, a certain wavelength of radiant beam enters the integrating sphere. Again, depending on the operating spectroradiometer range, there are two choices on the integrating sphere reflectance attachment which are either polytetrafluoroethylene powder (PTFE) or gold.

In the integrating sphere, the measured samples are positioned either in a sample port or in a filter holder compartment for determining reflectance or transmittance, respectively. Before starting the reflectance or transmittance measurement, a proper detector must be installed in the detector port. There are four types of detectors covering the wavelength range of 200 nm to 14,000 nm: Silicon (Si), PbS, PbSe, and HgCdTe. During the measurement, the processed signal sent by the detector proceeds to a computer where the final spectral results take form. Table 3.1 summarizes the operating wavelength ranges of the integrating sphere, source attachment, grating, and detector.

Wavelength (nm)			Wavelength (nm)		
Detectors	Si	200 – 1100	Gratings (grooves/ mm)	600	250 – 1100
	PbS	1000 – 3200		200	800 – 3500
	PbSe	1000 – 5000		150	1900 – 6500
	HgCdTe	1000 – 14000		75	5500 – 14500
Light Sources	Lamp	250 – 3500	Spheres	PTFE	250 – 2500
	Glower	1000 – 40000		Gold	2000 – 18000

Table 3.1: Overview of wavelength range for each component.

The operating wavelength range of the light-pipe detector can be characterized by using this infrared spectroradiometer system without the integrating sphere spectral

reflectance attachment. The detector with and without a light-pipe probe fixed on a linear translation stage was aligned with the center of the monochromator's exit slit. The quartz-halogen lamp and the grating of 600 grooves/mm were used in this measurement. It is noted that, for evaluating the sensitive wavelength, the duration time for recording the data at each step of wavelength was set to 3 minutes. The response curves as a function of wavelength, starting from 880 nm to 1,060 nm with an increment of 10 nm, for the detector with and without fused silica, fused quartz, and sapphire light-pipes are depicted in Figure 3.3.

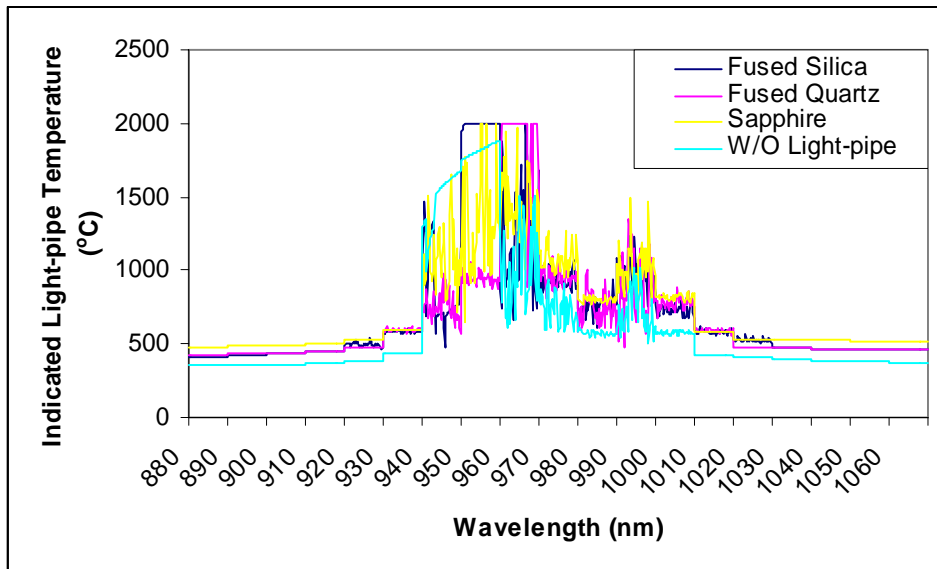


Figure 3.3: Comparison of response curves at the current of 5.5 A and at different wavelength for the detector with and without light-pipes attached.

From Figure 3.3, it can be seen that the characteristics of these response curves are similar. Their peaks occur at a wavelength between 950 nm and 960 nm. As mentioned earlier, the radiating temperature of a quartz-halogen lamp is as high as 2,700 °C; however, the maximum temperature that our detector can detect is 2,000 °C and the

lamps saturated the detector when operated at high temperature. Therefore, these response peaks may be at either one of these specific wavelengths or the others. The next experiment with similar set-up was performed by lowering the electric current supplying the quartz-halogen lamp in order to decrease the maximum temperature readings indicated by the LPRT. Figure 3.4 shows the spectral temperature profiles for the detector with fused silica light-pipe at the current of 5.5 A, 4.0 A, and 2.5 A. It appears that the peak was dropped to approximately 1,000 °C at 4.0 A and 750 °C at 2.5 A from 2,000 °C at 5.5 A. The range of effective wavelength was also expanded to between 950 nm and 970 nm instead of between 950 nm and 960 nm.

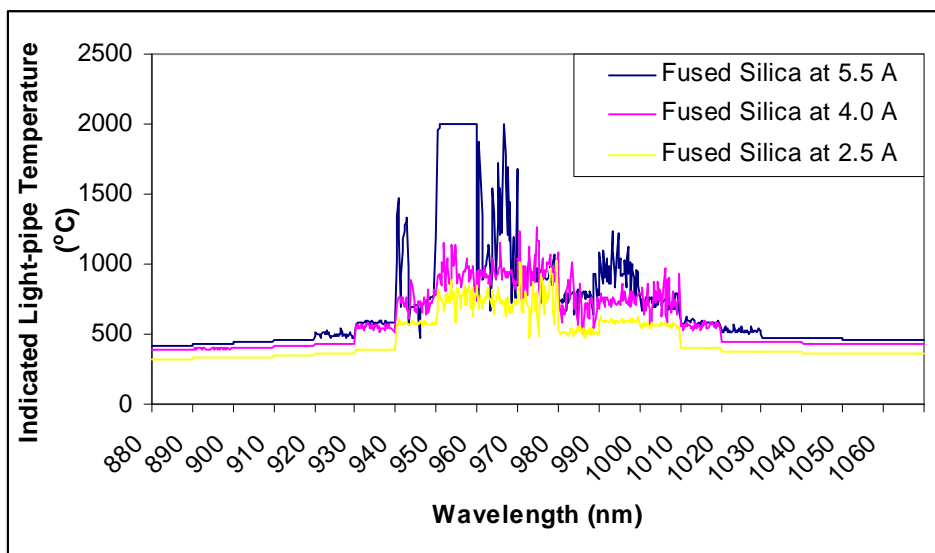


Figure 3.4: Comparison of response curves at different wavelength and different applied current for the detector with fused silica light-pipe.

To achieve a better determination of the sensitive wavelength range, another experiment was done at the wavelength between 910 nm and 990 nm with an increment of 1 nm. It is noted that the electric current of 5.5 A used in the spectroradiometer system is recommended by the manufacturer. Consequently, before beginning this experiment,

the LPRT was calibrated against the blackbody source in which the blackbody temperature was set to 1,100 °C while the fused silica light-pipe temperature was forced to read the temperature of 400 °C instead of 1,100 °C. The average temperature readings over the 3 minutes of recording time for each wavelength are illustrated in Figure 3.5. Figure 3.6 shows the spectral relative intensity calculated by using the equation (1.1). The result showed that the range of the effective wavelength of the LPRT is between 954 nm and 957 nm with the expanded uncertainty of  $\pm 1.3$  nm at 95.5 % confidence level. This expanded uncertainty, which was calculated by using the method discussed in Chapter 2, was accounted for the wavelength resolution of 1 nm and the wavelength accuracy of 0.05% of wavelength reading claimed by the manufacturer.

In order to calculate the value of operating effective wavelength from Figure 3.6, Dewitt and Nutter (1988) introduced the concept of mean effective wavelength by starting with the ratio of spectral radiances at  $T_1$  and  $T_2$ , and replaced it by  $I_1$  and  $I_2$  as:

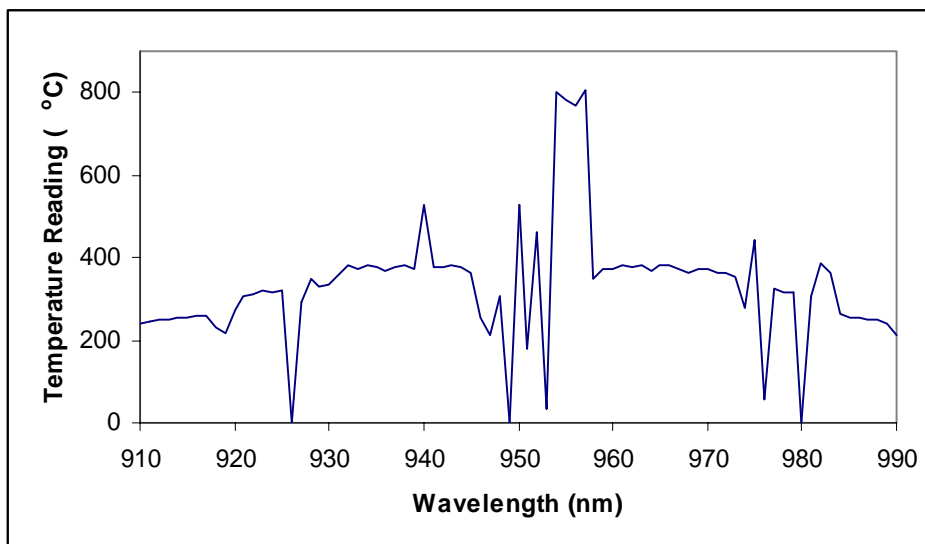


Figure 3.5: Temperature readings versus wavelength for the detector with fused silica light-pipe.

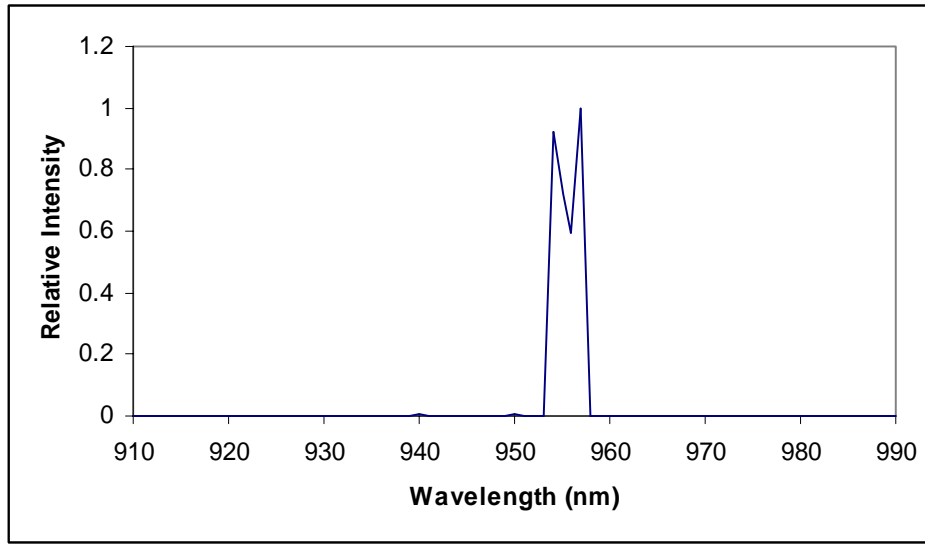


Figure 3.6: Illustration of effective wavelength range of detector with fused silica light-pipe.

$$\frac{I_1}{I_2} = \exp \left[ -\frac{c_2}{\lambda_{eff}} \cdot \left( \frac{1}{T_1} - \frac{1}{T_2} \right) \right] \quad (3.1)$$

Rewriting equation (3.1) in definite integral form gives

$$\frac{c_2}{\lambda_{eff}} \left( \frac{1}{T_1} - \frac{1}{T_2} \right) = \int_{I_1}^{I_2} \frac{dI}{I} \quad (3.2)$$

By taking the limit of both sides of equation (3.2), and defining a common temperature  $T$  as approached by  $T_1$  and  $T_2$  and the limiting effective wavelength  $\lambda_T$ , we have:

$$-\int_{\frac{1}{T_1}}^{\frac{1}{T_2}} \frac{c_2}{\lambda_T} d \left( \frac{1}{T} \right) = \int_{I_1}^{I_2} \frac{dI}{I} \quad (3.3)$$

Furthermore, Dewitt and Nutter (1988) claim that  $1/\lambda_T$  can be expressed as a linear function of  $1/T$ . Therefore, by equating the left sides of equations (3.2) and (3.3), and by substituting the linear equation of  $1/\lambda_T$ , the resulting expression will be able to be integrated to give the final expression of the mean effective wavelength as:

$$\frac{1}{\lambda_{eff}} = \frac{1}{2} \cdot \left( \frac{1}{\lambda_1} + \frac{1}{\lambda_2} \right) \quad (3.4)$$

where  $\lambda_1$  and  $\lambda_2$  are the wavelengths at  $T_1$  and  $T_2$ , respectively. Now, the true LPRT temperature reading can be calculated by applying the operating effective wavelength, obtained from placing the lower and upper limits of sensitive wavelength range of detector which is 954 nm and 957 nm in equation (3.4), into equation (1.4). Thus, the operating effective wavelength should be equal to  $955.5 \pm 0.0$  nm instead of 950 nm, which is presently used in CI-NTM500 software for calculating the true light-pipe temperature. Applying these two different effective wavelengths with an effective spectral emissivity of 0.1 to equation (1.4), the error on the light-pipe temperature reading can be as high as approximately  $4.6 \pm 0.0$  °C.

### 3.3 EXPERIMENTAL SET-UP AND RESULTS

The experimental study for measuring the thermal environment effect, as illustrated in Figure 3.7, was done by using a commercial tube furnace in order to generate the hot radiative environment surrounding a 12-inch length of light-pipe while the LPRT tip was collecting radiation from a constant radiance blackbody source. To achieve the temperature uniformity inside the furnace, a Mullite Process Tube of outer diameter 25.4 mm enclosed the light-pipe, and each end of the tube furnace was also wrapped by 35 mm thick layer of K-wool insulation.

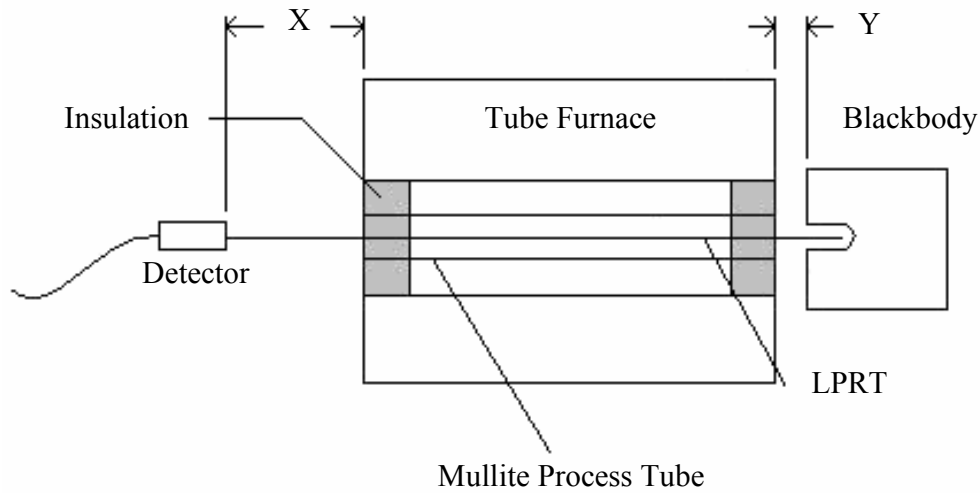


Figure 3.7: Schematic of experimental set-up.

Before beginning the examination, three LPRTs were calibrated against the blackbody source without turning on the tube furnace at 500 °C, 600 °C, 700 °C, and 800 °C, respectively, which are the same temperatures used during the experiments. While running the experiment, the furnace temperature,  $T_f$ , was adjusted from 21 °C up to 1,050 °C in approximately 100 °C increments. The experimental results of both furnace temperature and temperature displayed by the LPRT,  $T_{LP}$ , were recorded. The temperature difference between  $T_{LP}$  and  $T_{BB}$ , blackbody temperature, was then plotted as a function of  $T_f$  for the four different settings of  $T_{BB}$  of 500 °C, 600 °C, 700 °C, and 800 °C.

Since the control software for calibrating the CI-NTM500 LPRT system used in this research used a one-point calibration, there was an error in the measured temperature when the light-pipe temperature,  $T_{LP}$ , varied from the calibration point. In order to forecast this error, a second experiment was performed by using the blackbody source. First, the LPRTs were calibrated at 500 °C, and then the light-pipe readings were

collected when continuously increasing the blackbody temperature from the calibration temperature. The process was repeated for the other three temperature points as mentioned earlier. Linear correction factors expressed as  $T_{LP,act} = mT_{LP} + b$  can then be calculated by adding a trendline to each set of data. Both  $m$  and  $b$  values for each light-pipe at different blackbody temperatures are shown in Table 3.2. Figure 3.8 illustrates the example of results between before and after correction for three different kinds of light-pipe when the blackbody temperature is 500 °C.

After applying the linear correction factors along with their uncertainty to the measured temperature readings, the expanded measurement uncertainties of LPRTs were evaluated. The method for calculating the uncertainty including type A and B, combining, and expanded standard uncertainties is discussed in Chapter 2. The example of uncertainty for fused silica LPRT with  $T_f \approx 1,050$  °C and  $T_{BB} = 500$  °C is given in Table 3.3. The value of the coverage factor,  $k$ , was determined by using the Welch-Satterthwaite formula (Equation 2.11). The value corresponding to a  $t$ -factor for the 95.45% level of confidence is 2.00.

Light-pipe Materials	Values	Blackbody Temperature			
		500 °C	600 °C	700 °C	800 °C
Fused Silica	$m$	1.0265	1.0120	0.9933	1.0062
	$b$	-12.8970	-6.6551	4.8523	-4.0311
Fused Quartz	$m$	1.0212	1.0143	1.0002	0.9920
	$b$	-9.8560	-8.0259	-0.3162	6.5810
Sapphire	$m$	1.0523	1.0228	1.0039	1.0135
	$b$	-23.8760	-12.8500	-2.9941	-10.1780

Table 3.2: The values of  $m$  and  $b$  for linear correction factor equation.

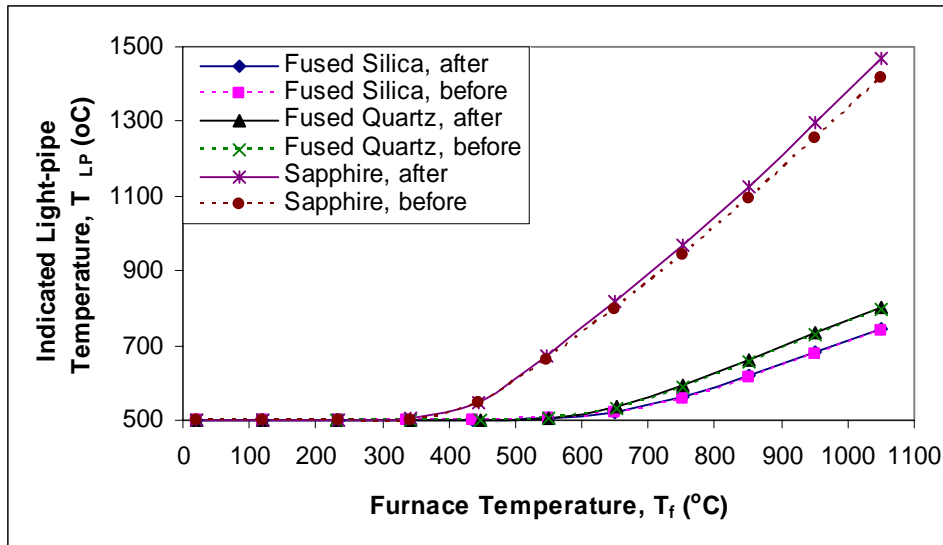


Figure 3.8: Comparison of measured temperature of three light-pipes before and after applying linear correction factors at the blackbody temperature of 500 °C.

Type	Source of uncertainty	Probability Distribution	Linear correction factor		
			A	B	C
A	Scatter of fitted curve	Normal	1	0.11	0.1
B	Calibration of blackbody	Normal	2	3.00	1.5
B	Resolution of blackbody reading	Rectangular	$\sqrt{3}$	0.50	0.3
B	Blackbody drift since last calibration	Rectangular	$\sqrt{3}$	0.01	0.0
B	Accuracy of detector	Rectangular	$\sqrt{3}$	8.12	4.7
B	Resolution of detector reading	Rectangular	$\sqrt{3}$	0.05	0.0
B	Hysteresis	Rectangular	$\sqrt{3}$	0.10	0.1
-	Combined standard uncertainty	Normal	-	-	4.9
-	Expanded standard uncertainty	Normal (k=2)	-	-	9.9

Light-pipe temperature					
A	LPRT reading repeatability	Normal	1	0.00	0.0
A	TC reading repeatability	Normal	1	0.00	0.0
B	Calibration of linear correction factor	Normal	2	7.06	3.5
B	Calibration of blackbody	Normal	2	3.00	1.5
B	Resolution of blackbody reading	Rectangular	$\sqrt{3}$	0.50	0.3
B	Blackbody drift since last calibration	Rectangular	$\sqrt{3}$	0.16	0.1
B	Resolution of detector reading	Rectangular	$\sqrt{3}$	0.05	0.0
B	Accuracy of type K thermocouple	Rectangular	$\sqrt{3}$	5.07	2.9
B	Accuracy of multimeter	Rectangular	$\sqrt{3}$	0.04	0.0
B	Accuracy of cold junction reading from multimeter	Rectangular	$\sqrt{3}$	0.02	0.0
B	Accuracy of cold junction TC	Rectangular	$\sqrt{3}$	1.70	1.0
B	Resolution of cold junction TC	Rectangular	$\sqrt{3}$	0.30	0.0
B	Resolution of TC reading	Rectangular	$\sqrt{3}$	0.30	0.0
B	Uniformity of tube furnace	Rectangular	$\sqrt{3}$	1.93	1.1
B	Stability of tube furnace	Rectangular	$\sqrt{3}$	0.13	0.1
B	Hysteresis	Rectangular	$\sqrt{3}$	0.10	0.1
-	Combined standard uncertainty	Normal	-	-	5.1
-	Expanded standard uncertainty	Normal (k=2)	-	-	10.1

Table 3.3: Example of uncertainty budget of fused silica light-pipe. A, B, and C are divisor, uncertainty value, and standard uncertainty, respectively.

The dominant uncertainty sources arise from the accuracy of the LPRT system itself and of the type-K thermocouple, which are 0.75% of reading or 5 °C and 0.75 % of reading or 2.5 °C, whichever values are greater, respectively. A single type-K thermocouple was used to measure the furnace temperature. The other major uncertainties are due to the blackbody calibration and the uniformity of tube furnace,  $\pm 3$  °C which are obtained from their specification.

Figures 3.9 to 3.11 present the results of the thermal environment effect on three different types of light-pipes including the expanded uncertainty value. For fused silica and fused quartz light-pipes, at each blackbody temperature ( $T_{LP, act} - T_{BB}$ ) increased dramatically when the furnace was heated to a temperature higher than the target temperature, as shown in Figure 3.9 and 3.10.  $T_{LP, act}$  represents the actual temperature indicated by LPRT after applying the linear correction factor. At the same furnace temperature, the ( $T_{LP, act} - T_{BB}$ ) for sapphire is much higher than for the other two types of light-pipe. The difference began to increase when  $T_f$  was still below  $T_{BB}$ , as illustrated in Figure 3.11. At the blackbody temperature of 500 °C and the furnace temperature of approximately 1,050 °C, the increase in  $T_{LP, act}$  from  $T_{BB}$  for sapphire could be at  $968.4 \text{ °C} \pm 22.0 \text{ °C}$  while it was  $245.8 \text{ °C} \pm 10.1 \text{ °C}$  and  $302.3 \text{ °C} \pm 10.9 \text{ °C}$  for fused silica and fused quartz, respectively. However, these temperature differences were always within  $\pm 2.9 \text{ °C}$  when the furnace temperature was less than the blackbody temperature by at least 160 °C for all three LPRTs.

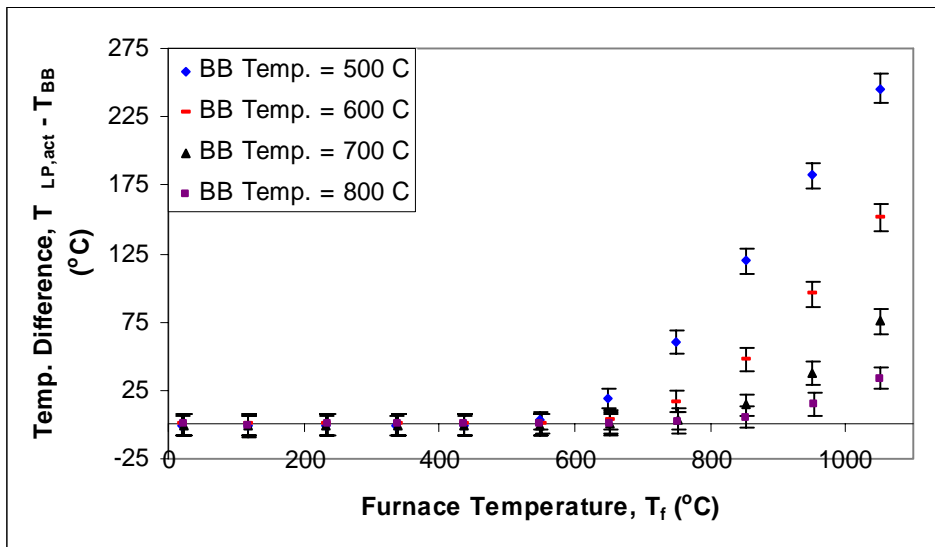


Figure 3.9: Actual temperature results displayed by fused silica light-pipe at four different blackbody temperature settings.

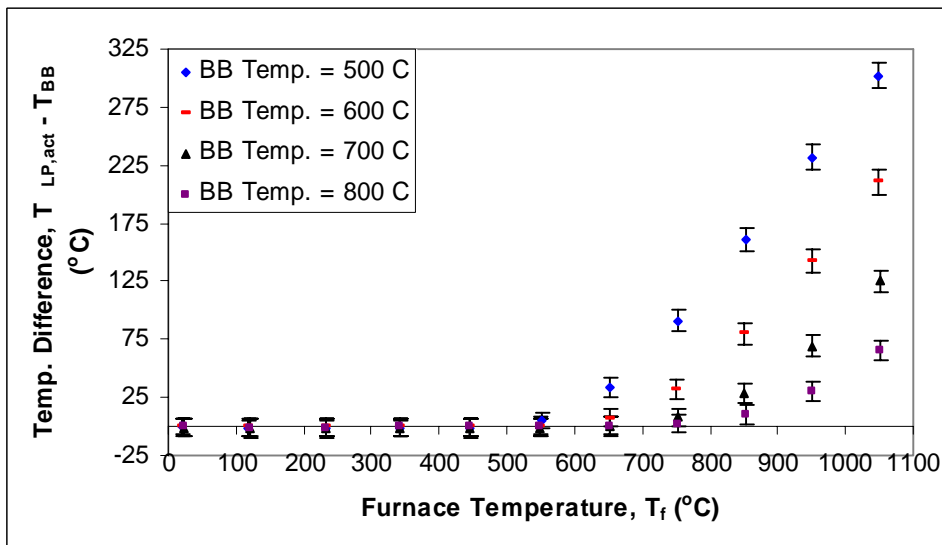


Figure 3.10: Actual temperature results displayed by fused quartz light-pipe at four different blackbody temperature settings.

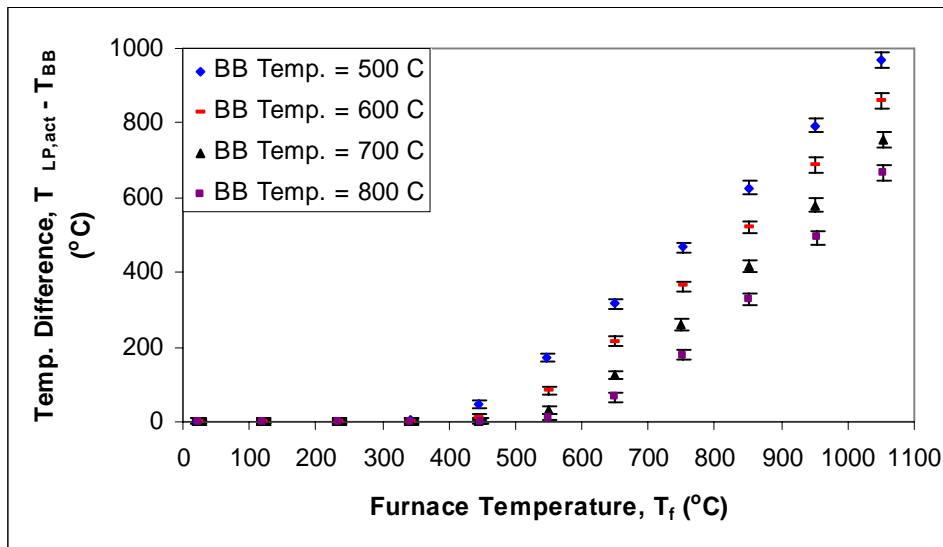


Figure 3.11: Actual temperature results displayed by sapphire light-pipe at four different blackbody temperature settings.

To explain why the temperature results obtained from three different light-pipes based on their radiative properties (transmittance and reflectance) are not exactly the same, the spectral transmittance of LPRTs was found using an infrared spectroradiometer, using samples of 2.5 cm diameter and 1.0 cm thickness. The results are shown in Figure 3.12. At the range of detector sensitive wavelength (954 - 957 nm), all three light-pipes have nearly 100% of transmittance.

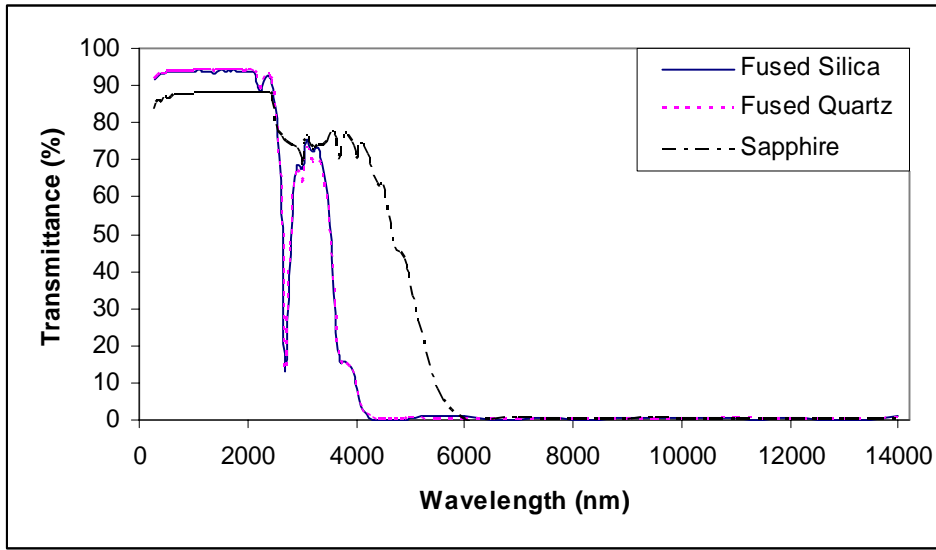


Figure 3.12: Spectral transmittances of three different LPRT materials at the normal incident angle  $\theta = 0^\circ$ .

The extinction coefficient,  $\kappa$ , shows how well the substance can absorb the electromagnetic radiation (EM waves). If the EM wave can easily pass through it, the extinction coefficient is low. Therefore, all light-pipe materials used in this research can be assumed to be ideal insulating materials ( $\kappa \rightarrow 0$ ). From the electromagnetic-theory, the reflectivity of the ideal insulating material having optically smooth surface can be decomposed into two components which are parallel and perpendicular to the incident surface. Both spectral reflectivities are a function of incident angle,  $\theta$ , and the ratio of spectral refractive indices as given in the following equations:

$$\rho_{\parallel}(\theta) = \frac{\left[ \left( \frac{n_2}{n_1} \right)^2 \cos \theta - \left[ \left( \frac{n_2}{n_1} \right)^2 - \sin^2 \theta \right]^{\frac{1}{2}} \right]^2}{\left[ \left( \frac{n_2}{n_1} \right)^2 \cos \theta + \left[ \left( \frac{n_2}{n_1} \right)^2 - \sin^2 \theta \right]^{\frac{1}{2}} \right]^2} \quad (3.5)$$

$$\rho_{\perp}(\theta) = \left\{ \frac{\left[ \left( \frac{n_2}{n_1} \right)^2 - \sin^2 \theta \right]^{\frac{1}{2}} - \cos \theta}{\left[ \left( \frac{n_2}{n_1} \right)^2 - \sin^2 \theta \right]^{\frac{1}{2}} + \cos \theta} \right\}^2 \quad (3.6)$$

where  $\rho_{\parallel}$  and  $\rho_{\perp}$  are the parallel and perpendicular components of the angular reflectivity. Applying the spectral refractive indices of light-pipes and air to the above equations, the angular reflectivity at the wavelength of 1,013.98 nm and the spectral reflectivity at normal incident angle ( $\theta = 0^\circ$ ) were found, as illustrated in Figure 3.13 and 3.14, respectively. The two components of reflectivity for all three light-pipe materials increase similarly as the incident angle increases.

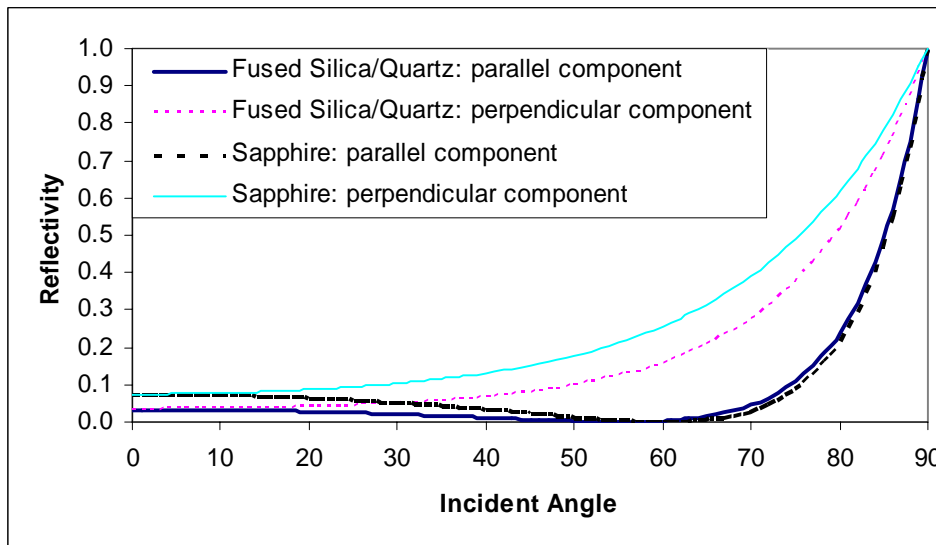


Figure 3.13: Reflectances of three different LPRT materials at the  $\lambda = 1,013.98$  nm.

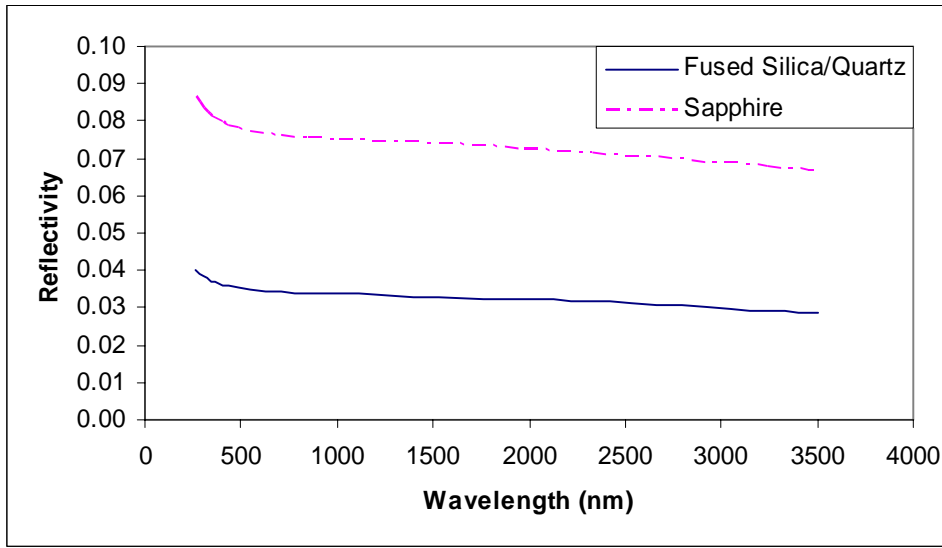


Figure 3.14: Spectral reflectances of three different LPRT materials at the normal incident angle  $\theta = 0^\circ$ .

It is noted that the values of the spectral refractive index for air is given by Cauchy's formula as:

$$n_{air}(\lambda) = 1 + A \left( 1 + \frac{B}{\lambda^2} \right) \quad (3.7)$$

where  $A = 28.79 \times 10^{-5}$ ,  $B = 5.67 \times 10^{11} \text{ cm}^{-2}$ , and  $\lambda$  is wavelength specified in cm. (Born and Wolf, 1993).

Because sapphire had higher reflectivity and lower transmissivity than the other two materials, less energy could be collected by the photo-detector causing a smaller thermal environment effect. But the results shown in Figures 3.8 to 3.11 trend in the opposite direction. This will be explained by experimental results presented below. Furthermore, the values of  $T_{LP, act} - T_{BB}$  between fused silica and fused quartz at each blackbody temperature should be the same because of the similar reflectance and transmittance. But the total metallic impurities present in fused quartz, which is

approximately 25-30 ppm, is higher than of fused silica ( $\approx 5$  ppm), so the multiple scattering inside the fused quartz light-pipe causes more environmental radiation (that would normally pass through the light-pipe) to be detected by the LPRT. The surface roughness of the light-pipe can be another explanation for this result. This also will be discussed in the following sections.

The experiment was repeated by both moving the tube furnace closer to the blackbody source ( $X = 44.5$  mm and  $Y = 25.5$  mm) and switching the ends of the light-pipes. Again, the LPRTs were calibrated against the blackbody source before running the tests. The results are shown in Figures 3.15 to 3.17. Also, the surface roughness of each half of light-pipe was randomly measured by using a Portable Surface Roughness Tester. Table 3.4 presents the surface roughness values for each of the three light-pipes. It can be seen that Figure 3.15 to 3.17 and Table 3.3 give consistent results. There is increased scattering from the inevitable flaws in the light-pipe surface which is consistent with higher external radiation leakage into the sides of the light-pipe.

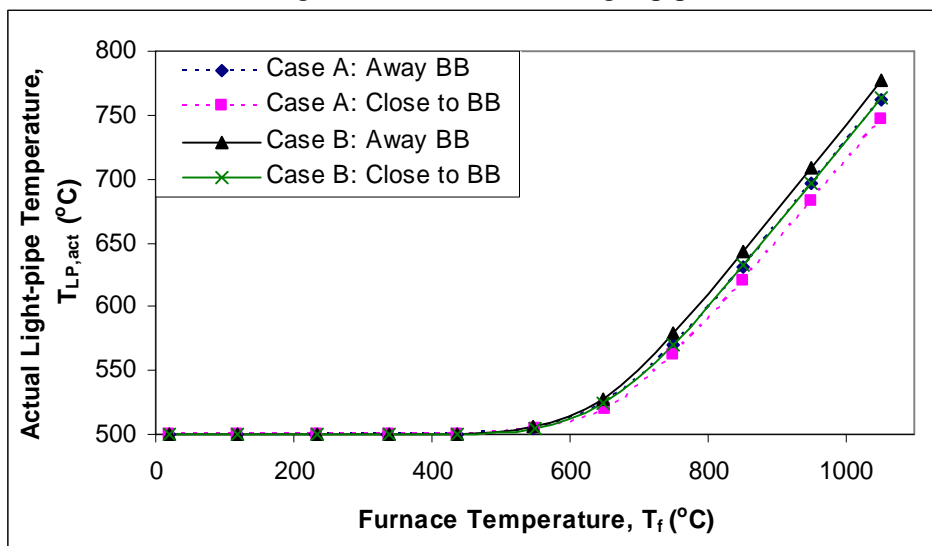


Figure 3.15: Comparison of temperature readings between different end and different furnace location of fused silica light-pipe at  $T_{BB} = 500$  °C.

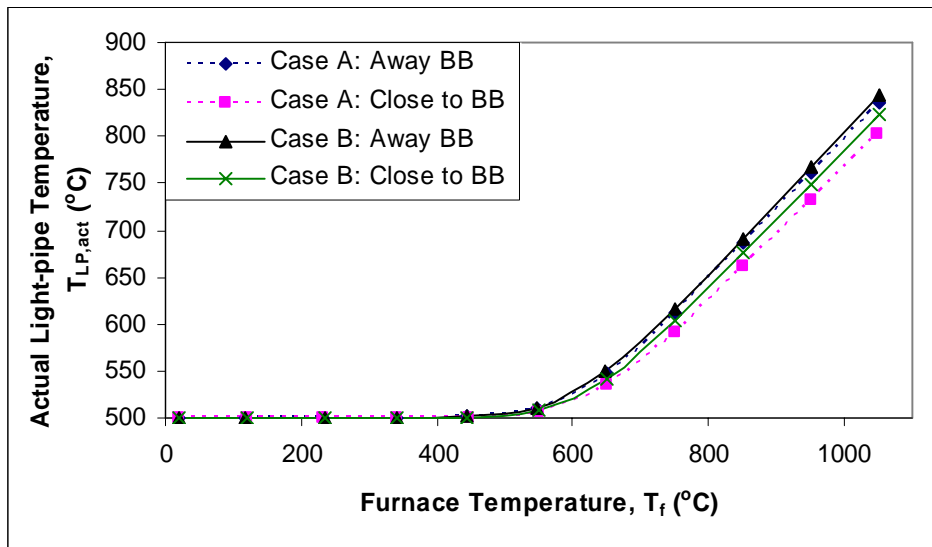


Figure 3.16: Comparison of temperature readings between different end and different furnace location of fused quartz light-pipe at  $T_{BB} = 500$  °C.

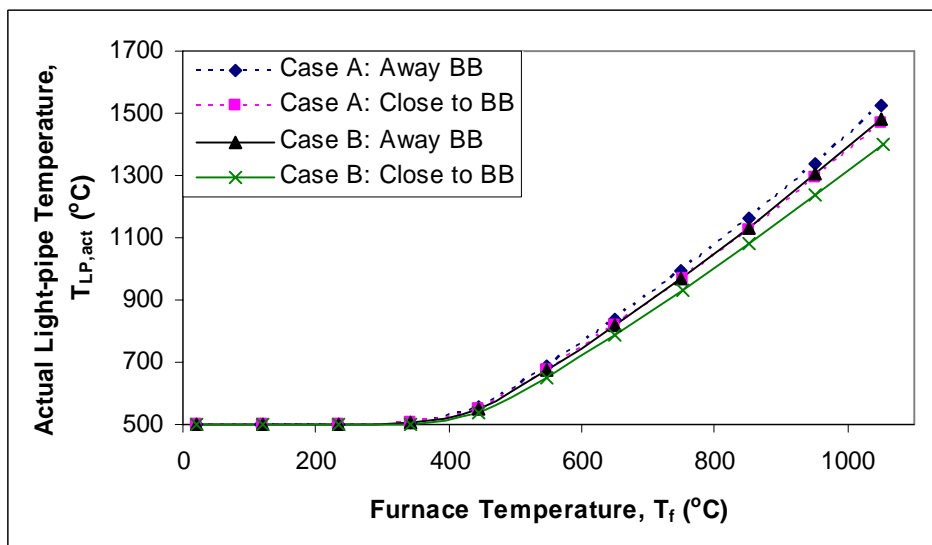


Figure 3.17: Comparison of temperature readings between different end and different furnace location of sapphire light-pipe at  $T_{BB} = 500$  °C.

To further investigate the effect of the microscopic flaws on a light-pipe surface, an experiment was done in which the fused silica light-pipe was roughened by two types of sandpaper in order to create different surface roughnesses. The experimental results for the various roughnesses shown in Figure 3.18 were compared. After the light-pipe was roughened, the indicated temperature of the LPRT began increasing at a lower furnace temperature than for a smooth surfaced light-pipe. When  $T_f$  was above 1,050 °C and  $T_{BB}$  was at 500 °C, the temperature reading indicated by the roughest-surface light-pipe was about 1,692.2 °C  $\pm$  25.6 °C while it was 746.8 °C  $\pm$  10.1 °C for the smoothest one. This is likely because when the average surface imperfection of the light-pipe is much larger than the detector sensitive wavelength, the material is optically rough resulting in non-specular reflections. Due to the non-specular property, more external radiation leaking into the light-pipe will be trapped inside and transmitted to the photo-detector causing a higher temperature reading.

As pointed out by Smith and Hering (1973), “At sufficiently long wavelengths and small solid angle of reflection, the contribution of the scattered component to energy reflected into the specular direction is negligible, and the expression for specular reflectance will be:”

$$\frac{\rho_{s,r}(\theta', \phi')}{\rho_{s,o}(\theta', \phi')} \cong \exp \left[ - \left( 4\pi \frac{\sigma_o}{\lambda} \cos \theta' \right)^2 \right] \quad (3.8)$$

where

$\rho_{s,o}$  and  $\rho_{s,r}$  = smooth and rough surface specular reflectivity

$\theta'$  = polar angle of incidence

$\phi'$  = azimuthal angle of incidence

$\sigma_o$  = optical rms height

$\lambda$  = wavelength

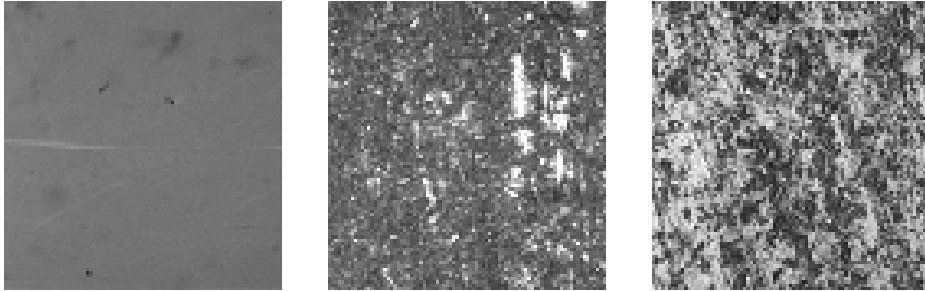
No.	Fused silica		Fused quartz		Sapphire	
	Case A	Case B	Case A	Case B	Case A	Case B
1	2.2	2.1	4.1	11.4	18.7	6.1
2	2.4	3.1	3.1	3.5	9.8	8.7
3	1.7	4.3	1.3	7.6	10.8	6.8
4	1.2	2.4	2.0	5.3	14.8	6.7
5	1.4	4.0	4.3	6.7	10.9	8.0
6	1.9	3.2	3.9	4.3	21.1	6.9
7	1.4	3.8	2.3	5.1	8.4	11.7
8	2.1	4.5	1.7	6.0	22.9	5.9
9	1.5	3.7	4.0	5.8	11.5	11.6
10	1.9	4.1	2.4	7.4	20.7	7.0
Avg.	1.77	3.52	2.91	6.31	14.96	7.94
Avg. ( $\mu m$ )	0.045	0.089	0.074	0.160	0.380	0.200
Uncertainty ( $\mu m$ )	$\pm 0.007$	$\pm 0.013$	$\pm 0.018$	$\pm 0.035$	$\pm 0.087$	$\pm 0.034$

Table 3.4: Surface roughness measurements in microinches for cylindrical surfaces at each end of LPRTs.

From the above equation, it can be seen that the specular reflectivity of a rough surface decreases to nearly zero when the surface roughness is large comparing to the effective wavelength. Therefore, the diffuse component of the reflectivity is dominant. In this case, the total reflectivity for fused silica light-pipe having the surface roughness of 0.28 and 0.77 microns is totally replaced by the non-specular part. The role of diffuse

reflectivity in the thermal environment effect will be discussed more in the following section.

a)



b)

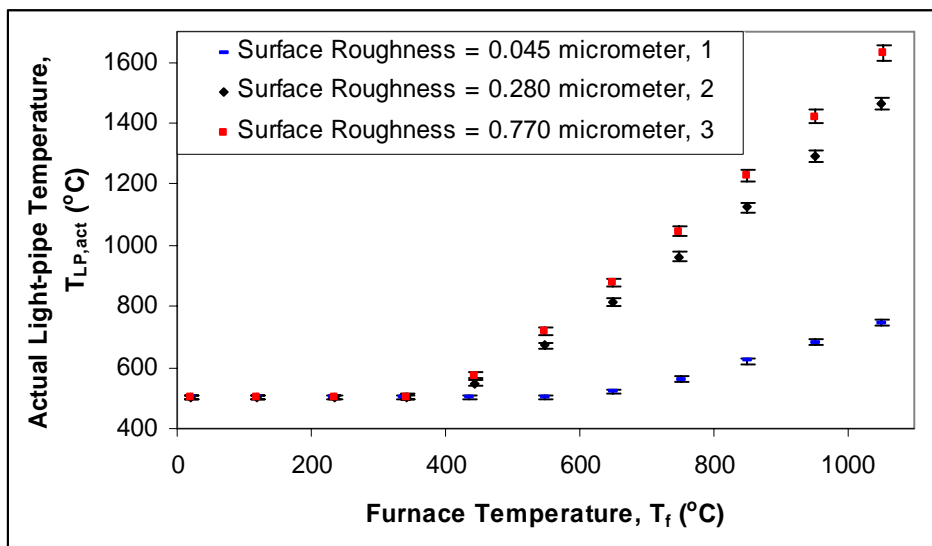


Figure 3.18: a) Magnified images at 500X of fused silica light-pipe with different surface roughness and b) Comparison of measured temperature readings among three different surface roughness values.

As mentioned earlier, less radiation leakage into an ideal sapphire light-pipe should happen compared to the fused silica. Examining Figures 3.17 and 3.18b at the furnace temperature of 1,050 °C, the temperature readings of sapphire case A (surface roughness = 0.38  $\mu m$ ) was 1,469.4 °C  $\pm$  22.0 °C and of fused silica rubbed by sandpaper

(surface roughness =  $0.28 \mu m$ ) was  $1,464.4 \text{ }^\circ\text{C} \pm 22.2 \text{ }^\circ\text{C}$ . Even though the sapphire was rougher than the fused silica, the readings were almost the same.

### 3.4 COMPARISON BETWEEN MEASURED AND COMPUTER-MODEL RESULTS

Yan Qu (2006) developed a computer simulation using the Monte Carlo method (MCM) in order to calculate the effect of thermal environment on LPRT output. In his Monte Carlo light-pipe model, the radiation source will be not only from the tip caused by the blackbody but also from the sidewall imperfections that trap the tube furnace radiation. He defined the radiative energy from the light-pipe tip collected by the photo-detector to be the reference and allowed energy received from the sidewall to increase temperature readings. The light-pipe temperature reading is found by using the following equation:

$$T_{light-pipe} = \frac{1}{0.9 \mu m} \cdot \frac{14,387.752}{\ln \left[ A_{tip} \left( \frac{2\pi \times 0.59552137 \times 10^8}{(n_{sidewall-received} e_{sidewall} + n_{tip-received} e_{tip}) (0.9 \mu m)^5} \right) + 1 \right]} \quad (3.9)$$

where

- $A_{tip}$  = the surface area of the light-pipe tip
- $e_{sidewall}$ ,  $e_{tip}$  = the energy carried by each bundles and generated by light-pipe sidewall and light-pipe tip, respectively
- $n_{sidewall-received}$  = the number of bundles received by the detector through the light-pipe tip
- $n_{tip-received}$  = the number of bundles received by the detector through the light-pipe sidewall

From equation (3.9), Yan Qu also assumed that the sensitive wavelength of the detector is  $0.9 \mu m$  instead of  $0.955498 \mu m$ , which is its actual effective wavelength. Figure 3.19 shows the flow chart of his Monte Carlo code. The comparison of light-pipe temperature obtained from experiments and computer simulations at different surface roughness was plotted as a function of furnace temperature in Figure 3.20. The solid lines represent the experimental results while the dotted lines represent the computer simulation results. Yan Qu claimed that in order to match the computer simulation results to the results obtained from the experiment, the diffuse reflectivity should be varied. Table 3.5 shows the value of non-specular reflectivity gained from matching the Monte Carlo analysis with the experimental results.

It can be seen from Table 3.5 that the diffuse reflectivity set by Yan Qu for highly polished fused silica light-pipe is 0.002% while 3% and 1% are the diffuse parts of the reflectivity for the fused silica light-pipe roughened by 800 and 120 grit sandpapers, respectively. As also mentioned earlier, the total reflectivity will be dominated by the diffuse component if the light-pipe surface is roughened. However, the value of diffuse reflectivity of a rough surface ( $\rho_{diffuse} \approx \rho_{total}$ ) shown in Table 3.5 decreases as the roughness increases. This can be explained by measuring reflectance and transmittance of fused silica sample at three different surface roughnesses: highly polished, roughening by 800 grit sandpaper, and roughening by 120 grit sandpaper. Again, the light-pipe sample has the dimension of 25 mm diameter and 10 mm thickness.

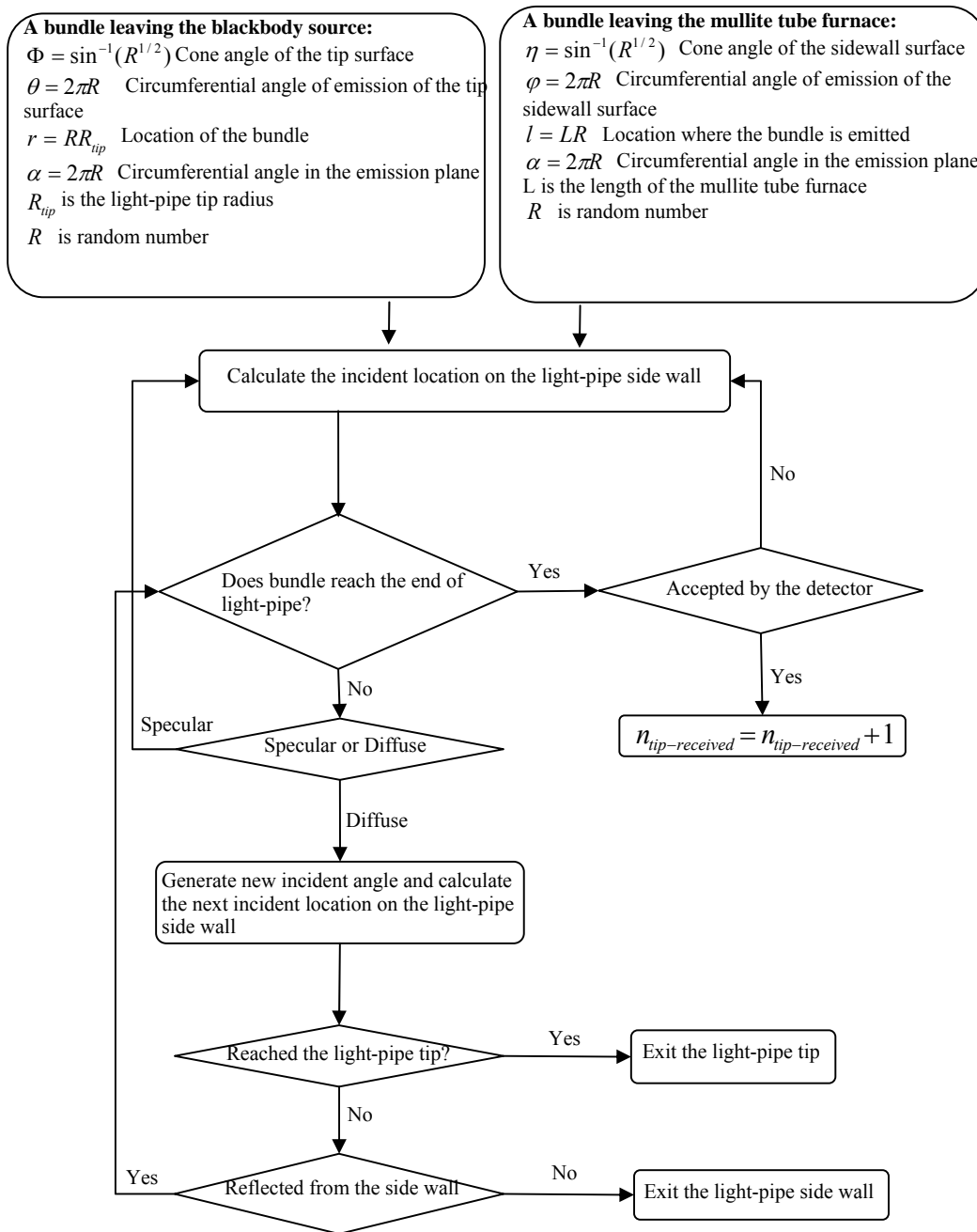


Figure 3.19: Flow chart diagram of Yan Qu's Monte Carlo model for determining the thermal environment effect [Qu, 2006].

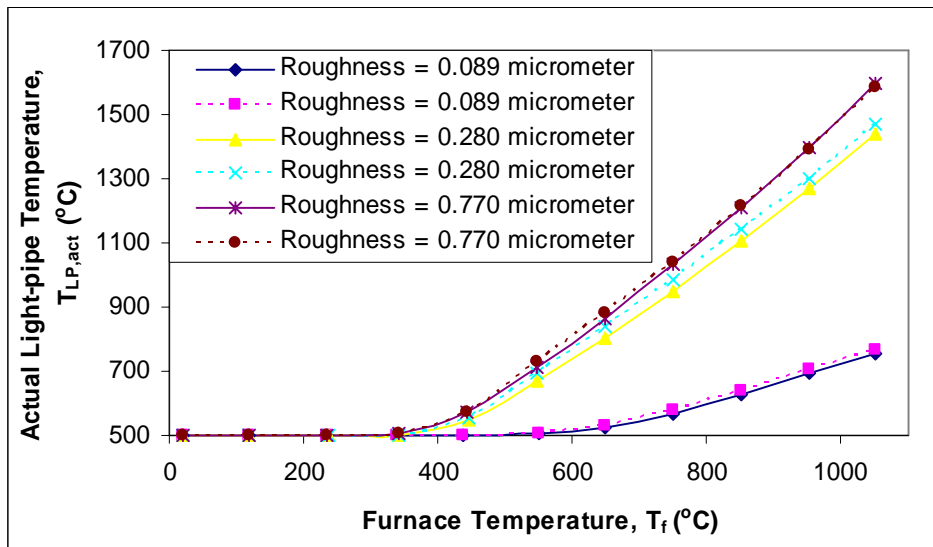


Figure 3.20: Comparison of experiment and computer simulation light-pipe temperature results.

	Highly polished fused silica	Fused silica rubbed by 800 grit sandpaper	Fused silica rubbed by 120 grit sandpaper
Roughness (micrometers)	0.089	0.280	0.770
Diffuse reflectivity	0.002%	3%	1%

Table 3.5: Surface roughness measurements in micron and diffuse reflectance gained from matching Yan Qu’s computer code with experimental results.

Since the fused silica is semitransparent at low wavelength as seen in Figure 3.12, it is impossible to evaluate the true reflectivity of the light-pipe surface. The spectral reflectivity of the light-pipe sample measured by using the infrared spectroradiometer is the combination of energy reflecting from the measured surface and that transmitted through the surface being measured which is caused by the multiple reflections inside the

sample, as seen in Figure 3.21a. To achieve the actual spectral reflectivity of the light-pipe surface, a black optical gel made of Aliphatic Hydrocarbons & Gelling Agents and having similar refractive index as fused silica material was applied to all light-pipe surfaces except the top surface which was intended to measure. The manufacturer claimed that the refractive index as a function of wavelength expressed in angstroms at 25 °C for this optical gel equates to:

$$n_{gel} = 1.44514 + \frac{431760}{\lambda^2} - \frac{1.80659 \times 10^{11}}{\lambda^4} \quad (3.10)$$

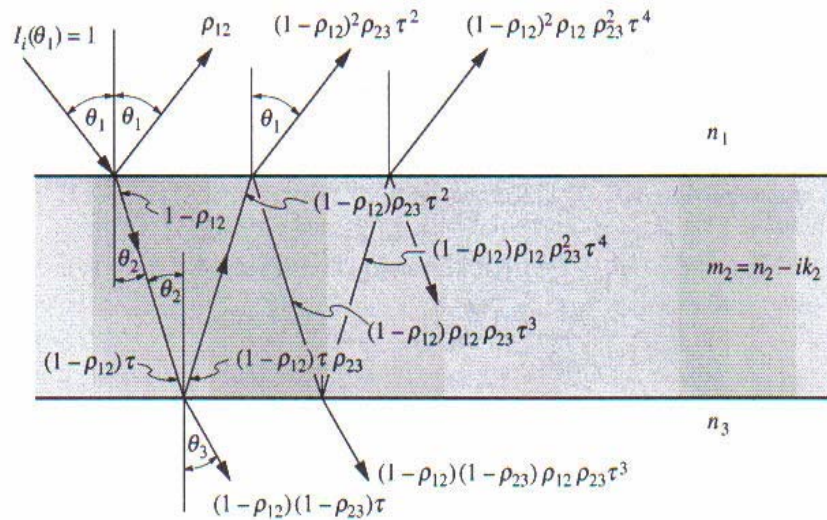
Malitson (1965) determined the relationship between the index of refraction of optical quality fused silica and the wavelength from 0.21 to 3.71 microns at 20 °C and gave as the following equation:

$$n_{fused-silica}^2 = 1 + \frac{0.6961663\lambda^2}{\lambda^2 - (0.0684043)^2} + \frac{0.4079426\lambda^2}{\lambda^2 - (0.1162414)^2} + \frac{0.8974794\lambda^2}{\lambda^2 - (9.896161)^2} \quad (3.11)$$

Considering equations (3.10) and (3.11) at the sensitive wavelength of our detector ( $\lambda_{eff} = 0.955498 \mu m$ ), the refractive indices of the optical gel and fused silica are equal to 1.44559 and 1.45099, respectively. Even though the optical gel was used, some energy could reflect back to the light-pipe sample at the interface between the outer surface of optical gel and air because of slightly different refractive index values. This reflected energy will cause an error in reflectivity measurement. To eliminate this problem, the light-pipe sample covered with the optical gel was inserted inside the light trap painted with flat black paint as shown in Figure 3.21b. Most of the signal, passing through the light-pipe sample and the optical gel, is absorbed by the light-trap. Figures

3.22 and 3.23 illustrated the results of reflectance and transmittance of fused silica light-pipe at wavelength from 0.87 to 1.07 microns.

a)



b)

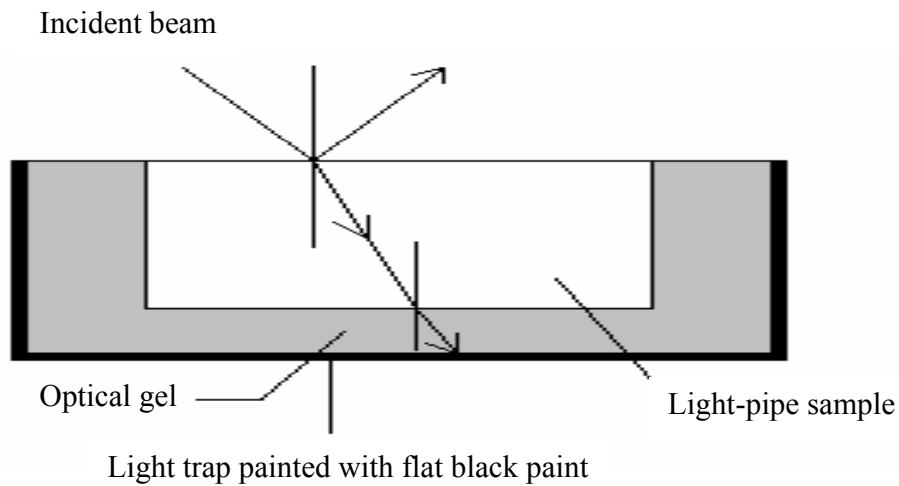


Figure 3.21: a) Reflectivity and transmittivity for radiation incident on a thick semitransparent material [Modest, 2003], and b) Experimental set-up for determining the actual reflectivity.

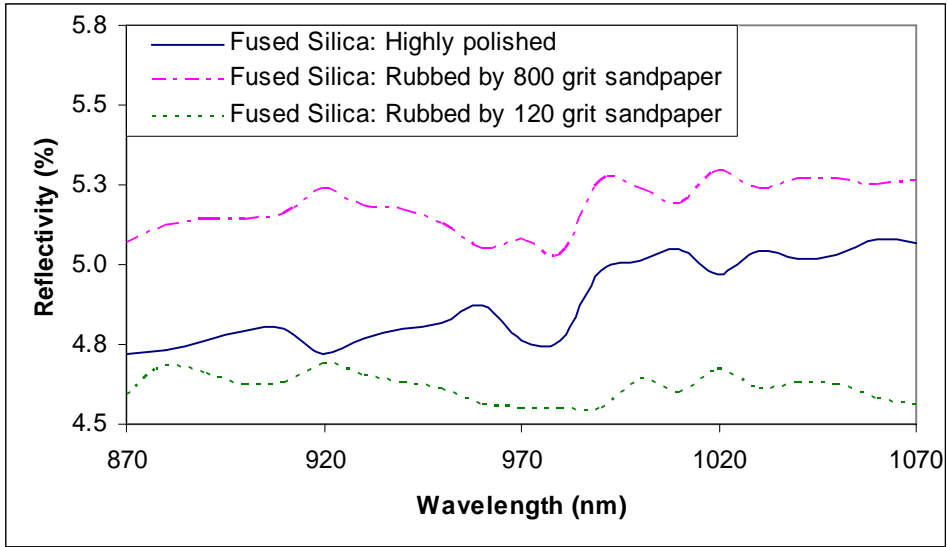


Figure 3.22: Spectral directional-hemispherical reflectivity (%) of fused silica light-pipe at different surface roughness.

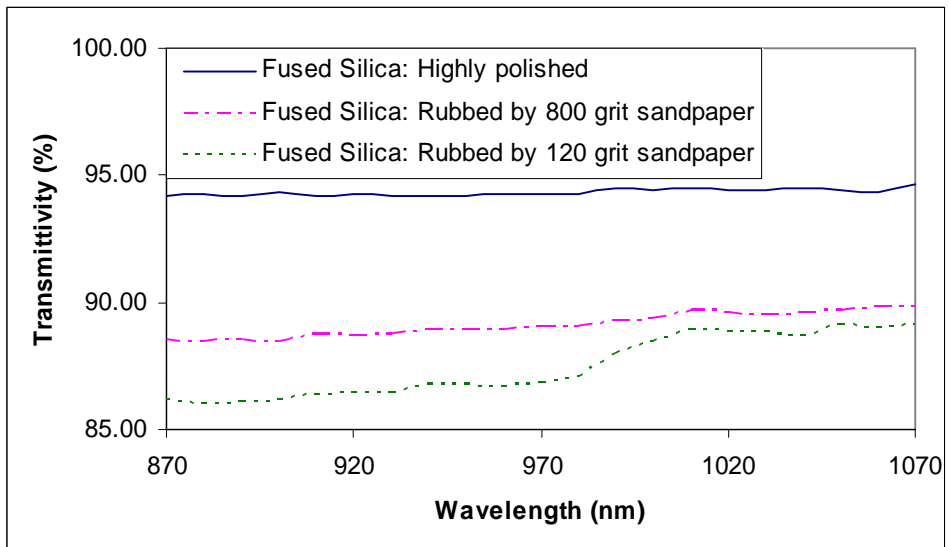


Figure 3.23: Spectral transmittivity (%) of fused silica light-pipe at different surface roughness.

Based on Figures 3.22 and 3.23 comparing with Yan Qu's MCM analysis results, it can be concluded that the specular reflectivity is dominant for a highly polished light-pipe and even the small amount of diffuse reflectivity (0.002%) can cause a significant error in the LPRT temperature readings when the surrounding temperature is higher than the target temperature. Once the surface roughness on a light-pipe increases to 0.280 microns, the total reflectivity (all of which is diffuse reflectivity) increases with decreasing transmittivity. However, after roughening with 120 grit sandpaper which creates 0.770 microns of surface roughness, the total reflectivity and transmittivity decrease. This is caused by the multiple bounces between each side of the roughness height which increase the chance of radiation signal to be absorbed. This means that the absorptivity value will increase as the light-pipe surface is roughened. Furthermore, both experiment and computer simulation reveal that the external radiation can lead to an extreme error on LPRT temperature measurement if the side of the light-pipe has surface imperfections and the environment temperature is above the target temperature by more than about 160 °C.

## **Chapter 4: *Discussion on Separation Distance Effect***

### **4.1 INTRODUCTION**

As addressed in the introduction section of Chapter 3, for standard commercial applications a small portion of the light-pipe is exposed to the hot environment inside an RTP chamber. Because most of the surface area of an LPRT is in the cold surrounding, the temperature of the light-pipe tip is cold compared to the object's surface being measured. This lower temperature of LPRT's tip acts as a radiation heat sink for the measured object. The magnitude of this depression in the wafer temperature depends on the distance between the light-pipe tip and the silicon wafer. This is called the "separation distance" or "drawdown" effect. The shorter the distance is, the more heat loss caused by the separation distance effect is expected to be present. The resulting non-uniform temperature distribution can cause significant failures of the components deposited on wafers.

Kreider and his colleagues (2003) at the National Institute of Standards and Technology (NIST) quantified the LPRT proximity effect using a 2-mm diameter sapphire light-pipe surrounded by 4.2-mm diameter sapphire sheath. The experiment was performed in the NIST RTP test bed, as shown in Figure 4.1. The temperature depression of 25 °C in the wafer temperature of 825 °C was measured by this group of researchers when the space between the light-pipe tip and the wafer was 2 mm. They also claimed that a depression of over 30 °C could occur at temperatures near 1,000 °C.

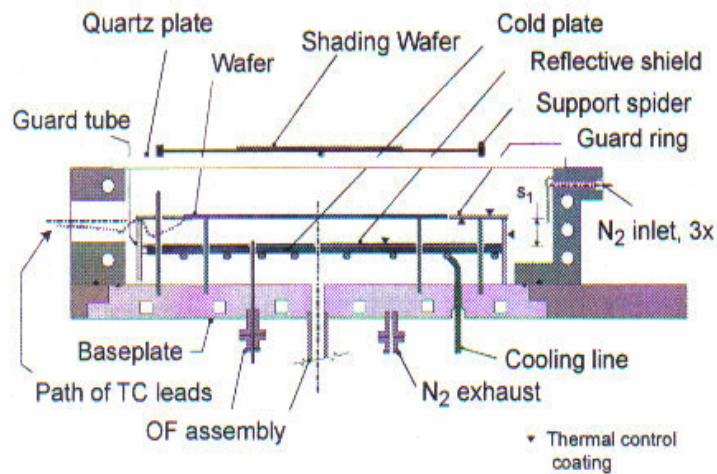


Figure 4.1: Illustration of NIST RTP test bed [Kreider, Chen, Dewitt, Kimes, and Tsai, 2003].

However, Qu, Puttitwong, Howell, Ezekoye, and Ball (2005) ran a similar experiment by using the thermometry test bed developed at the University of Texas at Austin, as illustrated in Figure 4.2. The investigation of draw-down effect was conducted with a 4-mm diameter and 428.5-mm length commercial fused silica light-pipe probe. Our experimental results for wafer temperatures of 535 °C, 760 °C, and 855 °C showed that the temperature readings at the wafer’s center point did not drop as the distance between the light-pipe tip and the target wafer decreased. Therefore, no evidence of the draw-down effect occurred in this study.

To further investigate the reason why the thermal depressions occurred only in the NIST research, another experimental study was performed by using three different kinds of light-pipes with a new chamber. The experimental results were also compared with the results obtained from a finite-difference computer simulation. The acceptance angle of the light-pipes was also determined in order to understand the temperature reading displayed by LPRTs.

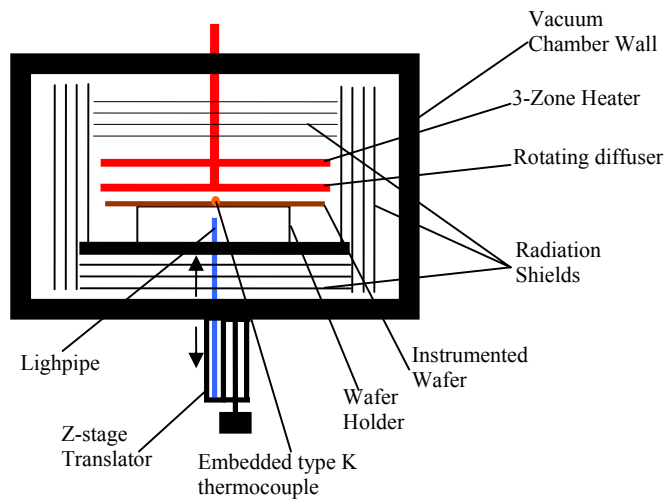


Figure 4.2: Schematic of UT-Austin RTP test bed [Qu, Puttitwong, Howell, Ezekoye, and Ball, 2005].

#### 4.2 EXPERIMENTAL SET-UP AND RESULTS

The test bed used to evaluate the separation distance effect is shown in Figure 4.3. The stainless steel plates were applied to create the 41-mm thickness chamber walls. To obtain a uniform temperature distribution, K-wool insulation was inserted inside the walls. Inside the chamber, a square heater was installed 13 mm above the measured object. Because of its high reflectivity and temperature capability, a molybdenum sheet located 26 mm under the instrumented object to achieve more uniform heating profile across the object's surface. The molybdenum sheet and test object were separated by a quartz ring (114 mm in diameter), which has low conductivity. Cold water at 5 °C was ducted under the radiation shield to prevent oxidation. Three kinds of 4-mm diameter commercial light-pipes measured the temperature at the bottom side of the object. The light-pipes were adjusted in height by using the linear translation stage.

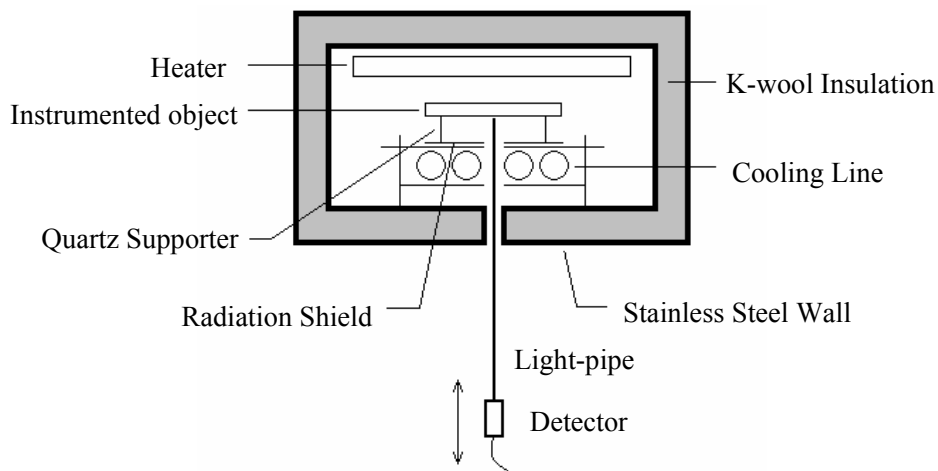


Figure 4.3: Schematic of chamber and several internal components.

As addressed in Chapter 1, the emissivity of the silicon wafer is unknown and the silicon wafer is semitransparent at low temperature. Thus, an octagon-shaped molybdenum plate with 152.4 mm diameter and 0.5 mm in thickness was used instead of the silicon wafer because of their similar conductivity values. Table 4.1 shows the values of thermal conductivity of different materials, used in this research, at room temperature. Since it was hard to control the temperature inside the chamber, a purge atmosphere of  $N_2$  was not used. To eliminate oxidation from occurring on the molybdenum plate and to obtain a high emissivity value, multiple layers of flat black ultra-high-temperature paint were applied to both sides of the surface. Five type-K thermocouples; four at the corner of a 56.7 mm square and one at the center of the square, were embedded on the test plate to monitor the temperature distribution.

Materials	Conductivity (W/m K)
Fused Silica	1.38
Fused Quartz	1.30
Sapphire	42.00
Molybdenum	138.00
Ceramic	25.08
Silicon	149.00

Table 4.1: Overview of thermal conductivity for each material.

Again, before starting the experiment, the LPRTs were calibrated against the blackbody source at 400 °C, 475 °C, and 550 °C, respectively. The temperature readings displayed by the thermocouples were collected when the light-pipes' tips were moved vertically away from the molybdenum plate by 2mm, 4mm, 6mm, 8mm, 16mm, 25mm, and 32 mm. Figures 4.4 to 4.12 illustrate the temperature readings versus the separation distances at the setting chamber temperatures of 400 °C, 475 °C, and 550 °C for fused silica, fused quartz, and sapphire light-pipes including the expanded uncertainty value at 95.45% level of confidence (a coverage factor of  $k = 2.00$ ) for the center thermocouple (TC#1). Only two thermocouple readings along with the indicated temperature of the center thermocouple are plotted in these figures.

The uncertainty analysis in the following figures was based on the details in Chapter 2. An example of the uncertainty calculation for the case of a sapphire light-pipe with ceramic plate at a chamber temperature of 475 °C and at the 2-mm separation distance was given in Table 4.2.

Type	Source of uncertainty	Probability Distribution	A	B (°C)	C (°C)
A	TC reading repeatability	Normal	1	0.0	0.0
B	Accuracy of type K thermocouple	Rectangular	$\sqrt{3}$	3.6	2.1
B	Resolution of TC reading	Rectangular	$\sqrt{3}$	0.1	0.0
B	Accuracy of multimeter	Rectangular	$\sqrt{3}$	0.0	0.0
B	Accuracy of cold junction reading	Rectangular	$\sqrt{3}$	1.0	0.6
B	Accuracy of cold junction TC	Rectangular	$\sqrt{3}$	2.5	1.4
B	Resolution of cold junction reading	Rectangular	$\sqrt{3}$	0.1	0.0
B	Hysteresis	Rectangular	$\sqrt{3}$	0.4	0.2
B	Accuracy of chamber controller	Rectangular	$\sqrt{3}$	2.1	1.2
B	Uniformity of chamber	Rectangular	$\sqrt{3}$	0.3	0.2
B	Stability of chamber	Rectangular	$\sqrt{3}$	0.3	0.2
B	Resolution of separation distance	Rectangular	$\sqrt{3}$	0.1	0.1
-	Combined standard uncertainty	Normal	-	-	2.9
-	Expanded standard uncertainty	Normal (k=2)	-	-	5.7

Table 4.2: Example of uncertainty budget of sapphire light-pipe with ceramic plate at 475 °C and 2-mm spacing. A, B, and C are divisor, uncertainty value, and standard uncertainty.

Because the chamber used in this study was constructed by the author, no specification of chamber's uniformity and instability were available. Before analyzing these two values, several type K thermocouples were bound together and inserted into the chamber. The chamber temperature was set to 400 °C, 475 °C, and 550 °C, respectively. Since the temperature readings indicated by these thermocouples must be exactly the same because they had the same target position, the differences between the

thermocouple readings were used to determine their corrections. After obtaining the correction values, all thermocouples were placed at different positions covering all area inside the chamber including at the geometric center. The thermocouple temperatures were measured at similar chamber temperature of 400 °C, 475 °C, and 550 °C. Half of the difference between the maximum and minimum temperatures was used for evaluating the uniformity of the chamber. The temperature displayed by the thermocouple located at the geometric center was continuously collected over a one hour period of time. Then, the chamber's stability was calculated by using the difference of the maximum and minimum temperature readings divided by two.

From Figures 4.4 – 4.12, consideration of the temperatures of the central thermocouple comparing to of the thermocouples #2 and #3 at each separation distance and at each chamber temperature shows that only the sapphire light-pipe caused a thermal depression at the center point of the molybdenum plate. The experimental results for fused silica and fused quartz light-pipes do not show any significant separation distance effect. With the sapphire light-pipe, the maximum depression increases with increasing temperature of the molybdenum sheet. A 1.6 °C, a 2.1 °C, and a 2.5 °C drops are found for the object near 400 °C, 475 °C, and 550 °C, respectively. Because sapphire has a higher thermal conductivity than fused silica and fused quartz materials, as shown in Table 4.1, the tip temperature of the sapphire light-pipe is much lower than for the other light-pipes, and this can increase the separation distance effect.

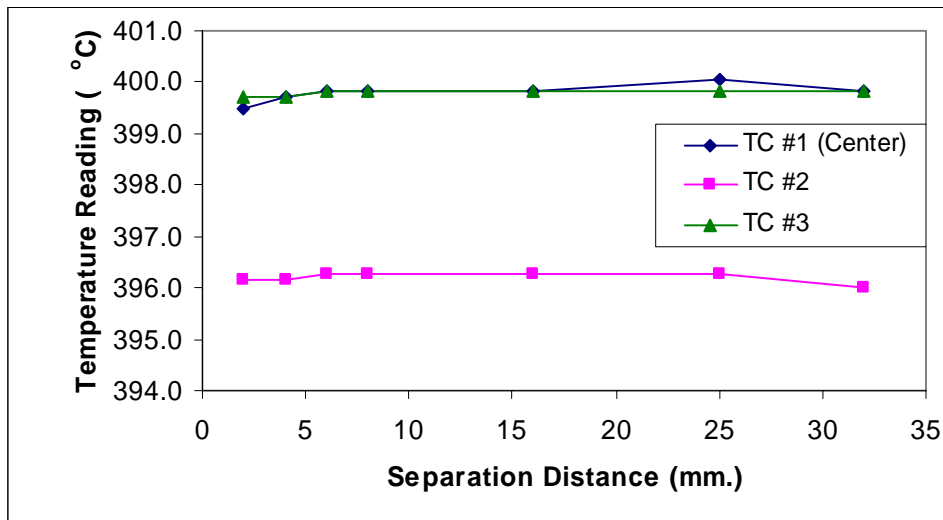


Figure 4.4: The changes in temperature of TCs embedded on molybdenum sheet due to the different positions of the fused silica light-pipe for the chamber temperature of 400 °C. The uncertainty of TC#1 is  $\pm 5.3$  °C.

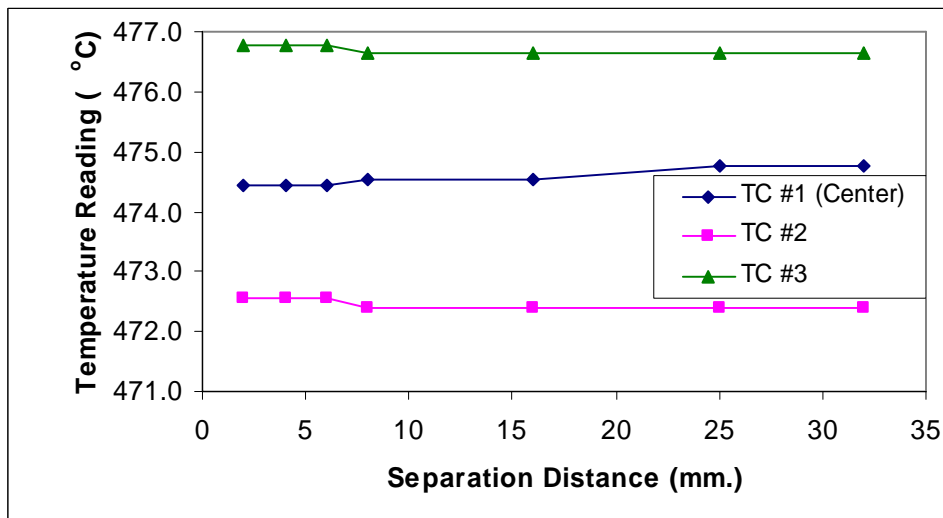


Figure 4.5: The changes in temperature of TCs embedded on molybdenum sheet due to the different positions of the fused silica light-pipe for the chamber temperature of 475 °C. The uncertainty of TC#1 is  $\pm 5.7$  °C.

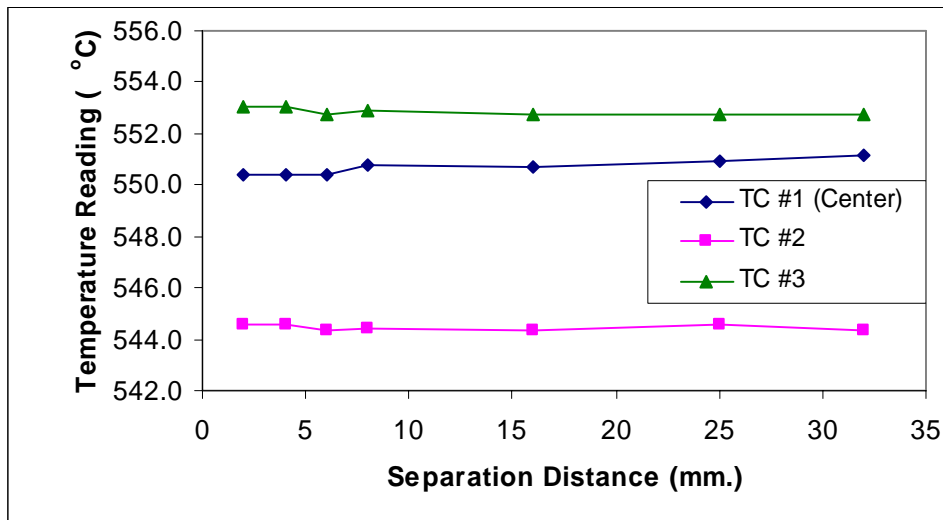


Figure 4.6: The changes in temperature of TCs embedded on molybdenum sheet due to the different positions of the fused silica light-pipe for the chamber temperature of 550 °C. The uncertainty of TC#1 is  $\pm 6.2$  °C.

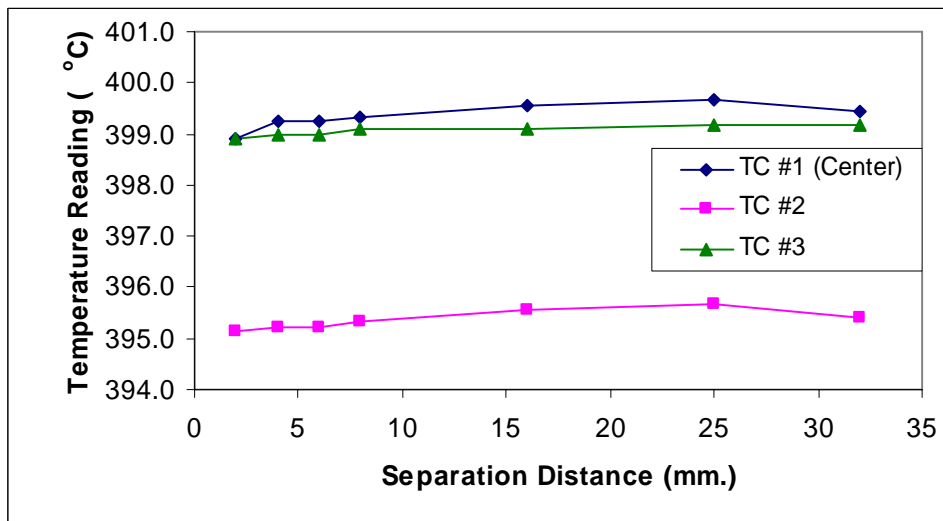


Figure 4.7: The changes in temperature of TCs embedded on molybdenum sheet due to the different positions of the fused quartz light-pipe for the chamber temperature of 400 °C. The uncertainty of TC#1 is  $\pm 5.3$  °C.

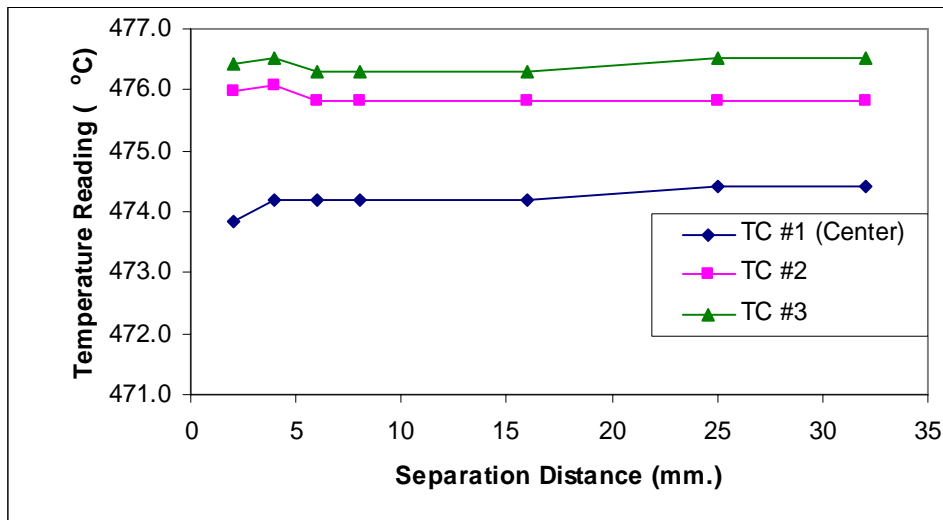


Figure 4.8: The changes in temperature of TCs embedded on molybdenum sheet due to the different positions of the fused quartz light-pipe for the chamber temperature of 475 °C. The uncertainty of TC#1 is  $\pm 5.7$  °C.

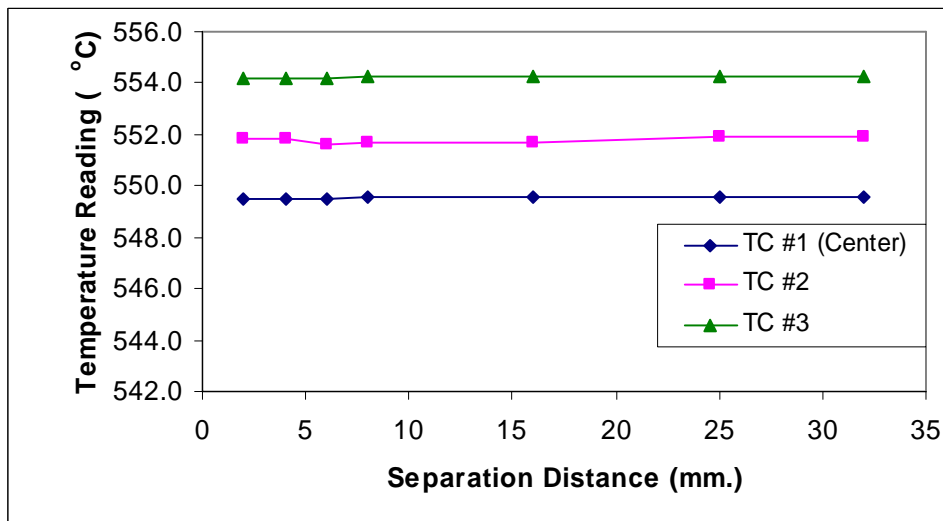


Figure 4.9: The changes in temperature of TCs embedded on molybdenum sheet due to the different positions of the fused quartz light-pipe for the chamber temperature of 550 °C. The uncertainty of TC#1 is  $\pm 6.2$  °C.

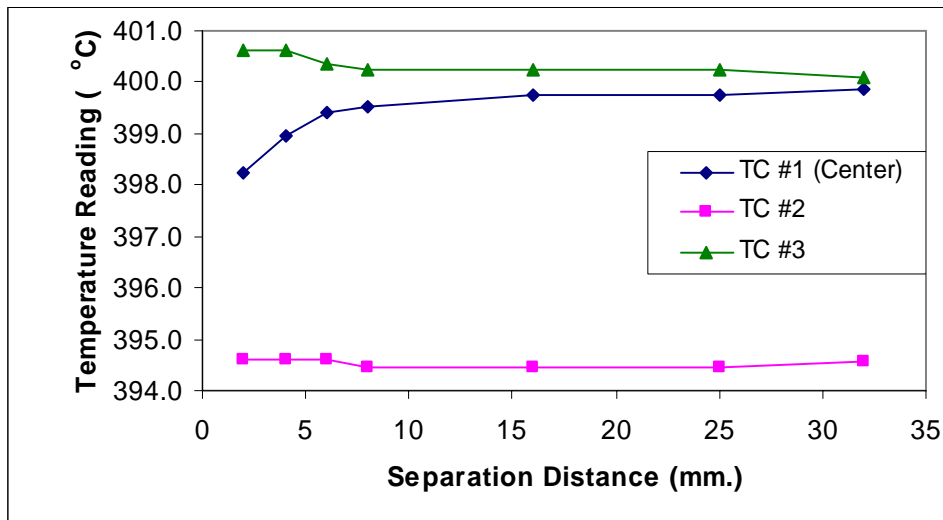


Figure 4.10: The changes in temperature of TCs embedded on molybdenum sheet due to the different positions of the sapphire light-pipe for the chamber temperature of 400 °C. The uncertainty of TC#1 is  $\pm 5.3$  °C.

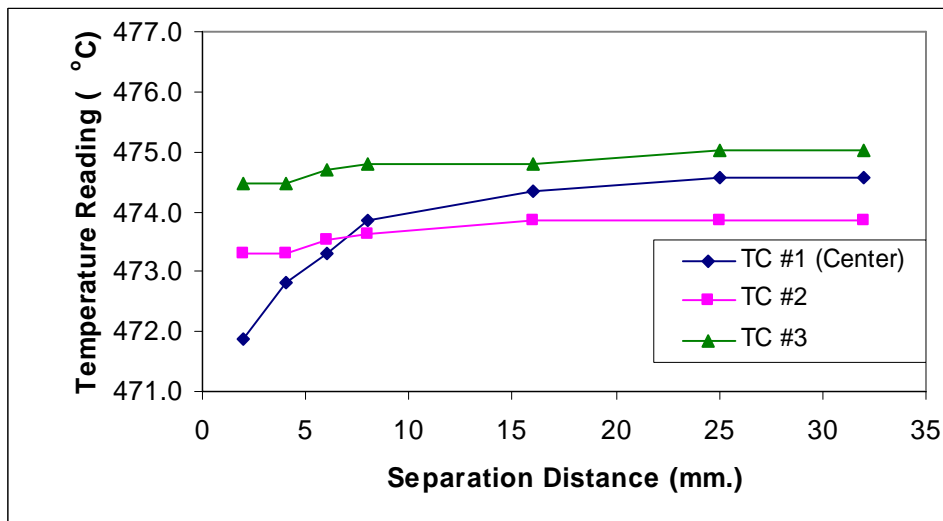


Figure 4.11: The changes in temperature of TCs embedded on molybdenum sheet due to the different positions of the sapphire light-pipe for the chamber temperature of 475 °C. The uncertainty of TC#1 is  $\pm 5.7$  °C.

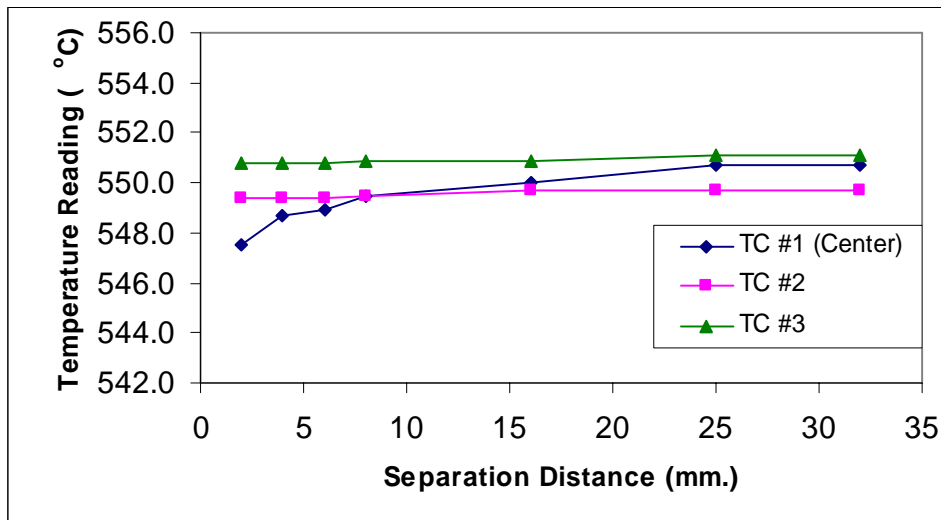


Figure 4.12: The changes in temperature of TCs embedded on molybdenum sheet due to the different positions of the sapphire light-pipe for the chamber temperature of 550 °C. The uncertainty of TC#1 is  $\pm 6.2$  °C.

A similar experiment was repeated by using an instrumented ceramic plate painted with flat black ultra-high-temperature paint instead of the painted molybdenum plate because of the low value of thermal conductivity for the ceramic. The ceramic has a dimension of 152.4 mm in diameter and 5 mm in thickness. The experimental results at 475 °C of chamber temperature for fused silica, fused quartz, and sapphire light-pipes were illustrated in Figures 4.13 - 4.15, respectively.

Based on these three figures, the drops in the ceramic center temperature were 0.4 °C, 0.3 °C, and 4.5 °C for fused silica, fused quartz, and sapphire light-pipes when the distances of the light-pipe tip from the object's surface decreased from 32 mm to 2 mm. Even when the fused silica and fused quartz light-pipes are used, which have higher tip temperature, at the same chamber temperature and the same light-pipe, it can be seen that the temperature drops in the ceramic plate are higher than in the molybdenum plate. The

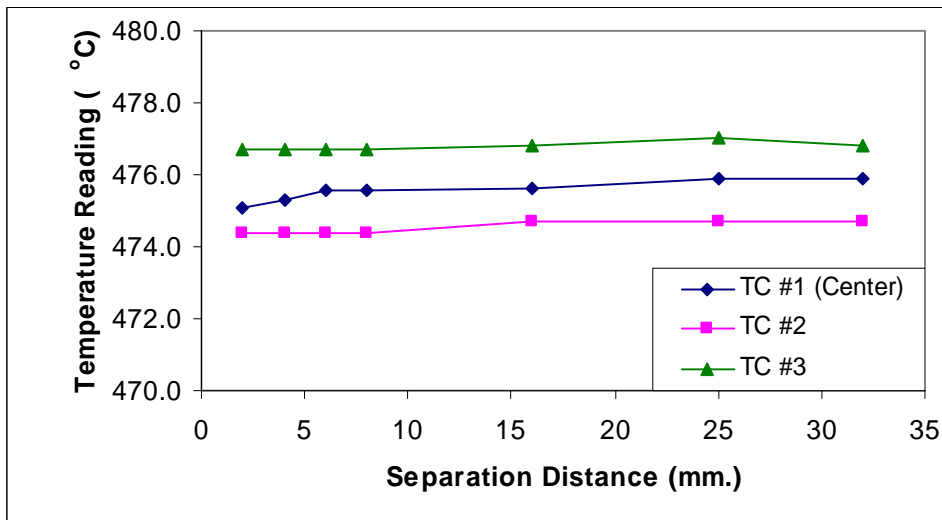


Figure 4.13: The changes in temperature of TCs embedded on ceramic plate due to the different positions of the fused silica light-pipe for the chamber temperature of 475 °C. The uncertainty of TC#1 is  $\pm 5.7$  °C.

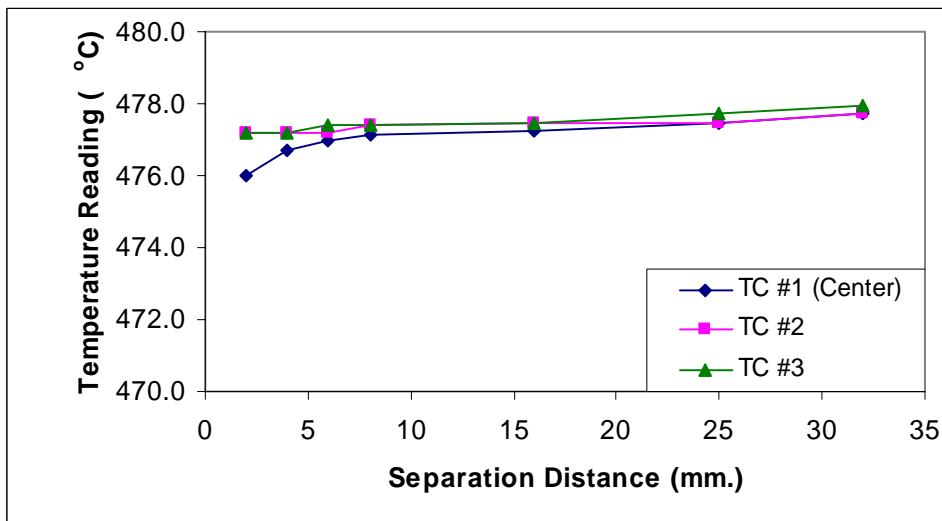


Figure 4.14: The changes in temperature of TCs embedded on ceramic plate due to the different positions of the fused quartz light-pipe for the chamber temperature of 475 °C. The uncertainty of TC#1 is  $\pm 5.7$  °C.

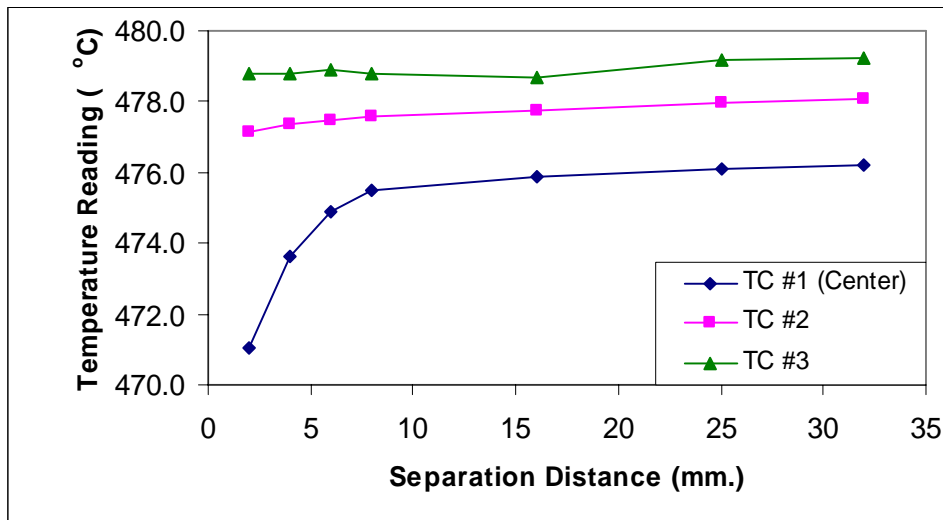


Figure 4.15: The changes in temperature of TCs embedded on ceramic plate due to the different positions of the sapphire light-pipe for the chamber temperature of 475 °C. The uncertainty of TC#1 is  $\pm 5.7$  °C.

reason is because the higher thermal conductivity of molybdenum smears out a radial temperature gradient caused by the separation distance effect.

### 4.3 COMPUTER SIMULATION RESULTS

In this section, a computer simulation used to investigate the separation distance effect is described. Figure 4.16 shows the schematic details of the chamber for computer modeling. Diffuse-gray surfaces for the radiation shield, painted objects, and light-pipes were assumed in this model. Furthermore, the experimental study was not conducted in a vacuum environment, and the governing equations for the radiation heat transfer combined with conduction and convection can be specified as follow:

For the measured object's surface:

$$\begin{aligned} \frac{1}{\varepsilon_{obj}(T)} \left[ q + \frac{A_{CS,obj}}{A_{S,obj}} k_{obj} \frac{1}{R} \frac{d}{dR} \left( R \frac{dT_{obj}}{dR} \right) - 2h_{obj} (T_{obj} - T_{surr}) \right] &= \sigma T_{obj}^4 - \int \sigma T_{surr}^4 dF_{obj-surr} \\ - \int \sigma T_{shield}^4 dF_{obj-shield} - \int \left[ \sigma T_{lp}^4 - \left( \frac{1 - \varepsilon_{lp}(T)}{\varepsilon_{lp}(T)} \right) \left\{ \frac{A_{CS,lp}}{A_{S,lp}} k_{lp} \frac{d^2 T_{lp}}{dz^2} - h_{lp} (T_{lp} - T_{surr}) \right\} \right] &dF_{obj-lp} \end{aligned} \quad (4.1)$$

For the light-pipe's surface:

$$\begin{aligned} \frac{1}{\varepsilon_{lp}(T)} \left[ \frac{A_{CS,lp}}{A_{S,lp}} k_{lp} \frac{d^2 T_{lp}}{dz^2} - h_{lp} (T_{lp} - T_{surr}) \right] &= \sigma T_{lp}^4 - \int \sigma T_{surr}^4 dF_{lp-surr} - \int \sigma T_{shield}^4 dF_{lp-shield} \\ - \int \left[ \sigma T_{obj}^4 - \left( \frac{1 - \varepsilon_{obj}(T)}{\varepsilon_{obj}(T)} \right) \left\{ q + \frac{A_{CS,obj}}{A_{S,obj}} k_{obj} \frac{1}{R} \frac{d}{dR} \left( R \frac{dT_{obj}}{dR} \right) - 2h_{obj} (T_{obj} - T_{surr}) \right\} \right] &dF_{lp-obj} \end{aligned} \quad (4.2)$$

where

- $q$  = Heat flux (W/m<sup>2</sup>).
- $A_{CS}$  = Cross-sectional area, m<sup>2</sup>.
- $A_S$  = Surface area, m<sup>2</sup>.
- $\varepsilon(T)$  = Total hemispherical emissivity.
- $k$  = Thermal conductivity, W/m K.
- $h$  = Convective heat transfer coefficient, W/m<sup>2</sup> K.
- $F$  = Configuration factor.

Subscripts:

- obj = Object.
- lp = Light-pipe.

surr = Surroundings.

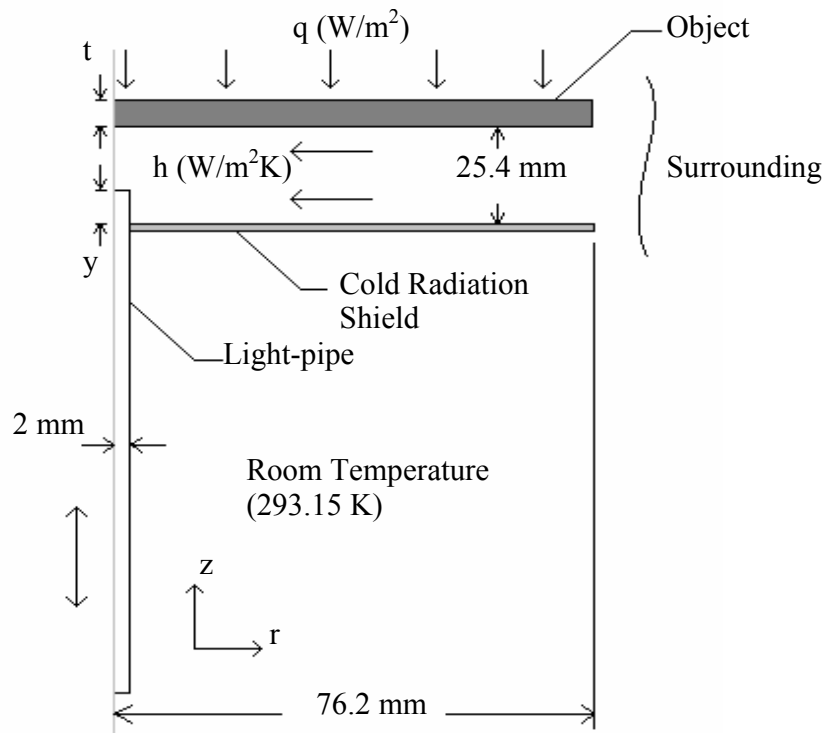


Figure 4.16: Schematic details of computer model.

The total hemispherical emissivity is a function of the spectral hemispherical emissivity,  $\varepsilon(\lambda)$ , and the blackbody function. Because of the opaque properties of materials used in this study (no radiation can pass through the surface) and Kirchhoff's law showing the equivalence between the absorbed and emitted energy, the spectral hemispherical emissivity equates to one minus the spectral hemispherical reflectivity. Measurements of the spectral hemispherical reflectivity of each material and surface coating were performed by using the infrared spectroradiometer described in Chapter 3. Representative values of this reflectivity are plotted in Figures 4.17 and 4.18. Figure 4.19 shows a plot of blackbody fractions in the spectral band from 0 to 14,000 nm as function

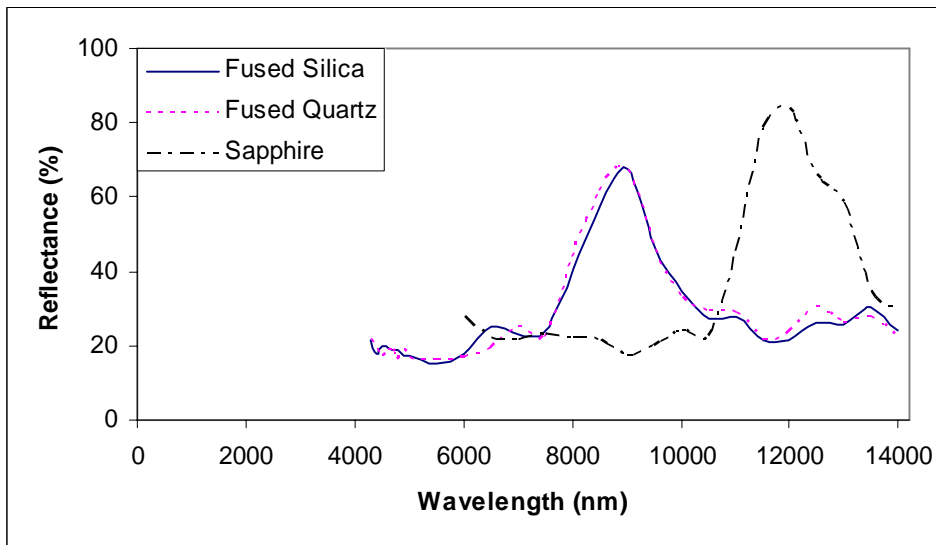


Figure 4.17: Spectral directional-hemispherical reflectivity (%) of fused silica, fused quartz, and sapphire light-pipes.

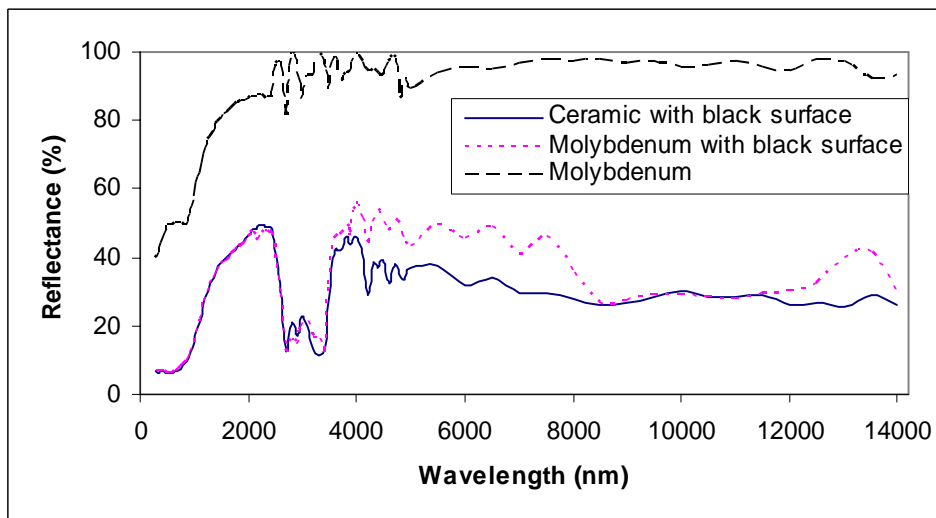


Figure 4.18: Spectral directional-hemispherical reflectivity (%) of materials with and without coatings.

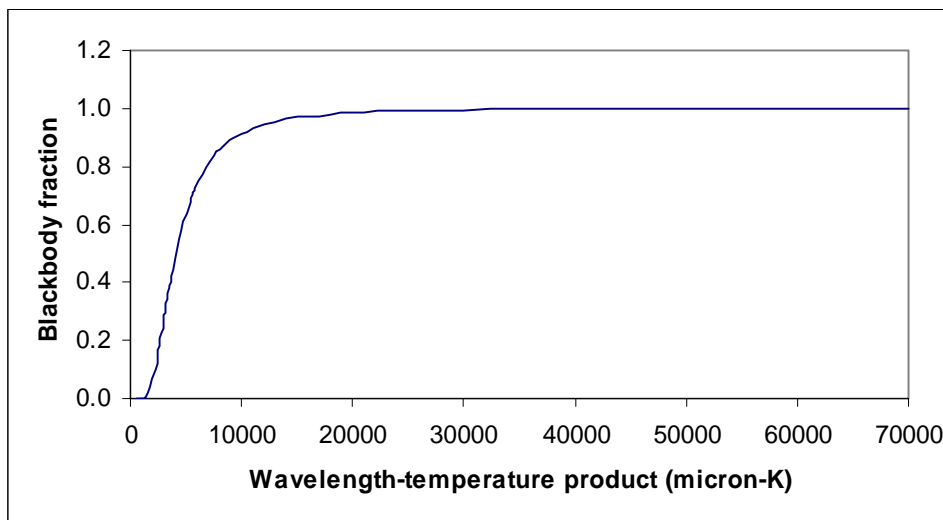


Figure 4.19: Fractional blackbody emissive power in the range 0 to  $\lambda T$  [Siegel and Howell, 2002].

of  $\lambda T$ . Because at low wavelength, the radiation from all directions can pass through the light-pipe probe as seen in Figure 3.12, the total radiation signal coming from the light-pipe surface to the detector is the combination of the reflectance and transmittance of the pipe surface. Thus, the spectral hemispherical emissivity of each light-pipe surface at this range of wavelength was modeled as a blackbody ( $\varepsilon = 1$ ).

The configuration factors between each surface were determined by using the formulas available in the on-line radiation shape factors web catalog (<http://www.me.utexas.edu/~howell/>) along with configuration-factor algebra [Siegel and Howell, 2002]. The configuration factors for the painted object's surface to the top surface of the light-pipe tip and to the radiation shield are approximated as parallel circular disks of unequal radius with centers along the same normal, shown in Figure 4.20. For the object to the sidewall of the light-pipe probe and to the surroundings, the shape factors are calculated by using the formulas in the case of the outer surface of a cylinder to an annular disk at the end of the cylinder, shown in Figure 4.21.

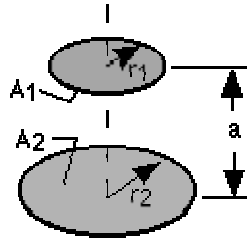


Figure 4.20: Illustration of disk to parallel coaxial disk of unequal radius [Siegel and Howell, 2002].

$$F_{1-2} = \frac{1}{2} \left\{ X - \left[ X^2 - 4 \left( \frac{R_2}{R_1} \right)^2 \right]^{\frac{1}{2}} \right\} \quad (4.3)$$

where  $R = r/a$ ; and  $X = 1 + (1 + R_2^2)/R_1^2$ .

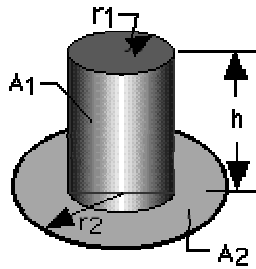


Figure 4.21: Illustration of outer surface of cylinder to annular disk at end of cylinder [Siegel and Howell, 2002].

$$F_{1-2} = \frac{B}{8RH} + \frac{1}{2\pi} \left\{ \cos^{-1} \left( \frac{A}{B} \right) - \frac{1}{2H} \left[ \frac{(A+2)^2}{R^2} - 4 \right]^{\frac{1}{2}} \times \cos^{-1} \left( \frac{AR}{B} \right) - \frac{A}{2RH} \sin^{-1} R \right\} \quad (4.4)$$

where  $R = r_1/r_2$ ;  $H = h/r_2$ ;  $A = H^2 + R^2 - 1$ ; and  $B = H^2 - R^2 + 1$ .

The surrounding temperature and the temperature of the cold radiation shield were assumed to be uniform in this computer modeling. Their values were averaged from the temperature readings indicated by several type K thermocouples which were placed at different positions inside the chamber. Table 4.3 shows the results with the uncertainty values ( $k = 2.00$ ) at each chamber temperature. The uncertainty budgets of both temperatures are similar to Table 4.2 except that the error source from resolution of separation distance does not exist. Furthermore, there is an additional source of uncertainty of the surrounding temperature which is the vertical uniformity of the chamber. The uniformity of the chamber appearing in the uncertainty budget of separation distance effect and shield temperature is the horizontal uniformity.

Chamber Temperature (°C)	Surrounding Temperature (°C)	Shield Temperature (°C)
400.0	$314.2 \pm 7.5$	$197.4 \pm 7.2$
475.0	$380.0 \pm 7.5$	$265.8 \pm 6.8$
550.0	$449.3 \pm 7.9$	$341.0 \pm 6.7$

Table 4.3: Temperatures of surrounding and cold radiation shield at different chamber temperatures.

Because there is no forced fluid motion over the object and light-pipe's surfaces, the convective heat transfer coefficients were determined by free natural convection. The natural convection heat transfer depends on not only the type of fluid involved and the variation of surface temperature but also the geometry of the surface [Cengel, 1998]. In this computer model, therefore, the painted object was treated as a horizontal plate which has the cold surface facing up. With this natural flow geometry, the convective heat transfer coefficient is of the form:

$$h_{obj} = 0.27 \frac{k}{L} Ra_L^{1/4} \quad ; \quad 10^5 \leq Ra_L \leq 10^{11} \quad (4.5)$$

where

$$Ra_L = \text{Rayleigh number} = \frac{g\beta(T_s - T_{surr})L^3}{\nu\alpha}$$

$L$  = Characteristic length, m = surface area/perimeter.

$g$  = gravitational force, m/s<sup>2</sup>.

$\beta$  = Expansion coefficient, K<sup>-1</sup>.

$\nu$  = Kinematic viscosity of fluid, m<sup>2</sup>/s.

$\alpha$  = Thermal diffusivity of fluid, m<sup>2</sup>/s.

$k$  = Thermal conductivity of fluid, W/m K.

For the light-pipe which is in the shape of cylindrical rod and is oriented vertically, its geometry can be treated as a vertical plate. This can be true only if the cylinder diameter is larger than or equal to the boundary layer thickness [Incropera and Dewitt, 2002]. In our situation, it is always true. Therefore, the convective heat transfer coefficient can be obtained by using:

$$h_{ip} = \frac{k}{L} \left\{ 0.825 + \frac{0.387 Ra_L^{1/6}}{\left[ 1 + (0.492/Pr)^{9/16} \right]^{8/27}} \right\}^2 \quad (4.6)$$

where  $Pr$  is Prandtl number of fluid.

All thermophysical properties of the fluid were determined at the average temperature of the surface and surrounding temperatures.

In order to calculate the temperature distribution across the object's surface using equations 4.1 and 4.2, the finite difference method was applied. The finite difference method transforms the partial differential equation to an algebraic difference equation [Mill, 1999]. This approximate algebraic equation may be expressed in terms central-

difference, forward-difference, or backward-difference formulas depending on the nodal geometry [Incropera and Dewitt, 2002]. In numerical analysis, the light-pipe probe was divided into small elements having equal height of  $\Delta z$  while the object was meshed as small uniform rings having equal width of  $\Delta r$ .

Only a 25-grid element study was used in the simulation because of long computational time. However, the drop in temperature between 2-mm and 20.7-mm nearly converges to a constant value after using more than 10 elements as seen in Figure 4.22. Temperature drops of 0.52 °C and 0.67 °C were observed when using the grid study of 5 and 25, respectively. It also shows that the temperature of the object increases as the grid size decreases. But what we are concerned with in this simulation is the thermal depression in the center of the target instead of the real temperature across the target. Therefore, 25 elements are sufficient and used in all computer model cases.

Figure 4.23 shows the temperature distribution over the painted ceramic plate at different locations of sapphire light-pipe's tip separation when the center temperature of the object was near 475 °C. A temperature drop of 0.67 °C between 2-mm and 20.7-mm separation distances was found. But it is much smaller than what was found in the experimental study (thermal depression of 4.5 °C was measured). This is because the thermal conductivities of both target and light-pipe used in the computer simulation are at room temperature. At higher temperature, the ceramic and sapphire have lower thermal conductivities. Hence, the tip temperature of sapphire light-pipe must be higher than what was simulated but lower than the surrounding and target temperature. The thermal conductivity of ceramic at 1,000 °C is 5.85-6.69  $W/m \cdot K$  (<http://www.memsnet.org/material/aluminumoxideal/2o3bulk/>) and the thermal conductivity of sapphire at 900 °C is 7.54  $W/m \cdot K$  (<http://www.melleroptics.com/datasheets/sapphire-3.htm>). The

temperature non-uniformity across the ceramic caused by the separation distance effect should also be lower. This will increase the separation distance effect significantly.

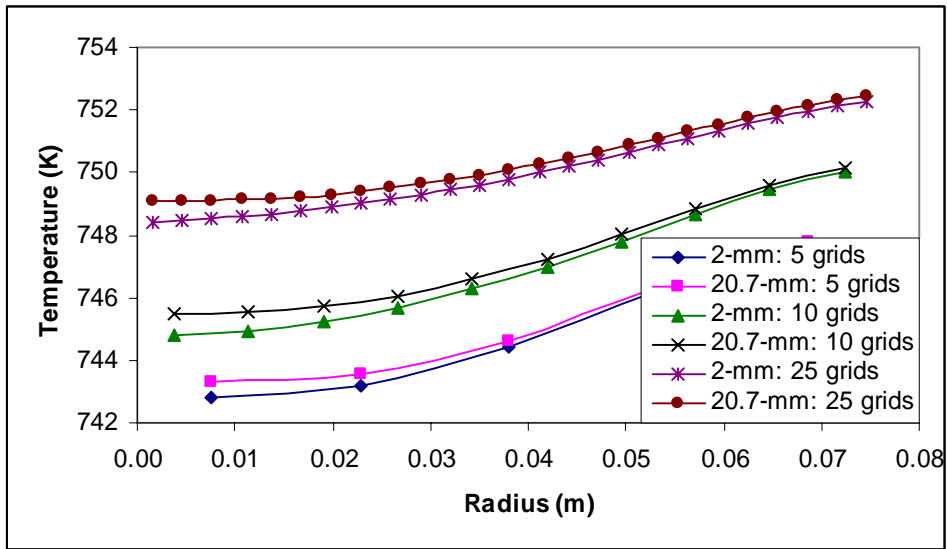


Figure 4.22: Grid study for object temperature.

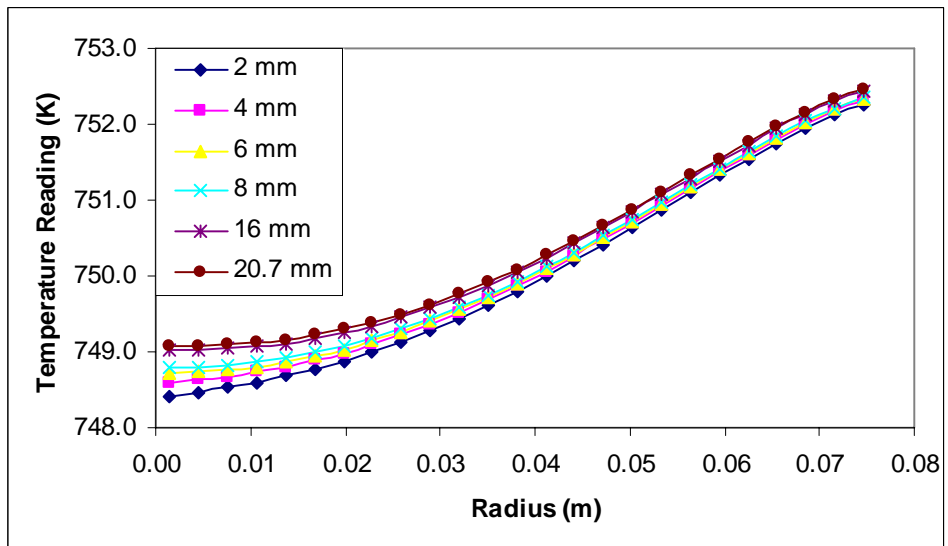


Figure 4.23: Temperature profile across the ceramic plate for different tip-to-target spacing of sapphire light-pipe.

Temperature differences at each separation distance and at 2-mm space were plotted in Figure 4.24. It shows that a depression of 1.99 °C occurred for the case of a molybdenum object and sapphire light-pipe. But this number is not consistent with the experimental results, where the ceramic-sapphire combination has a higher temperature drop than for molybdenum-sapphire. The reason is that both object's surfaces were painted by black paint. The ratio of thickness between the paint and the ceramic plate is small, but they are nearly equal for the paint and the molybdenum. Therefore, the thermal conductivity of painted molybdenum may be higher than we expect. The higher thermal conductivity will increase the temperature uniformity across the object's surface and will result in less thermal depression.

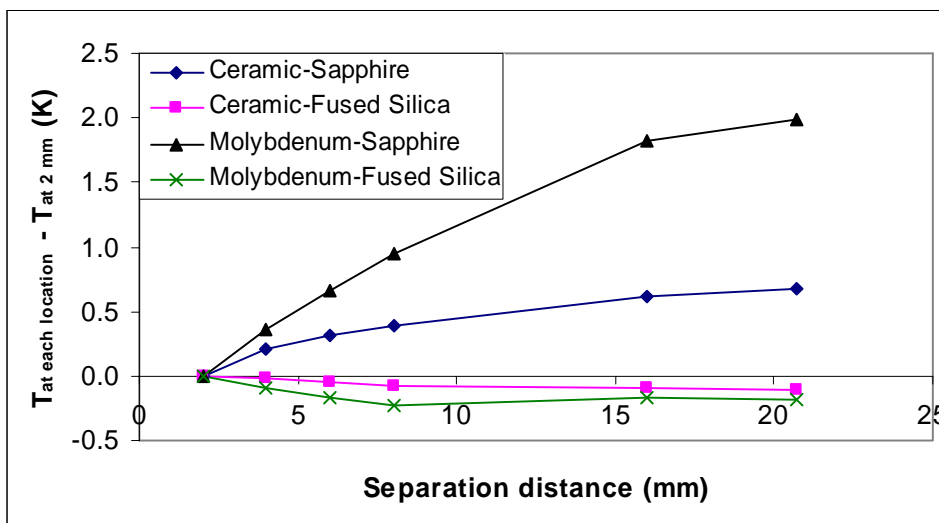


Figure 4.24: Comparison of the magnitude of the separation distance effect among different combination of object and light-pipe's materials.

Moreover, the simulation shows that the fused silica light-pipe did not cause any thermal depression on the target. On the other hand, the depression goes in the opposite way, although the variation with separation distance is small and may be within

measurement error. The lowest center temperature is not at 2-mm separation distance. Since the fused silica light-pipe has very low thermal conductivity as shown in Table 4.1, its tip temperature is much higher than for the sapphire light-pipe. Figure 4.25 illustrates the tip temperature of light-pipes for each case. The maximum tip temperature of fused silica light-pipe is almost the same as the surrounding temperature and is higher than the shield temperature. This is the reason why there is an increase in center temperature when the tip of fused silica light-pipe is closest to the measured object.

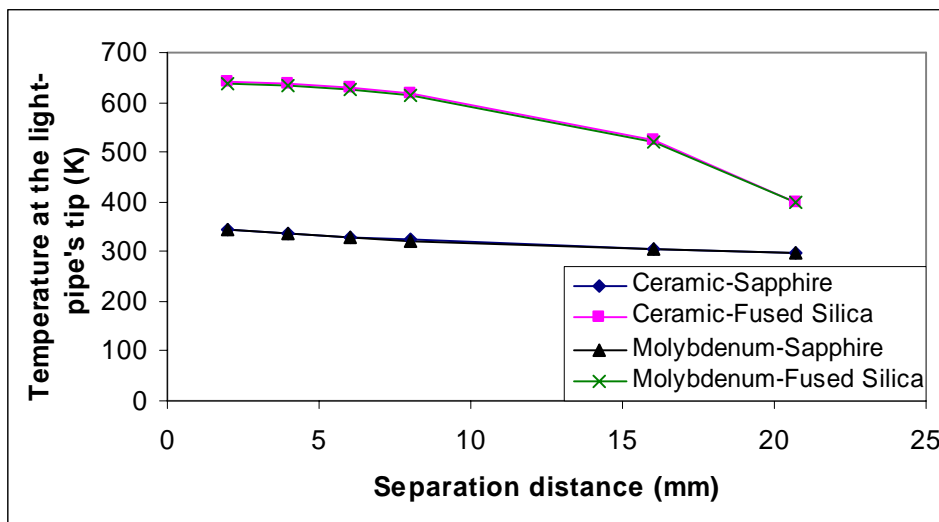


Figure 4.25: Tip temperature at each separation distance when using different kinds of objects and light-pipes.

#### 4.4 DETERMINATION OF ACCEPTANCE ANGLE OF LPRT SENSOR

To determine the acceptance angle, Snell's law defining the refraction of light crossing an interface between two media of differing indices of refraction shown in the following equation was used.

$$n_1 \sin \theta_1 = n_2 \sin \theta_2 \quad (4.7)$$

where  $\theta_1$  and  $\theta_2$  are the angle of incidence and the angle of refraction, respectively. The refractive index or index of refraction given the symbol  $n$  is the property of material showing that the phase velocity of electromagnetic radiation is slowed relative to its vacuum velocity, and is defined as a function of relative permittivity  $\epsilon_r$  and permeability  $\mu_r$  of material.

Based on the equation (4.7), the critical angle which is the minimum incidence angle creating total internal reflection instead of refraction can be calculated and given by

$$\theta_c = \arcsin\left(\frac{n_2}{n_1}\right) \quad (4.8)$$

When the light beam travels from a dense to a less dense medium ( $n_1 > n_2$ ) with a ray incident angle exceeding the critical angle, it will totally reflect off the interface (none can pass through). The incident angle on the tip that causes total internal reflection on the side of the light-pipe is called the acceptance angle.

Yan Qu (2006) created a computer simulation to evaluate the acceptance angle of a light-pipe and showed that its acceptance angle  $\chi^o$  is a function of incident plane distance  $r$  and refractive ratio  $n_{\text{vacuum}}/n_{LP}$  shown in equation (4.9). If the ratio of index of refraction  $n_{LP}/n_{\text{vacuum}}$  is greater than or equal to the square root of two, the acceptance angle will be  $90^\circ$  at all radii. Figure 4.26 illustrates Yan Qu's geometry relationship of incident angles.

$$\chi^o = \sin^{-1} \left( \frac{n_{LP}}{n_{\text{vacuum}}} \sin \left( \frac{\pi}{2} - \cos^{-1} \left( \frac{\cos \left( \sin^{-1} \left( \frac{n_{\text{vacuum}}}{n_{LP}} \right) \right)}{\cos \left( \sin^{-1} \left( \frac{r}{R} \right) \right)} \right) \right) \right) \quad (4.9)$$

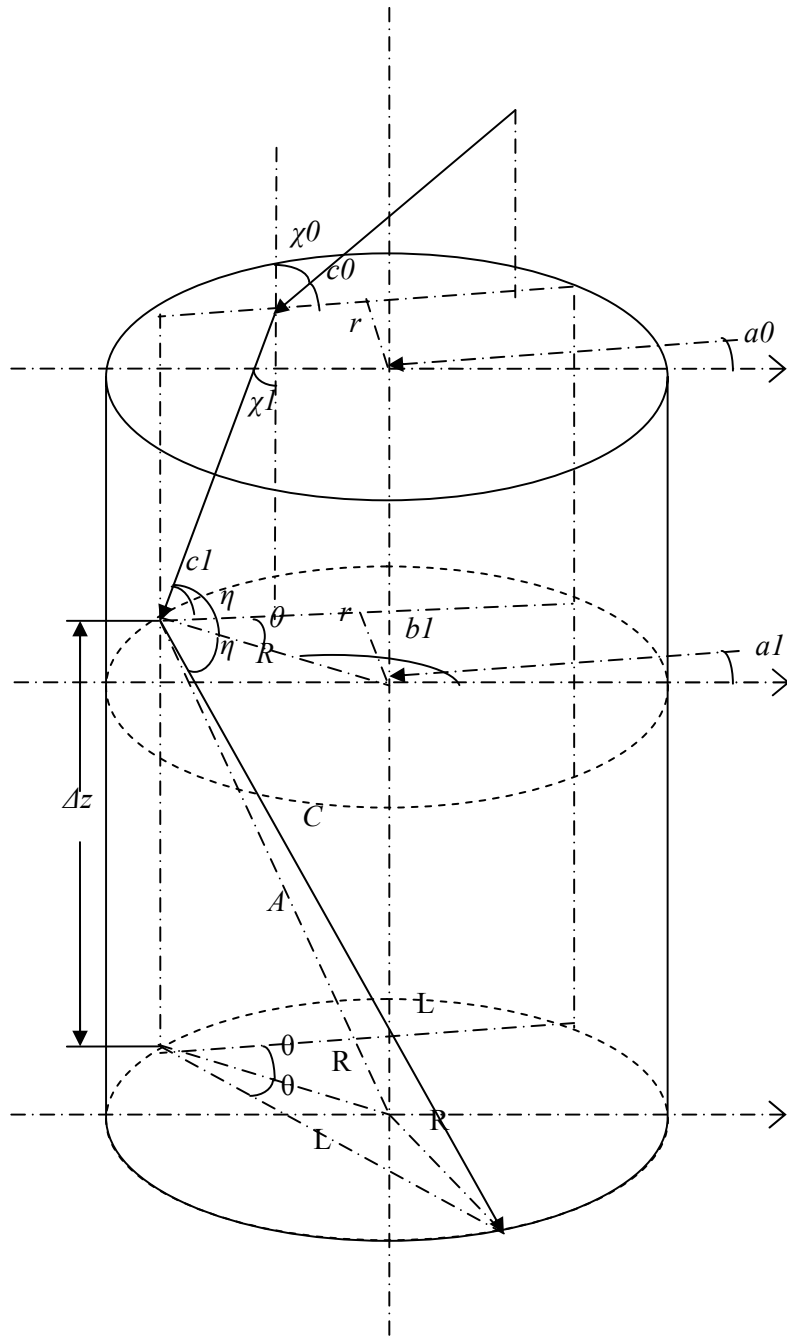


Figure 4.26: Schematic of light beam traveling inside the light-pipe probe relative to the incident angle [Qu, 2006].

At the effective wavelength of our photo detector which is 955.498 nm (from Section 3.2), the refractive indices of fused silica, fused quartz, and sapphire are higher than 1.414214. In this case, the acceptance angles of these light-pipe materials are  $90^\circ$ . To verify this assumption, an experiment to investigate the acceptance angle was conducted by using a laser pointer having the wavelength of 633.680 nm in order to generate the visible light beam. Figure 4.27 shows the experimental set-up.

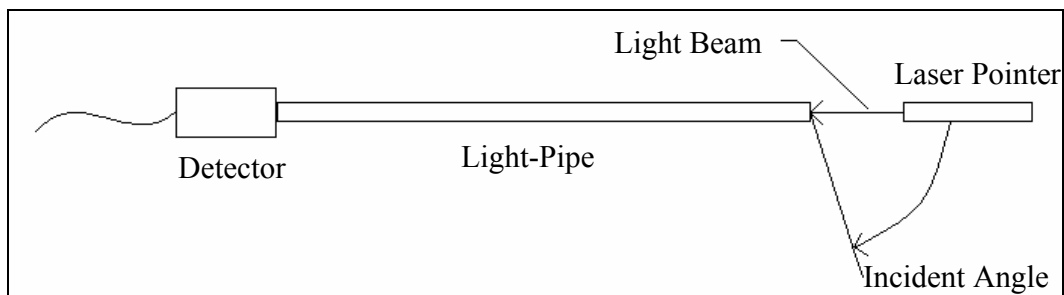


Figure 4.27: Schematic of experimental set-up for determining the acceptance angle.

With each type of light-pipe, the detector was set to calibration parameters of 400 °C before performing the experiment. The effective temperature measured at each incident angle was then assumed to be in proportion to the detector sensitivity at that angle. The light-pipe tip was oriented as close to the laser pointer as possible for each incident angle. This distance was varied depending on the angle; however, the maximum difference was within 25.4 mm. The experiment was started from 0 degrees, which is normal to the surface of light-pipe tip, to 85 degrees with increments of 5 degrees. The temperature readings were continuously recorded for a 30 second period at each increment. After completion of the ramp-up scan (0 to 85 degrees), the ramp-down scan from 85 to 0 degrees was conducted. The second, ramp-down, scan was an attempt to normalize any effect of the laser pointer intensity decaying with use. The corresponding

temperature data at each incident angle and each light-pipe material were averaged to yield a single effective temperature measurement and shown in Figure 4.28.

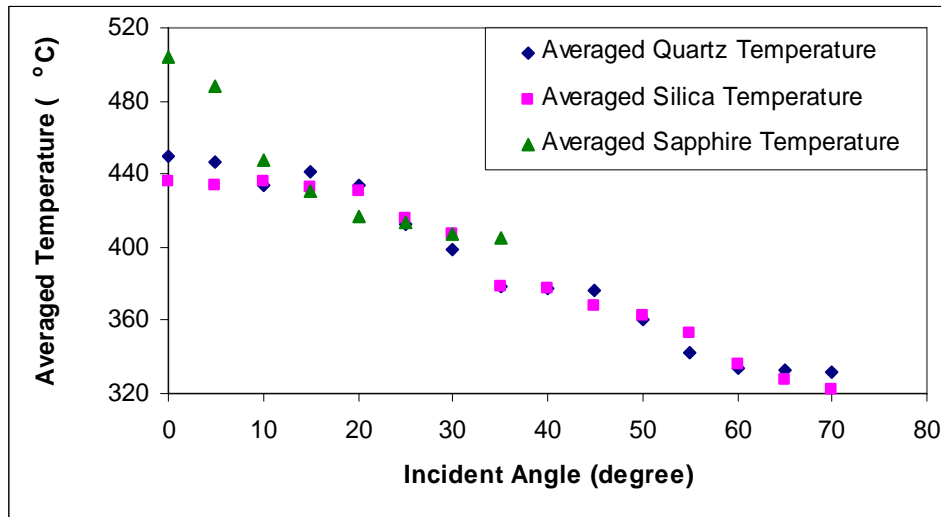


Figure 4.28: Illustration of averaged temperature readings obtained from different kinds of light-pipe versus the incident angle.

The results shown in Figure 4.28 indicated that the strongest signal was at the beginning of the ramp-up scan (0 degree) while the end of this scan (85 degree) gave the weakest. The uncertainty of the incident angle was calculated and equated to  $\pm 1.2$  degree. As mentioned earlier, the LPRT can detect an effective temperature above 300 °C for fused silica and fused quartz and above 400 °C for sapphire; therefore, the experiments for acceptance angles of fused silica and fused quartz were able to complete up to 70 degrees but only from 0 to 35 degrees was done for sapphire. Because of the inability to complete a full 90 degree scan, the MCM results for a fused silica light-pipe developed by Yan Qu was compared to the experimental results and shown in Figure 4.29 in order to predict whether the acceptance angle for all three light-pipe materials is 90 degree based on the theory.

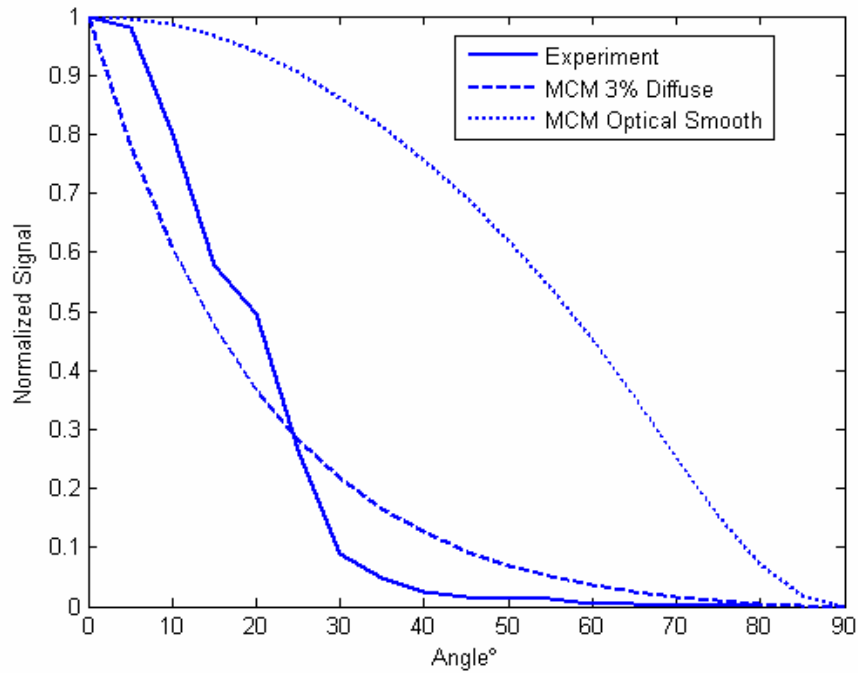


Figure 4.29: Comparison of the results obtained from the experiment and the MCM simulation for each incident angle.

The results for the signal received by the photo detector at each incident angle were normalized to the signal at the normal angle. It clearly shows that the acceptance angle is 90 degree and the diffuse component of reflectance plays an important role in allowing the radiation signal to travel through the light-pipe probe. Even for 3% diffusivity added into the MCM model, the normalized signal dropped dramatically. As it is known that our sapphire light-pipe has 100% non-specular reflectivity at the sensitive wavelength of the detector because of the roughness, only a small amount of radiation can pass through the probe. Thus, the signal at incident angles above 35 degrees was unable to be measured.

Figure 4.30 illustrates an example of the ring pattern of the light beam exiting from the light-pipe. It was caused by the photons from the edges around the diameter of

the light beam bouncing and exiting the light-pipe probe. This may be the reason why there is an error on the temperature indicated by an LPRT when the end of the light-pipe is disconnected from detector after being calibrated. A different location of light-pipe on the detector after reconnection may give a different temperature reading due to unsymmetrical properties inside the light-pipe material, or slight misalignment of the light-pipe and the detector surface.

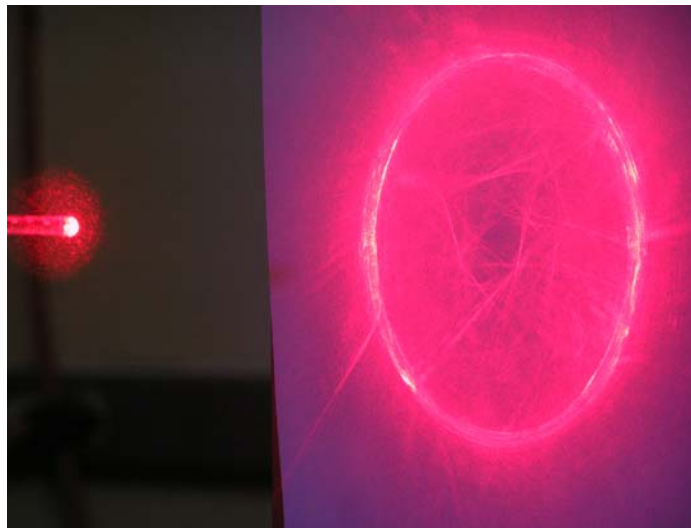


Figure 4.30: Illustration of the shape of light beam coming out from fused silica light-pipe when the distance between light-pipe tip and white paper is 168.3 mm and the incident angle is 10 degrees.

Knowing the distance between the centers of this ring shape and the light-pipe tip, the correlation between exit angle and incident angle was also determined. Within estimated uncertainty ranging from 0.3 to 2.3 degrees for fused silica and from 0.7 to 6.7 degrees for fused quartz, the exit angle correlates well to the incident angle. The estimation of these uncertainty values was based on the ability to discern the outer edge of the circle. As the incident angle increased, the circle got hazy and thick which resulted in an increased uncertainty. The uncertainty for fused quartz is greater than for fused

silica because the quartz is more diffuse and thus produces a less distinct exit circle than silica. Figure 4.31 shows the plot of exit angle versus incident angle results for fused silica and fused quartz light-pipes with an addition of the  $y = x$  line which is the expected result. As a result of surface scratches, there was too much attenuation to see a distinct shape from the exit photons from the sapphire light-pipe. However, there is no reason to believe that the exit angle would not be the same as the incident angle as well.

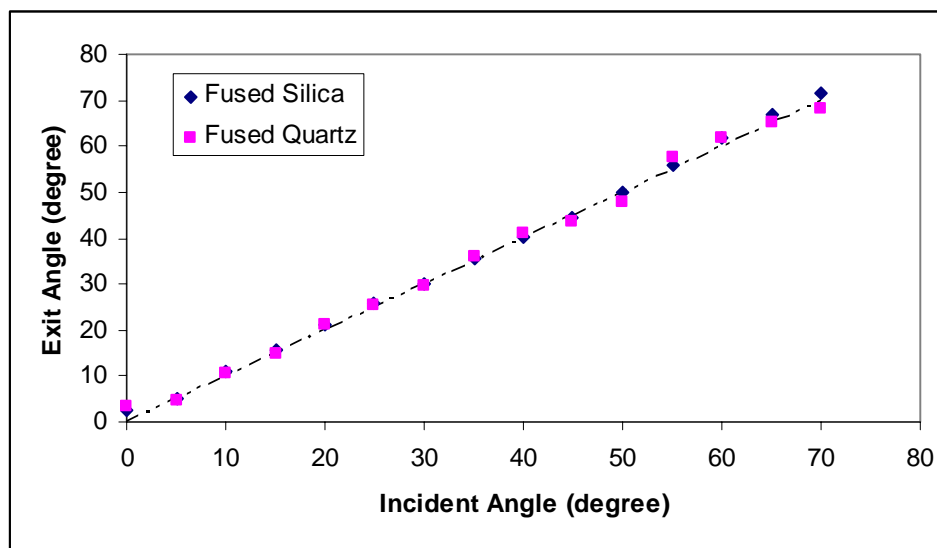
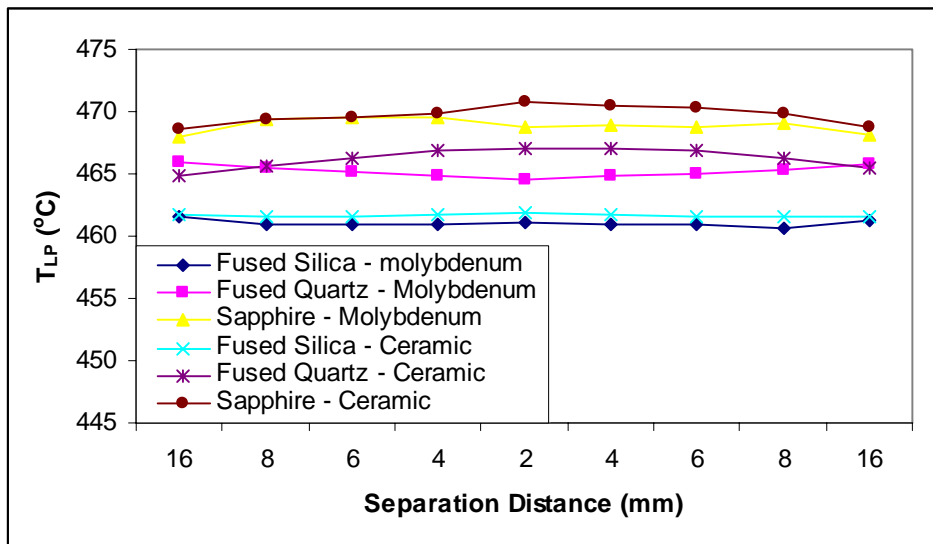


Figure 4.31: Exit angle versus incident angle (degrees) for fused silica and fused quartz light-pipes.

Since the acceptance angle of each type of light-pipe is  $90^\circ$ , the light-pipe tips can receive the radiation signal from all directions which means that the signal is not only from the target's surface but also from the surroundings. If the temperature of the surroundings is hotter than or close to that of the target, the light-pipe temperature reading will be increased due to increasing distance between the light-pipe tip and the target surface. However, this was not observed in this experiment as shown in Figure 4.32a because the surrounding temperature is colder than the object's surface as shown in

Table 4.3. The drop in temperature readings indicated by the LPRT between 2-mm and 16-mm separation distances was found instead.

a)



b)

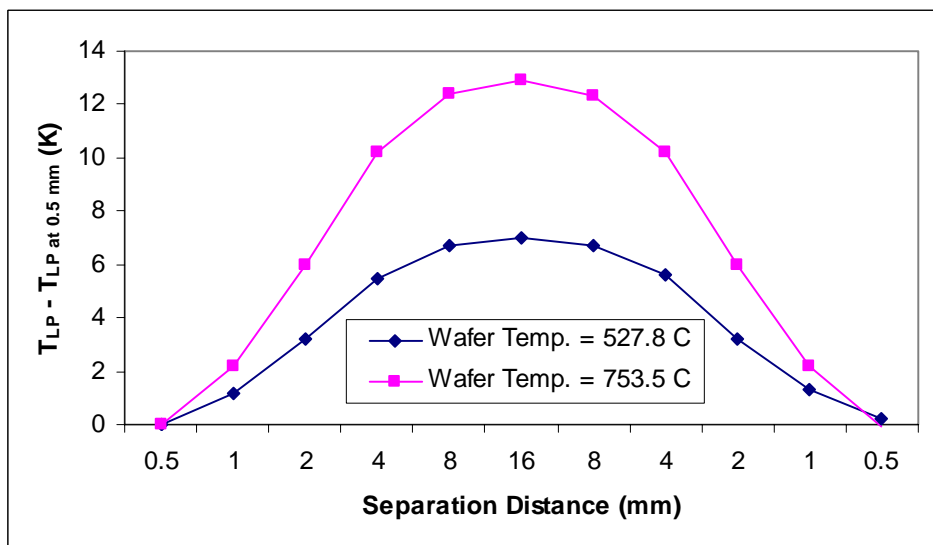


Figure 4.32: a) Light-pipe temperature readings at different LPRT's tip locations, and b) Light-pipe temperature differences at different separation distances and at 0.5 mm away from the surface of silicon wafer (in UT-Austin RTP test bed).

To investigate the effect of hot surrounding temperature due to the 90-degree acceptance angle, the fused silica light-pipe and an instrumented silicon wafer were inserted into the UT-Austin RTP test bed shown in Figure 4.2. The light-pipe was moved to different distances from a target surface by using a Z-stage Linear Displacement Mechanism (LDM). Before starting the investigation, the light-pipe was calibrated against a blackbody source and the temperature of radiation shield (top, bottom, and side) surrounding the silicon wafer was measured. Table 4.4 shows the shield temperatures along with the temperature of silicon wafer. As the tip-to-target surface distance was increased, the light-pipe readings changed approximately 6.9 °C and 13.0 °C when the wafer temperatures were approximately 527.8 °C and 753.5 °C, respectively.

Wafer Temp.	Top Shield Temp.	Bottom Shield Temp.	Side Shield Temp.
534.3	560.8	336.7	527.6
761.3	811.8	554.8	749.0

Table 4.4: Summary of shield temperature (°C) in UT-Austin RTP chamber.

Two major sources of these temperature differences caused by the location of the light-pipe were the radiation signals originating from the surroundings which: 1) goes directly into the light-pipe probe, and 2) reflects from the silicon wafer into the light-pipe probe. Yan Qu (2006) noted that this reflected radiation signal from a silicon wafer can be as large as 66.7% of the total error at a separation distance of 0.5 mm. If the object surface is absolutely black, no radiation signal from the surrounding could be reflected into the light-pipe.

## **Chapter 5: Conclusions and Recommendations**

Due to the requirement of accurate temperature measurement in Rapid Thermal Processing (RTP) with an uncertainty of  $\pm 1.5$  °C at 1,000 °C by the International Technology Roadmap for Semi-Conductor 2004 (ITRS-2004), the light-pipe radiation thermometer (LPRT) is becoming an important instrument. To understand the behavior of this type of sensor, to gain the fundamental knowledge required to improve its measurement accuracy, and to achieve the required measurement uncertainty, four important factors to characterize are the effective wavelength, the thermal environment effect, the separation distance effect, and the acceptance angle. These have been examined in this study with three different light-pipe materials: fused silica, fused quartz, and sapphire.

### **5.1. CONCLUSIONS**

#### **5.1.1 EFFECTIVE WAVELENGTH**

The characterization of the effective wavelength of the NTM 500-R LPRT system used in this study was done by using the infrared spectroradiometer. It is very important to know the operating wavelength in order to determine the real target temperature from the LPRT measured spectral radiance temperature when applying the temperature measurement equation (equation 1.4). The experiments for the detector with and without fused silica, fused quartz, and sapphire light-pipes were performed. Their results show that the effective wavelength range is between 954 nm and 957 nm with the expanded uncertainty ( $k = 2$ ) of  $\pm 1.3$  nm.

To be able to use the temperature measurement equation with this range, Dewitt and Nutter (1988) introduced the expression of the mean effective wavelength. Therefore, by replacing the upper and lower limits of sensitive wavelength range into this

expression, the operating effective wavelength was found and specified as  $955.5 \pm 0.0$  nm. However, the wavelength of 950.0 nm is used in CI-NTM 500 software instead for evaluating the true light-pipe temperature. This wavelength difference can cause an error which may exceed the accuracy of the detector itself depending on the effective spectral emissivity of the target's surface. Based on equation (1.4) with an assumed effective spectral emissivity of 0.1, the indicated temperature reading can be off by  $4.6 \pm 0.0$  °C if 950.0 nm is used. This means that specifying wrong effective wavelength is one of the contributors to the errors in LPRT temperature measurement.

### **5.1.2 THERMAL ENVIRONMENT EFFECT**

The experiments reveal that the thermal environment can greatly affect the quality of an LPRT measurement. The errors in the indicated temperature increase to unacceptable levels when the surrounding temperature is higher than the target temperature. Based on the radiation properties of light-pipe materials in the range of the effective wavelength of our detector, which is 954 - 957 nm, sapphire should experience the least effect of the thermal environment while fused quartz should have the most. However, the external radiation can cause an extreme error on LPRT readings if the side of the light-pipe has surface imperfections. The error can be as high as  $1,692.2 \pm 23.1$  °C for the fused silica light-pipe having a surface roughness of 0.77 microns and in surrounding of temperature 1,100 °C. Therefore, this effect is unavoidable when using the LPRT in the RTP chamber having hot walls with resistively heated silicon carbide heating elements as mentioned in Chapter 1, or in batch processing furnaces.

The MCM computer simulation indicates that the non-specular component of reflectivity plays the important role in this measurement error. For a highly polished light-pipe with little diffuse component of reflectivity, no thermal environment effect exists. If the length of the light-pipe is rubbed by sandpaper which creates a higher value

of surface roughness, the specular reflectivity component will be replaced by an equivalent diffuse reflectivity component. Even for a relatively smooth light-pipe probe which has a diffuse reflectivity of 0.002%, a significant error in temperature readings indicated by LPRT can be observed. Furthermore, the results from both experiment and computer analysis demonstrate that the error will start to appear when the environment temperature approaches the blackbody temperature by less than 160 °C.

In order to minimize the error due to the thermal environment effect, the LPRT should be calibrated in an environment similar to that of its intended use, be used in a cold surrounding environment (more than 160 °C below the target temperature), or expose the minimum LPRT length to a hot surrounding temperature in order to decrease the amount of radiation signal getting into the light-pipe's sidewall. The experimental results show that this error can be less than  $\pm 0.3$  °C and  $\pm 2.9$  °C when using the LPRT at the same surrounding temperature as for the calibration and in a colder environment than the blackbody, respectively.

### **5.1.3 SEPARATION DISTANCE EFFECT**

The separation distance effect is the thermal depression occurring on the object's surface. It is caused by the physical mass and configuration of the light-pipe probe. Since most of its surface area is surrounded by room temperature, the temperature at the tip of the light-pipe will be colder than at the target. Therefore, it acts as a radiation heat sink for the measured object. A temperature drop of 25 °C was measured by NIST researchers when the sapphire light-pipe was 2-mm from the silicon wafer. This study was conducted inside the NIST RTP test bed. These researchers also concluded that the magnitude of the temperature depression was a function of the distance between the light-pipe tip and the target and between the reflection shield and the target. However, a similar experiment using a fused silica light-pipe and the UT-Austin RTP test bed was conducted by Yan Qu.

He found no evidence of the separation distance effect even though the light-pipe tip was located as close as 0.5 mm from the silicon wafer.

I performed another similar experiment by using a new chamber. Two types of measured object; molybdenum and ceramic, painted with flat black ultra-high-temperature paint and three different light-pipe materials; fused silica, fused quartz, and sapphire, were used to investigate the separation distance effect. A 4.5 °C depression was observed with the combination of a sapphire light-pipe and ceramic plate when the distance between the sapphire light-pipe tip and the ceramic's surface was varied from 2 mm to 32 mm. No temperature drop occurred when fused silica and fused quartz light-pipes were used to measure the temperature of molybdenum sheet. This is because sapphire has higher thermal conductivity than fused silica and fused quartz while molybdenum has higher thermal conductivity than ceramic. The higher the thermal conductivity of the light-pipe, the larger heat loss can be extracted. Large thermal conductivity on target localizes and magnifies the temperature depression.

The computer model using the finite-difference method was developed to predict the temperature depression as a function of object-light-pipe separation distance. The simulated data were consistent with the experimental data showing that only a sapphire light-pipe can cause this effect. The magnitude of the effect also depends on the thermal conductivity and the thickness of the target. All thermal conductivities used in the simulation are at room temperature, the thermal depression found in my computer model was lower than in the experiment. At higher temperature, ceramic, molybdenum, and sapphire have lower thermal conductivity values than at lower temperature while fused silica and fused quartz have higher.

Another interesting discovery in the investigation of the separation distance effect is that the center temperature of the measured object increases slightly when the fused

silica light-pipe was moved close to the target. This is because the light-pipe is heated by both environment and target and the thermal conductivity of fused silica is extremely low leading to less heat transfer along the fused silica light-pipe probe. Thus, its tip temperature is almost the same as the surrounding temperature and is higher than the shield temperature as compared to the sapphire light-pipe. The higher the light-pipe tip temperature, the less is the drop in center temperature of the target.

#### **5.1.4 EFFECT OF ACCEPTANCE ANGLE**

In order to understand how much the radiation signal can be collected by the LPRT when it moves to different locations, we must know the acceptance angle of the light-pipe probe. Snell's law shows that total internal reflection can occur only if the light beam travels from a medium with larger refractive index to another medium having smaller index of refraction. Furthermore, if the refractive index ratio is greater than or equal to the square root of two, the LPRT acceptance angle will be  $90^\circ$ . For all three light-pipe materials used in this research, their refractive indices at the detector's effective wavelength are higher than 1.414214. So, they must have the acceptance angles of  $90^\circ$ .

The assumption was confirmed by both experiment and computer simulation. Using a 633.68-nm laser pointer, the results show that the light beam is transmitted through the fused silica and fused quartz light-pipes until the incident angle exceeded 70 degrees. For a sapphire light-pipe, the signal was only transmitted up to 35 degrees. It is noted that the refractive index is a function of wavelength. The higher the wavelength, the lower the refractive index is. So, at 633.68 nm, these light-pipes should have  $90^\circ$  acceptance angles. There are three reasons why they were not  $90^\circ$ . First, it is impossible in practice to shoot the laser pointer parallel to the plane of the light-pipe's tip. Second, our LPRT system can detect the target's temperature higher than  $300^\circ\text{C}$  for fused silica

and fused quartz light-pipes and 400 °C for sapphire light-pipe. As the incident angle increases, the amount of radiation signal received by the detector keeps decreasing until the detectivity threshold is reached. Last, the surfaces of light-pipe sidewalls are not smooth causing a higher diffuse component of reflectivity. This diffuse reflectivity plays an important role in the transmission of the signal. The higher the surface roughness compared to the effective wavelength of the detector, the less signal can pass through the light-pipe, again reducing the signal to below the level of detectivity.

However, the MCM computer simulation developed by Yan Qu gives a consistent result with the experimental result for the incident angle from 0 to 70 degrees when applying 3% of diffuse reflectivity to the light-pipe surface. It also predicts that the radiation energy can be collected by the detector even though the incident angle equates to 90°. Since the acceptance angles are 90 degrees for all three light-pipe materials, they will receive the signal from all directions no matter how close the light-pipe tip is to the object's surface. If the surrounding temperature is hot and the object has low emissivity, the temperature indicated by LPRT will increase when the tip-to-target surface distance is increased as shown in the experimental results.

Finally, based on the results of this work, the errors inherent in LPRT measurements of object temperature can be minimized by: taking care to minimize scratches or imperfections in the LPRT surface; reducing the length of the LPRT that is exposed to high-temperature surroundings; minimizing the LPRT-object separation distance; assuring that the effective wavelength used in software conversion of LPRT signal to temperature readout is appropriate; choosing a light-pipe material that has low thermal conductivity; and if possible, calibrating the LPRT in situ.

## 5.2 RECOMMENDATIONS

Based on the experimental study of the thermal environment effect, only three surface roughness of fused silica light-pipe were completed and one of them has nearly the same value as the operating effective wavelength of our detector. In order to evaluate the effect of this roughness on the indicated temperature of LPRT, more experiments with lower averaged surface roughness than the value of sensitive wavelength and with different types of light-pipes must be performed. This might allow for better comparison of the rough-surface LPRT with its operating effective wavelength. Highly accurate temperature sensors such as resistance thermometers should also be used to monitor the furnace temperature distribution. Furthermore, because the LPRT may be used during the rapid thermal chemical vapor decomposition (RTCVD) as mentioned in Chapter 1, another experiment on determining the effect of chemical used in this processing that can deposit impurities on the rough-surface light-pipe should be taken into consideration.

In the MCM modeling for determining the effect of thermal environment with different surface roughness developed by Yan Qu (2006), he assumed the light-pipe to have a smooth surface and varied the value of diffuse reflectivity to match the simulation results to the experimental results. To obtain more accurate model, more information of the surface roughness such as shape, height, and space between each peak needs to be considered to achieve a better understanding of how these factors can affect to the light-pipe measurement. Non-uniform temperature distributions inside the tube furnace must also be taken into account.

For the separation distance effect, all experiments should be repeated in UT-Austin RTP chamber because of good uniform temperature distribution. An instrumented silicon wafer must also be used as an object. In the computer modeling work, future work should include more sophisticated physics than I have specified. The details of the

specular and diffuse components of reflectivity of the radiation shield must be considered. Non-uniform surroundings and the shield temperature distribution must also be taken into account. Instead of assuming the diffuse-gray surfaces and using the finite difference method to calculate the temperature distribution across the object's surface, a Monte Carlo Method (MCM) which accounts for a complete set of radiation properties of the chamber must be used to model the signal transfer process inside the chamber. The thermal environment effect must be taken into account in this computer study model.

Due to the 90-degree acceptance angle of light-pipes, the temperature indicated by the LPRT can be affected by the radiation signal surrounding the light-pipe tip. The variation on the temperature readings as the tip-to-target surface distance changes caused by the hot surrounding temperature must be determined by both experiment and computer model. In the experimental study of this effect, it can be done by both using a material having high emissivity as an object in order to eliminate the shadow effect introduced by Yan Qu (2006) and minimizing the length of light-pipe that exposed to hot surrounding temperature in order to reduce the effect of thermal environment. The computer simulation study can be conducted by using the MCM to quantify the radiation energy generated from the surrounding environment that can reach the photo-detector.

## References

- 2005, *Advantages and Challenges Associated with the Introduction of 450mm Wafers*, URL: <http://www.itrs.net>.
- Abernethy, R. B., Benedict, R. P., and Dowdell, R. B., 1985, *ASME Measurement Uncertainty*, Journal of Fluids Engineering, Volume 107, p161.
- Arunkumar, M., 2003, *Effect of Distance on Light Pipe Radiation Thermometer Measurements in an RTP Thermometry Test Bed*, Thesis, Mechanical Engineering Department, the University of Texas at Austin, Austin, TX.
- Ball, K. S., and Howell J. R., 2004, *Modeling and Experimental results for an RTP Light-Pipe Radiation Thermometer Calibration Testbed*, 12<sup>th</sup> IEEE International Conference on Advanced Thermal Processing of Semiconductors – RTP2004, Portland, OR, pp.175-180.
- Ball, K. S., Huston, K. S., Noska, B. L., Simonich, M. A., Geyling, F.T., Sing, D., Tichy, R.S., and Baharav, Y., 2001, *The UT/NIST/SA/ISMT Thermometry Test Bed – 2001*, Proceedings of 9<sup>th</sup> International Conference on Advanced Thermal Processing of Semiconductors.
- Bentley, R. E., 1998, *Theory and Practice of Thermoelectric Thermometry*, Handbook of Temperature Measurement Volume 3, Springer-Verlag, Singapore.
- Blakeney, J. K., 2000, *Wafer Temperature Measurements in a Thermometry Test Bed*, Thesis, Mechanical Engineering Department, the University of Texas at Austin, Austin, TX.
- Born, M., and Wolf, E., 1993, *Principles of Optics*, 6<sup>th</sup> edition, Pergamon Press, New York.
- Cengel, Y. A., 1998, *Heat Transfer: A Practical Approach*, McGraw-Hill, New Jersey.
- Chen, D. H., DeWitt, D. P., Tsai, B. K., Kreider, K. G., and Kimes, W.A., 2002, *Effects of Wafer Emissivity on Rapid Thermal Processing Temperature Measurement*, 10<sup>th</sup> IEEE International Conference on Advanced Thermal Processing of Semiconductors- RTP 2002.
- Coleman, H. W., and Steele, W. G., JR., 1989, *Experimentation and Uncertainty Analysis for Engineers*, John Wiley & Sons, Canada.
- DeWitt, D. P., and Nutter, G. D., 1988, *Theory and Practice of Radiation Thermometry*, John Wiley and Sons, New York.

- Eckert, Ernst R. G., and Goldstein, R. J., 1976, *Measurements in Heat Transfer*, 2<sup>nd</sup> edition, Hemisphere Publishing, Washington, DC.
- Figliola, R. S., and Beasley, D. E., 2006, *Theory and Design for Mechanical Measurements*, 4<sup>th</sup> edition, John Wiley & Sons, New Jersey.
- Frankman, D. J., Webb, B. W., and Jones, M. R., 2006, *Investigation of Lightpipe Volumetric Radiation Effects in RTP Thermometry*, Journal of Heat Transfer, Volume 128, Issue 2, p132.
- Fukuda, H., 2003, *Rapid Thermal Processing for Future Semiconductor Devices*, Elsevier Science, Netherlands.
- Gertsbakh, I., 2003, *Measurement Theory for Engineers*, Springer-Verlag Berlin Heidelberg, Germany.
- Geyling, F., Van Eck, B., Ball, K., Powers, B., and Blakeney, J., 2000, *The UT/NIST/SA/ISMT Thermometry Test Bed*, 8<sup>th</sup> IEEE International Conference on Advanced Thermal Processing of Semiconductors-RTP 2000.
- Hart, M. J., and Evans, A. G. R., 1988, *Rapid Thermal Processing in Semiconductor Technology*, Semiconductor Science and Technology, Volume 3, Issue 5, p421.
- Husain, R., and An-Nahdi K. A. 2000, *Uncertainty Calculations in a Measurement Standards Laboratory*, Proceedings of the National Science Council, Republic of China, Part A: Physical Science and Engineering, Volume 24, Issue 3, p210.
- Huston, K. S., 2002, *Temperature Measurement Issues in an RTP Thermometry Test Bed*, Thesis, Mechanical Engineering Department, the University of Texas at Austin, Austin, TX.
- Incropera, F. P., and DeWitt, D. P., 2002, *Fundamentals of Heat and Mass Transfer*, 5<sup>th</sup> edition, John Wiley and Sons, New York.
- Incropera, F. P., and DeWitt, D. P., 2002, *Fundamentals of Heat and Mass Transfer*, 5<sup>th</sup> edition, John Wiley and Sons, New York.
- Kline, S. J., 1985, *The Purposes of Uncertainty Analysis*, Journal of Fluids Engineering, Volume 107, p153.
- Kline, S. J., and McClintock, F. A., 1953, *Describing Uncertainties in Single-Sample Experiments*, Journal of Fluids Engineering, Volume 75, p3.
- Kreider, K. G., Chen, D. H., DeWitt, D. P., Kimes, W. A., and Tsai, B. K. 2003, *Light Pipe Proximity Effects on Si Wafer Temperature in Rapid Thermal Processing*

- Tools*, Proceedings of the 11th IEEE International Conference on Advanced Thermal Processing of Semiconductors – RTP 2003, pp. 125 – 129.
- Kreider, K. G., Kimes, W. A., Meyer, C. W., Ripple, D. C., Tsai, B. K., Chen, D. C., and Dewitt, D. P., 2003, *Calibration of Radiation Thermometers in Rapid Thermal Processing Tools Using Si Wafers with Thin-film Thermocouples*, in *Temperature: Its Measurement and Control in Science and Industry*, Volume 7, AIP Conference Proceedings, Melville, New York.
- Kreyszig, E., 1999, *Advanced Engineering Mathematics*, 8<sup>th</sup> edition, John Wiley & Sons, Singapore.
- Lira, I., 2002, *Evaluating the Measurement Uncertainty*, Institute of Physics Publishing, London, England.
- Malitson, I. H., 1965, *Interspecimen Comparison of the Refractive Index of Fused Silica*, *Journal of the Optical Society of America*, Volume 55, Issue 10, p1205.
- Mathews, J. H., 1992, *Numerical Methods for Mathematics, Science, and Engineering*, 2<sup>nd</sup> edition, Prentice-Hall, New Jersey.
- Maxwell, J. D., 2005, *Full Field Temperature Measurement of Silicon Wafers During Rapid Thermal Processing*, Thesis, Mechanical Engineering Department, the University of Texas at Austin, Austin, TX.
- McGee, T. D., *Principles and Methods of Temperature Measurement*, John Wiley & Sons, Canada.
- Meyer, C. W., DeWitt, D. P., Kreider, K. G., Lovas, F. J., and Tsai, B. K., 2001, *ITS-90 Calibration of Radiation Thermometers for RTP Using Wire/Thin-film Thermocouples on a Wafer*, AIP Conference Proceedings 2001, Volume 550, Issue 1, p254.
- Meyer, C. W., June, 2001, *Effects of Extraneous Radiation on the Performance of Lightpipe Radiation Thermometers*, TEMPMEKO, 8th International Symposium on Temperature and Thermal Measurement in Industry and Science.
- Michalski, L., Eckersdorf, K., and McGhee, J., 1991, *Temperature Measurement*, John Wiley & Sons, England.
- Mills, A. F., 1999, *Heat Transfer*, 2<sup>nd</sup> edition, Prentice-Hall, New Jersey.
- Modest, M. F., 2003, *Radiative Heat Transfer*, 2<sup>nd</sup> edition, Academic Press, California.
- Nicholas, J. V., and White, D. R., 1994, *Traceable Temperatures*, John Wiley & Sons, England.

- Perkins, R. H., Riley, T. J., and Gyurcsik, R. S., 1995, *Thermal Uniformity and Stress Minimization During Rapid Thermal Processes*, IEEE Transactions on Semiconductor Manufacturing, Volume 8, Issue 3, p272.
- Puttitwong, E., Qu, Y., Howell, J. R., and Ezekoye, O.A., 2006, *Effects of Thermal Environment and Surface Roughness on LPRTs in Surface Temperature Measurement*, 9th AIAA/ASME Joint Thermophysics and Heat Transfer Conference.
- Qu, Y., 2003, *Emissivity Issues in Silicon Wafer Surface Temperature Measurement in RTP System*, Thesis, Mechanical Engineering Department, the University of Texas at Austin, Austin, TX.
- Qu, Y., 2006, *Silicon Wafer Surface Temperature Measurement using Light-pipe Radiation Thermometers in Rapid Thermal Processing*, Dissertation, Mechanical Engineering Department, the University of Texas at Austin, Austin, TX.
- Qu, Y., Puttitwong, E., Howell, J. R., and Ezekoye, O. A., 2006, *Shadow-Effect of Light-pipes in Silicon Wafer Surface Temperature Measurements*, 9th AIAA/ASME Joint Thermophysics and Heat Transfer Conference.
- Qu, Y., Puttitwong, E., Howell, J. R., Ezekoye, O. A., and Ball, K. S., 2005, *Drawdown-Effect of Lightpipes in Silicon Wafer Surface Temperature Measurements*, ASME Heat Transfer Conference.
- Quinn, T. J., 1990, *Temperature*, 2<sup>nd</sup> edition, Academic Press, San Diego, California.
- Ranish, J. M., 2003, *Design of Halogen Lamps for Rapid Thermal Processing*, 11<sup>th</sup> IEEE International Conference on Advanced Thermal Processing of Semiconductors-RTP 2003.
- Sato, K., 1967, *Spectral Emissivity of Silicon*, Japanese Journal of Applied Physics Volume 6, pp. 339-347.
- Schneider, W. E., 1985, *Automated Spectroradiometrics Systems: Components and Applications*, Technical Publishing, a Division of Dun-Donnelley Publishing Corp.
- Schooley, J. F., 1986, *Thermometry*, CRC Press, Florida.
- Siegel, R., and Howell, J. R., 2002, *Thermal Radiation Heat Transfer*, 4<sup>th</sup> edition, Taylor and Francis, New York.
- Simonich, M. A., 2001, *Silicon Wafer Temperature Measurements and Uncertainty Analysis in a RTP Thermometry Test Bed*, Thesis, Mechanical Engineering Department, the University of Texas at Austin, Austin, TX.

- Singh, R., Fakhruddin, M., and Poole, K. F., 2003, *The Impact of Single-Wafer Processing on Semiconductor Manufacturing*, IEEE Transactions on Semiconductor Manufacturing, Volume 16, Issue 2, p96.
- Smith, T. F. and Hering; R. G., August 5-8 1973, *Comparison of the Beckman Model with Bidirectional Reflectance Measurements*, ASME-AIChE, Heat Transfer Conference, Atlanta, GA.
- Tan, G. Y., 2002, *Light Pipe Radiation Thermometry in an RTP Thermometry Test Bed*, Thesis, Mechanical Engineering Department, the University of Texas at Austin, Austin, TX.
- Taylor, B. N., and Kuyatt, C. E., 2001, *Guidelines for Evaluating and Expressing the Uncertainty of NIST Measurement Results*, URL: <http://www.physics.nist.gov/Pubs/guidelines/appb/htm>.
- Timans, P. J., 1998, *Rapid Thermal Processing technology for the 21<sup>st</sup> Century*, Materials Science in Semiconductor Processing, Volume 1, Issue 3-4, p169.
- Tsai, B. K., 2003, *Traceable Temperature Calibrations of Radiation Thermometers for Rapid Thermal Processing*, 11<sup>th</sup> IEEE International Conference on Advanced Thermal Processing of Semiconductors-RTP 2003.
- Tsai, B. K., and DeWitt, D. P., 2003, *Characterization and Calibration of Lightpipe Radiation Thermometers for Use in Rapid Thermal Processing*, AIP Conference Proceedings, Volume 684 Issue 1, p441.
- Tsai, B. K., DeWitt, D. P., Lovas, F. J., Kreider, K. G., Meyer, C. W., and Allen, D. W., 1999, *Chamber Radiation Effects on Calibration of Radiation Thermometers with a Thin-film Thermocouple Test Wafer*, TEMPMEKO International Symposium on Temperature and Thermal Measurements in Industry and Science.
- Yan, J., 1999, *A New Approach to Measure the Temperature in Rapid Thermal Processing (RTP)*, Dissertation, Mechanical Engineering Department, the University of Texas at Austin, Austin, TX.
- Yoo, W. S., Yamazaki, T., and Enjoji, K., 2000, *Thermal Processing in a Single Wafer Rapid Thermal Furnace*, Solid State Technology, Volume 43, Issue 7, p223.

## **Vita**

Ekachai Puttitwong was born in Bangkok, Thailand on August 23, 1973, the son of Suthep Puttitwong and Pimpa Puttitwong. After Mr. Puttitwong completed his high school at Lasalle Bangna College, Bangkok, Thailand, he received the degree of Bachelor of Engineering in Mechanical Engineering from Chiang Mai University, Chiang Mai, Thailand in May, 1995. Upon his graduation, he had worked as an engineer in the Technical Information department of the Toyota Motor Thailand Co., Ltd., Samutprakarn, Thailand for 13 months. He received his Master of Science in Mechanical Engineering from Ohio University, Athens, Ohio in June, 1999. In his last year at the Graduate School of Ohio University, he was sent to work as a part-time engineer in the Technical department at the Stirling Technology, Inc., Athens, Ohio. During the following years, he was employed as a metrologist in the Thermometry department at the National Institute of Metrology Thailand, Pathumthani, Thailand. In the spring of 2003, he began to pursue a doctoral degree in Mechanical Engineering at the University of Texas at Austin.

Permanent address: 1347 Moo 4 Theparak Road,  
Meuang, Samutprakarn,  
Thailand 10270

This dissertation was typed by the author.